https://doi.org/10.15388/vu.thesis.245
https://orcid.org/0000-0002-9223-9363

VILNIUS UNIVERSITY
CENTER FOR PHYSICAL SCIENCES AND TECHNOLOGY

Karolis
MADEIKIS

Investigation of the ultrafast fiber and hybrid laser systems and their nonlinear wavelength conversion methods in the infrared spectral region

DOCTORAL DISSERTATION

Natural sciences,
Physics (N 002)

VILNIUS 2021

This dissertation was written between 2016 and 2020 at the Department of Laser Technologies of the Center for Physical Sciences and Technology. The research was performed at the company Ekspla and the Science and Technology Park. The research was supported by the Research Council of Lithuania.

Academic supervisor:
Dr. Andrejus Michailovas (Center for Physical Sciences and Technology, Natural Sciences, Physics, N 002).

Dissertation Defence Panel:
Chairman – Prof. Habil. Dr. Vidmantas Gulbinas (Center for Physical Sciences and Technology, Natural Sciences, Physics, N 002).
Members:
Prof. Dr. Virginijus Barzda (Toronto University, Natural Sciences, Physics, N 002).
Dr. Mindaugas Gedvilas (Center for Physical Sciences and Technology, Technological Sciences, Materials Engineering, T 008).
Dr. Rimantas Grigonis (Vilnius University, Natural Sciences, Physics, N 002).
Assoc. Prof. Dr. Vytautas Jukna (Vilnius University, Natural Sciences, Physics, N 002).

The dissertation shall be defended at a public meeting of the Dissertation Defence Panel at 16:00 on 16th November 2021 in the hall of FTMC Institute of Physics.
Address: Savanoriu Ave. 231, LT-02300 Vilnius, Lithuania
Tel. +370 5 264 8884; e-mail: office@ftmc.lt

The text of this dissertation can be accessed at the libraries of the Center for Physical Sciences and Technology and Vilnius University, as well as on the website of Vilnius University:
www.vu.lt/lt/naujienos/ivykiu-kalendorius

https://doi.org/10.15388/vu.thesis.245
https://orcid.org/0000-0002-9223-9363

VILNIAUS UNIVERSITETAS
FIZINIŲ IR TECHNOLOGIJOS MOKSLŲ CENTRAS

Karolis
MADEIKIS

Ultrasparčių skaidulinių ir hibridinių lazerinių sistemų bei jų bangos ilgio netiesinio keitimo infraraudonajame spektriniame diapazone metodų tyrimai

DAKTARO DISERTACIJA

Gamtos mokslai,
Fizika (N 002)

VILNIUS 2021

Disertacija rengta 2016–2020 metais valstybinio mokslinių tyrimų instituto Fizinių ir technologijos mokslų centro Lazerinių technologijų skyriuje. Tyrimai buvo atlikti įmonės Ekspla ir Technologijų parko laboratorijose. Mokslinius tyrimus rėmė Lietuvos mokslo taryba.

Mokslinis vadovas:
Dr. Andrejus Michailovas (Fizinių ir technologijos mokslų centras, gamtos mokslai, fizika – N 002).

Gynimo taryba:
Pirmininkas – Prof. habil. dr. Vidmantas Gulbinas (Fizinių ir technologijos mokslų centras, gamtos mokslai, fizika, N 002).
Nariai:
Prof. dr. Virginijus Barzda (Toronto universitetas, gamtos mokslai, fizika, N 002).
Dr. Mindaugas Gedvilas (Fizinių ir technologijos mokslų centras, technologijos mokslai, medžiagų inžinerija, T 008).
Dr. Rimantas Grigonis (Vilniaus universitetas, gamtos mokslai, fizika, N 002).
Doc. dr. Vytautas Jukna (Vilniaus universitetas, gamtos mokslai, fizika, N 002).

Disertacija ginama viešame Gynimo tarybos posėdyje 2021 m. lapkričio mėn. 16 d. 16:00 val. FTMC Fizikos instituto salėje.
Adresas: Savanorių pr. 231, LT-02300 Vilnius, Lietuva
Tel. +370 5 264 8884; el. paštas: office@ftmc.lt

Disertaciją galima peržiūrėti Fizinių ir technologijos mokslų centro bei Vilniaus universiteto bibliotekose ir VU interneto svetainėje adresu: https://www.vu.lt/naujienos/ivykiu-kalendorius

CONTENTS

ACKNOWLEDGEMENTS

One of the most challenging parts of this paper was definitely listing all the wonderful people who contributed one or another way during my studies as well as preparation of the thesis. There are simply too many of them. Therefore, I am firstly very grateful to **all** my dearest colleagues and friends for every kind and supporting word and advice throughout this journey. Without you, it would be hardly possible.

I would also like to express my special gratitude to my scientific supervisor Dr. Andrejus Michailovas, for providing excellent conditions for the research, his guidance, and support during the planning and development of this work.

I express my sincere gratitude to Dr. Rokas Danilevičius without whose support, endless help as well as patience, and valuable insights this study would not have been successful.

Many thanks to Dr. Karolis Viskontas for important assistance and insights with oscillators related matters. Your provided SESAMs are the heart of all investigated lasers.

I am grateful to Dr. Robertas Kananavičius for his support in developing the SFG spectrometer.

Thanks to Dr. Pierre-Marc Dansette for providing software for numerical simulations.

Thanks to Dr. Audrius Zaukevičius for consultations and valuable help with numerical modeling.

Thanks to my colleagues Raimundas Burokas, Aivaras Kazakevičius for the friendly atmosphere and support. More to add, I would like to thank Dr. Tadas Bartulevičius and Laurynas Veselis for an unforgettable experience received throughout the conference travels.

A special thanks to my brilliant wife Kristina for her thorough support and care of my well-being during the preparation of the thesis. You were the first one to see the drafts.

Last but not least, I would like to thank my parents, Palmira and Romualdas, who have always encouraged me to seek more, and sister Neringa for support and encouragement.

LIST OF ABBREVIATIONS

AGS	silver thiogallate ($AgGaS_2$)
ASE	spontaneous emission
BBO	β-barium borate (β-BaB_2O_4)
CCD	charge-coupled device
CFBG	chirped fiber Bragg grating
DFG	difference frequency generation
DUT	device under test
EOM	electro-optic modulator
EPC	electronic polarization controller
FFT	fast Fourier transform
FWHM	full width at half maximum
GS	gallium selenide (GaSe)
GVD	group-delay dispersion
GVM	group velocity mismatch
YAG	yttrium aluminum garnet
IR	infrared
KGW	potassium gadolinium tungstate
LGS	lithium gallium sulfide ($LiGaS_2$)
LGSE	lithium gallium selenide ($LiGaSe_2$)
LIDT	laser-induced damage threshold
MCT	mercury cadmium telluride (HgCdTe)
Mid-IR	middle infrared
MPE	multi-photon excitation
MPM	multi-photon microscopy
NALM	nonlinear amplifying loop mirror
NIR	near-infrared
NOPA	noncollinear optical parametric amplification
NPR	nonlinear polarization rotation
OPA	optical parametric amplification
OPCPA	optical parametric chirped pulse amplification
PDM	phase detector method
PLL	phase-locked loop
PMT	photomultiplier tube
PSD	power spectrum density
PVWC	Poynting-vector walk-off compensation
PZT	piezoelectric transducers
RA	regenerative amplifier
RRC	repetition rate controller

SC	supercontinuum
SERS	surface-enhanced Raman scattering
SESAM	semiconductor saturable absorber mirror
SFG	sum-frequency generation
SH	second-harmonic
SHG	second-harmonic generation
SPM	self-phase modulation
SRA	stimulated Raman amplification
SRS	stimulated Raman scattering
SSA	signal source analyzer
TPM	tangential phase-matching
VCO	voltage-controlled oscillator
VIS	visible
WDM	wavelength division multiplexer

INTRODUCTION

Since the beginning of the laser era in 1960 [1] throughout more than 60 years, laser technology has improved significantly. Lasers or laser systems could be found in various fields starting from the scientific centers and laboratories and going up to factories or even hospitals. With the emergence of new functionalities more and more areas of applications appear.

The history of mid-infrared (mid-IR) lasers sources is counting almost as much as the creation of the first laser. Interesting fact, that the world's second laser after the Maiman's ruby laser was actually the mid-IR solid-state laser based on uranium-doped calcium fluoride [2]. It was operating at 2.49 μm wavelength and was developed in the same year (1960). Over the decades, the need for mid-IR sources for spectroscopical applications has significantly influenced the development of traditional lasers sources which were typically operating in the continuous wave or ns regime. The emergence of broadband oscillators (Ti:Sapphire, Cr:LiSAF, Alexandrite) and their amplification in the early 90s have triggered the dawn of femtosecond technology in the visible (VIS) spectral range. These broadband laser sources altogether with newly developed nonlinear crystals with high second-order susceptibility [3] led to efficient optical parametric amplification (OPA). Femtosecond parametric amplification and frequency conversion technologies were shortly adapted to develop the near-infrared (NIR) and mid-IR sources.

One of the most attractive fields where ultrafast mid-IR sources are required is vibrational sum-frequency generation (SFG) spectroscopy. The process is based on resonant nonlinear mixing of tunable mid-IR laser radiation and visible laser pulse [4]. Active vibrational modes of the examined molecules at the interface give a resonant contribution to the sum-frequency signal. This technology is widely used for many applications [5] such as studies of molecular orientation, surface structure, chemical composition, electrochemistry of epitaxial growth, investigation of interfaces and surfaces of liquids, solids, polymers, biological membranes, and other systems. A broadband femtosecond tunable mid-IR source based on Ti:Sapphire oscillator allowed to create a system, that can avoid measurement scanning and can simultaneously record the whole spectrum of the investigated material [6]. However, the visible channel bandwidth limits the resolution of the measured spectrum. The problem is typically solved by narrowing the visible channel or by combining two lasers. Notwithstanding, the first solution is very ineffective and causes huge energy losses while the second solution requires complex synchronization.

Ultrafast laser sources at NIR spectral range have found their applications for nonlinear microscopy. The NIR laser systems are desirable especially for biological microscopy due to transparency windows of tissues at that spectral range. First femtosecond NIR systems were based on OPA and Ti:Sapphire oscillator and optimized for high energy (from tens of μJ to a few mJ) and low repetition operation (from a few to few hundred kHz). Meanwhile, the microscopy applications demand a high repetition rate (MHz level) and sub μJ level energy to increase speed, signal-to-noise ratio and avoid sample damage. With the emerge of femtosecond lasers based on Yb-doped solid-state and fiber active media, more suitable NIR systems were constructed [7], however, OPA layouts were usually quite complex. Since nonlinear microscopy often does not require tunable wavelength, the simpler discrete wavelength conversion methods can be used. One of the successfully demonstrated methods is stimulated Raman scattering [8]. However, for the femtosecond pulses, the conversion efficiency is low, for this single-pass configuration it was only a few percent. Multiple stages can increase energy, but this approach increases the system's complexity. Synchronous pump schemes were proposed to solve the efficiency problem [9], however, even for the 80 MHz pump laser source almost 4 m length cavity is required. That affects long-term stability and complicates laser integration.

The goal of this thesis was to develop laser sources for the SFG spectroscopy as well as for nonlinear microscopy which overcomes mentioned problems and are more compact, reliable, and affordable.

First of all, we concentrated our effort on the development of a hybrid optically synchronized SFG spectrometer. We started from the two-channel optically synchronized oscillator, which was used as a seed for both channels. Special attention was paid to achieve a widely tunable and broadband mid-IR channel. The modeling analysis helped to select the appropriate and most efficient OPA scheme. The SFG system was experimentally realized and characterized with a few known samples. As an alternative to an optically synchronized SFG system, we aimed to develop a simple repetition rate control technique dedicated to the narrowband channel laser oscillator. The analysis of phase noise of a different total cavity dispersion semiconductor saturable absorber mirror (SESAM) mode-locked fiber oscillators, and all-fiber repetition rate controllers let us distinguish optimal configuration. The gathered information was used to realize the synchronized oscillator.

Another aim for this thesis was dedicated to the development of a simple and robust method to convert Yb-based high repetition rate radiation into the NIR spectral range where are the tissue transparency windows. Results and analysis of supercontinuum generation experiment at low energy conditions

were used for the development of a single-pass SC seeded stimulated Raman amplification (SRA) setup. To further increase the conversion efficiency of this approach, synchronous pumping methods were investigated. The emerge of the new MHz pump laser source which exploits a novel fiber-based GHz burst formation technique allowed to design a short resonator length high repetition rate synchronously pumped layouts. Gathered information from SC and SRA experiments combined with synchronous pumping scheme and oscillator repetition rate control technique was used to investigate an efficient, robust, and compact concept of femtosecond NIR laser source applicable for nonlinear microscopy.

THE GOAL AND MAIN TASKS OF THE THESIS

The main goal of the thesis was to develop methods and technologies that allow the realization of effective and robust laser sources in the NIR and mid-IR region dedicated to microscopy and SFG spectrometer systems. The following tasks were accomplished in order to achieve the objective:

1. Design of broadband tunable femtosecond mid-IR source for SFG spectrometry and demonstration of the fully functional optically synchronized hybrid SFG spectrometer setup.
2. Investigation of phase noise of free-running ultrafast SESAM mode-locked Yb-doped fiber lasers with the different total cavity dispersion to distinguish the optimal configuration for low timing jitter frequency locking.
3. Testing and optimization of all-fiber phase shifters dedicated for integration in repetition rate locked oscillator setups. Realization of oscillator repetition rate locking to external clock and characterization of the assembled system.
4. Investigation and optimization of SC generation in various crystals at 1 MHz repetition rate and low (<1μJ) pump pulse energy in order to shift the Yb-based laser wavelength to transparency windows of the biological tissues.
5. Study of Yb-based laser sources wavelength conversion methods to NIR spectral region based on SC seeded SRA layouts dedicated to constructing compact, robust, and efficient source for nonlinear microscopy.

SCIENTIFIC NOVELTY

The scientific novelty of this work lies in the successfully incorporated solid-state and fiber technologies which allowed the realization of the hybrid mid-IR SFG spectrometer, synchronized fiber oscillator, and effective NIR laser source:

1. A novel optically synchronized high-resolution broadband widely tunable mid-IR SFG spectrometer setup based on an all-fiber two-channel oscillator as a seed source for broadband and narrowband pulse generation was proposed and experimentally demonstrated. This approach eliminates the need for two synchronized laser sources or very

ineffective spectral narrowing techniques, therefore, greatly simplifies the spectrometer setup.

2. A method to increase the response speed of a refractive index modulation-based Er-doped fiber phase shifter by incorporating a feedback loop that changes the effective lifetime of excited atoms was proposed and experimentally investigated.

3. Repetition rate locked all-fiber ultrafast Yb-based SESAM mode-locked fiber oscillator exploiting an Er-doped fiber-based phase shifter was presented. This was the first demonstration of such an approach for the Yb-doped SESAM mode-locked fiber oscillator locking to the external clock.

4. The realization of a low-energy femtosecond 1 MHz repetition rate Yb-doped fiber laser wavelength conversion to the NIR region based on the supercontinuum (SC) seeded SRA approach was demonstrated for the first time, which allowed to increase conversion efficiency and the realization of a compact NIR laser setup.

5. A novel compact synchronously pumped wavelength conversion to NIR setup concept based on SRA, which employs GHz burst pump laser, self-seeded SRA technique, and all-fiber repetition rate control method was proposed and numerically investigated.

PRACTICAL VALUE

The improvements and development of wavelength conversion methods altogether with the incorporation of robust fiber-based lasers and technologies enable the creation of compact, reliable, efficient, and affordable ultrashort laser sources in NIR and mid-IR spectral regions dedicated for the spectroscopy and nonlinear microscopy applications.

This work has a practical value in several aspects:

1. A novel optically synchronized hybrid broadband high-resolution mid-IR SFG spectrometer setup was successfully demonstrated. The validation of the system with a few samples led to the implementation of this approach into a fully functional SFG spectrometer system which is ready for prototyping.

2. The combination of low total cavity dispersion fiber oscillator and Er-doped fiber-based phase shifter allowed to develop compact and robust seed source, which can be integrated into high-power high-energy laser

systems and allows to lock repetition rate of such systems to the external clock with a low total timing jitter. The commercial laser systems exploiting such seed sources are already available at the company Ekspla.

3. The combination of synchronous pumping, GHz pump laser, self-seeded SRA, and all-fiber repetition rate locking technologies paved a way to develop a robust, very compact, and efficient femtosecond NIR laser source that can be implemented into commercial low energy lasers systems dedicated for nonlinear microscopy.

STATEMENTS TO DEFEND

S1. Optically synchronized broadband hybrid mid-IR spectrometer with a high spectral resolution of <3 cm^{-1}, tuning range from 2 μm to 10 μm, and broad bandwidth up to 850 cm^{-1} can be realized by exploiting two-channel fiber laser with subsequent amplification in narrowband picosecond Nd:YVO_4 regenerative amplifier and in broadband multiple-stage mid-IR OPA based on efficient low-energy supercontinuum seed pre-amplification in BBO crystal.

S2. The frequency response speed of the refractive index modulation based Er-doped fiber phase shifter can be increased by incorporating a feedback loop that changes the effective lifetime of excited ions of the active media which allows using this method as an alternative to conventional piezo-based phase shifter in a low timing jitter repetition rate locked ultrafast Yb-based SESAM mode-locked all-fiber oscillator.

S3. A reliable, compact, and efficient method for μJ-level 1 μm femtosecond laser wavelength conversion to biological tissues transparent (1.1-1.35 μm) NIR region can be achieved by exploiting SC generation and subsequent amplification in stimulated Raman scattering active crystals.

AUTHOR'S CONTRIBUTION

All the research presented in the thesis was performed by the author except the work mentioned in the co-author's contribution section. The author constructed or contributed to the construction of all laser systems described in A1-A4 articles. The author prepared the manuscripts of A1-A4 articles. Furthermore, the author performed numerical simulations and the theoretical analysis of the research presented in the proposed articles and this thesis.

CO-AUTHOR'S CONTRIBUTION

- Dr. Andrejus Michailovas was a supervisor of the author's PhD studies, provided excellent conditions for the research and suggested significant ideas for the work published in the A3 article, and organized the process of P1 patenting.
- Dr. Rokas Danilevičius suggested ideas and made a great contribution in preparing manuscripts for A1 and A2 publications. Furthermore, Rokas provided consultations and shared his experience in order to achieve success in this work.
- Dr. Karolis Viskontas contributed to the construction and characterization of fiber lasers described in A2. In addition to this, he made a great contribution in preparing the article manuscript.
- Dr. Robertas Kananavičius built the spectrometer setup and helped to realize and evaluate the SFG spectrometer system. Furthermore, he shared his experience and insights that helped in preparing the manuscript for article A1.
- Dr. Regimantas Januškevičius contributed to preparing the manuscript for article A1 and participated in the validation of the SFG spectrometer system.
- Rokas Jutas helped to perform SC generation and SRA measurements which are presented in A3.
- Dr. Tadas Bartulevičius developed a GHz repetition rate pump laser described in P1 and shared his experience in performing experimental work.
- Virginija Petrauskienė has done valuable work in making the descriptions of P1.
- Dr. Valdas Girdauskas performed the numerical analysis of the synchronously pumped Raman amplifier.
- Dr. Pierre-Marc Dansette and PhD stud. Maksim Eremchev developed and analyzed NIR OPA presented in A3.
- Dr. Audrius Zaukevičius and PhD stud. Laurynas Veselis advised on various issues of laser technology and shared their experience in performing numerical simulations and experimental work.

SCIENTIFIC PAPERS

Publications related to the topic of the thesis:

A1. **K. Madeikis**, R. Kananavicius, R. Danilevicius, A. Zaukevicius, R. Januskevicius, and A. Michailovas, "Hybrid high spectral resolution broadband mid-infrared SFG spectrometer development and demonstration," Opt. Express **29**, 25344-25357 (2021). DOI: 10.1364/OE.433617.

A2. **K. Madeikis**, K. Viskontas, R. Danilevičius, and A. Michailovas, "All-optical repetition rate stabilization methods for ultrafast Yb-based SESAM mode-locked fiber oscillator," Opt. Fiber Technol. **65**, 102636 (2021). DOI: 10.1016/j.yofte.2021.102636.

A3. **K. Madeikis**, P. Dansette, T. Bartulevičius, L. Veselis, R. Jutas, M. Eremchev, R. Danilevičius, V. Girdauskas, and A. Michailovas, "Investigation of materials for supercontinuum generation for subsequent nonlinear parametrical and Raman amplification at 1 MHz repetition rate," Opt. Laser Technol. **143**, 107373 (2021). DOI: 10.1016/j.optlastec.2021.107373.

Conference proceedings related to the topic of the thesis:

A4. **K. Madeikis**, R. Danilevicius, A. Zaukevicius, T. Bartulevicius, L. Veselis, A. Michailovas, "Compact broadband femtosecond MIR source for hybrid sum frequency generation spectroscopy systems", Proc. SPIE **11264**, 112641Q (2020). DOI: 10.1117/12.2544911.

Other publications:

A5. T. Bartulevicius, L. Veselis, **K. Madeikis**, A. Michailovas, and N. Rusteika, “Compact femtosecond 10 μJ pulse energy fiber laser with a CFBG stretcher and CVBG compressor,” Opt. Fiber Technol. **45**, 77-80 (2018). DOI: 10.1016/j.yofte.2018.06.006.

A6. L. Veselis, T. Bartulevicius, **K. Madeikis**, A. Michailovas, and N. Rusteika, “Compact 20 W femtosecond laser system based on fiber laser seeder, Yb:YAG rod amplifier and chirped volume Bragg grating compressor,” Opt. Express **26**, 31873-31879 (2018). DOI: 10.1364/OE.26.031873.

A7. T. Bartulevicius, **K. Madeikis**, L. Veselis, V. Petrauskiene, and A. Michailovas, “Active fiber loop for synthesizing GHz bursts of

equidistant ultrashort pulses," Opt. Express **28**, 13059-13067 (2020). DOI: 10.1364/OE.389056.

Other conference proceedings:

A8. T. Bartulevičius, **K. Madeikis**, L. Veselis, A. Michailovas, "Compact high-power GHz intra-burst repetition rate all-in-fiber CPA system with LMA fiber power amplifier," Proc. SPIE **11260**, 112602F (2020). DOI: 10.1117/12.2545665.

A9. L. Veselis, T. Bartulevicius. **K. Madeikis**, A. Michailovas „Generation of 40 W, 400 fs pulses at 1 MHz repetition rate from efficient, room temperature Yb:YAG double-pass amplifier seeded by fiber CPA system", Proc. SPIE **11259**, 1125925 (2020). DOI: 10.1117/12.2545473.

PATENTS

P1. A. Michailovas, **K. Madeikis**, T. Bartulevicius, Lazeris netiesinei mikroskopijai. Application number: LT2020 526.

CONFERENCE PRESENTATIONS

Presentations directly related to the topic of the thesis:

C1. **K. Madeikis**, K. Viskontas, R. Danilevicius, T. Bartulevičius, L. Veselis, A. Michailovas and N. Rusteika, "Optical Repetition Rate Locking of Ultrafast SESAM-Based Yb-Doped All-Fiber Oscillator for High Intensity OPCPA Systems", CLEO 2018.

C2. **K. Madeikis**, K. Viskontas, R. Danilevicius, T. Bartulevičius, L. Veselis, A. Michailovas and N. Rusteika, "Optical Repetition Rate Locking of Ultrafast Yb Doped All Fiber Oscillator for High Intensity OPCPA Systems", Laser Optics 2018.

C3. **K. Madeikis**, K. Viskontas, R. Danilevicius, T. Bartulevičius, L. Veselis, A. Michailovas and N. Rusteika, "All-Optical Repetition Rate Stabilization of Ultrafast SESAM-Based Yb Doped All Fiber Oscillator for High Intensity OPCPA Systems", Laser Precision Microfabrication Symposium 2018.

C4. **K. Madeikis**, K. Viskontas, R. Danilevicius, T. Bartulevičius, L. Veselis, A. Michailovas and N. Rusteika, "All-Optical Repetition Rate Stabilization of Ultrafast Yb Doped All Fiber Oscillator for High Intensity OPCPA Systems", Europhoton 2018.

C5. **K. Madeikis**, K. Viskontas, R. Danilevicius, T. Bartulevičius, L. Veselis, A. Michailovas and N. Rusteika, “Optinis Skaidulinio Užkrato Šaltinio Pasikartojimo Dažnio Stabilizavimas”, FizTech 2018.

C6. **K. Madeikis**, K. Viskontas, R. Danilevicius, T. Bartulevičius, L. Veselis, N. Rusteika and A. Michailovas, “Optical Repetition Rate Stabilization Techniques of Ultrafast Yb Doped All Fiber Oscillator”, CLEO Europe 2019.

C7. **K. Madeikis**, K. Viskontas, R. Danilevicius, T. Bartulevičius, L. Veselis and A. Michailovas, “Optical Repetition Rate Stabilization Techniques of Ultrafast Yb Doped All Fiber Oscillator”, Siegman International Summer School on Lasers 2019.

C8. **K. Madeikis**, K. Viskontas, R. Danilevicius, T. Bartulevičius, L. Veselis and A. Michailovas, “Optiniai Yb legiruoto skaidulinio užkrato šaltinio pasikartojimo dažnio stabilizavimo metodai”, LNFK 43 2019.

C9. **K. Madeikis**, R. Danilevicius, T. Bartulevičius, L. Veselis and A. Michailovas, “Kompaktiškas plačiajuostis femtosekundinis MIR šaltinis SDG spektroskopijai”, FizTech 2019.

C10. **K. Madeikis**, R. Danilevicius, A. Zaukevicius, T. Bartulevicius, L. Veselis, A. Michailovas, "Compact broadband femtosecond MIR source for hybrid sum frequency generation spectroscopy systems", SPIE LASE 2020.

THE STRUCTURE OF THE THESIS

The material of this thesis is divided into four main parts. At first, the principles, origin, and technologies relevant to this work, that are widely used to generate NIR and mid-IR radiation are described in Chapter 1. The following chapters begin with the literature review related to the topic of the research. Chapter 2 is dedicated to present the development and realization of the hybrid optically synchronized broadband widely tunable mid-IR SFG system. An approach of the all-fiber repetition rate control technique demonstration is presented in Chapter 3. Finally, a new concept of a synchronously pumped SRA-based NIR laser system is presented in Chapter 4.

CHAPTER 1

GENERAL INTRODUCTION

This chapter is dedicated to an overview of the principles and origin of mostly used effects, methods, and technologies required for wavelength conversion to ultrashort near and middle-infrared radiation.

1.1 Nonlinear polarization

If the low-intensity light interacts with material, the light-induced response linearly depends on the intensity of the incident light. In this linear optical regime the properties of the material such as refractive index, absorption coefficient does not depend on the light intensity, meanwhile the induced polarization $P(t)$ dependency on external field $E(t)$ is described by [10–12]:

$$P(t) = \epsilon_0 \chi^{(1)} E(t), \tag{1.1}$$

where the ϵ_0 is the permittivity of free space and $\chi^{(1)}$ is known as linear susceptibility. If the intensity of incident light is high enough, the properties of the material modify. In this nonlinear optical regime, induced polarization will include additional terms which depend on higher orders of incident light intensity. In this case, with the assumption that the induced polarization is weak, the $P(t)$ can be expanded into a Taylor series of field strength $E(t)$ [10]:

$$\begin{aligned} P(t) &= \epsilon_0 \left[\chi^{(1)} E(t) + \chi^{(2)} E^2(t) + \chi^{(3)} E^3(t) + \cdots \right] \\ &= P^{(1)}(t) + P^{(2)}(t) + P^{(3)}(t) + \cdots \\ &= P^{(1)}(t) + P^{NL}(t), \end{aligned} \tag{1.2}$$

where $\chi^{(2)}$ and $\chi^{(3)}$ are the second- and third-order nonlinear optical susceptibilities, $P^{(2)}(t)$ and $P^{(3)}(t)$ are the second- and third-order nonlinear polarization, respectively. The second-order polarization allows the three-wave mixing processes in the media: second harmonic generation (SHG), sum and difference frequency generation (SFG, DFG), optical parametric amplification (OPA), and optical rectification (OR). Since all even-order nonlinear susceptibilities vanish in the centrosymmetric media, the above-mentioned processes can occur only in the media with no inversion symmetry. The third-order polarization gives rise to a four-wave mixing process, self- and cross-phase modulation, self-focusing, optical phase conjugation,

stimulated Raman scattering, and third-harmonic generation. These third-order interactions can occur in any material regardless of its spatial symmetry.

When the nonlinear polarization is induced in the material, it acts as a source of new frequency electromagnetic waves. For nonlinear media that is unmagnetized, with no free charges and currents, the propagation of light can be expressed by the general form of the wave equation [10–12]:

$$\nabla^2 E - \frac{n^2}{c^2}\frac{\partial^2 E}{\partial t^2} = \frac{1}{\epsilon_0 c^2}\frac{\partial^2 P^{NL}}{\partial t^2}, \tag{1.3}$$

where E is the electric field strength, n is the refractive index of the material, c is the speed of light in a vacuum, and P^{NL} is the nonlinear polarization. From this equation with the slowly varying amplitude approximation, we can derive a coupled-wave equation which will be described in later sections. It represents how the complex amplitudes of interacting waves change as a result of nonlinear interaction in media.

1.2 Difference frequency generation and optical parametric amplification

There are two basic nonlinear down-conversion methods widely used: optical parametric amplification and difference frequency generation [10–12]. Both of them are based on a three-wave process that exploits second-order nonlinearity ($\chi^{(2)}$) of the optical material. The main difference between OPA and DFG is that the DFG requires two powerful input sources while OPA requires only one pump source and a weak seed signal.

For both processes energy (1.4) and momentum (1.5) conservation laws must be satisfied [13]:

$$\hbar\omega_p = \hbar\omega_s + \hbar\omega_i, \tag{1.4}$$

$$\hbar\vec{k}_p = \hbar\vec{k}_s + \hbar\vec{k}_i. \tag{1.5}$$

Herein, ω_p, ω_s, ω_i are so-called pump, signal, and idler angular frequencies. Respectively, $\vec{k}_p$, $\vec{k}_s$, $\vec{k}_i$ are wave vectors of the pump, signal, and idler, and $\hbar$ is the Planck's constant divided by 2π. In the DFG case, the idler wave is equal to the DFG wave, therefore, $\omega_{DFG} = \omega_i = \omega_p - \omega_s$.

The interaction of three waves in the collinear geometry of OPA/DFG for lossless media is defined by the coupled amplitude equations [13]:

$$\frac{\partial A_s}{\partial z} = -i\frac{\omega_s d_{eff}}{n_s c} A_i^* A_p \exp(-i\Delta k z), \tag{1.6}$$

$$\frac{\partial A_i}{\partial z} = -i\frac{\omega_i d_{eff}}{n_i c} A_s^* A_p \exp(-i\Delta kz), \tag{1.7}$$

$$\frac{\partial A_p}{\partial z} = -i\frac{\omega_p d_{eff}}{n_p c} A_s^* A_i \exp(-i\Delta kz), \tag{1.8}$$

where A_s, A_i, A_p are the signal, idler, and pump wave amplitudes, d_{eff} is the effective nonlinear optical coefficient, which depends on propagation direction and polarization of the three beams, n_s, n_i, n_p are the refractive indexes, c is the speed of light, and $\Delta k = k_p - k_s - k_i$ is the wave-vector mismatch.

These three coupled equations (1.6)-(1.8) could be solved for monochromatic beams and cast into the form also known as Manley-Rowe relations [13]:

$$\frac{1}{\omega_i}\frac{dI_i}{dz} = \frac{1}{\omega_s}\frac{dI_s}{dz} = -\frac{1}{\omega_p}\frac{dI_p}{dz}, \tag{1.9}$$

where I_i, I_s, I_p are the intensities of the three waves. It shows that three-wave interaction in ($\chi^{(2)}$) media manifest in energy flow from higher frequency field to two lower frequency fields or vice versa. For OPA and DFG cases, the energy is transferred from a stronger pump beam to the less powerful signal and newly generated idler/DFG beam.

By assuming that the initial signal intensity is I_{s0}, no initial idler beam is present ($I_{i0} = 0$), and there is no pump depletion ($I_p \cong const.$), equations (1.6)-(1.8) can be solved to describe the change of the signal and idler intensities after propagating a length L of nonlinear crystal [13]:

$$I_s(L) = I_{s0}\left[1 + \frac{\Gamma^2}{g^2} sinh^2(gL)\right], \tag{1.10}$$

$$I_i(L) = I_{s0}\frac{\omega_i}{\omega_s}\frac{\Gamma^2}{g^2} sinh^2(gL), \tag{1.11}$$

in which

$$g = \sqrt{\Gamma^2 - \left(\frac{\Delta k}{2}\right)^2}, \tag{1.12}$$

$$\Gamma^2 = \frac{2\omega_i\omega_s d_{eff}^2 I_p}{n_i n_s n_p \varepsilon_0 c^3} = \frac{8\pi^2 d_{eff}^2 I_p}{n_i n_s n_p \lambda_i \lambda_s \varepsilon_0 c}, \tag{1.13}$$

where Γ is the nonlinear coefficient and ε_0 is the vacuum permittivity. The equations above could be simplified considering the large gain approximation ($\Gamma L \gg 1$) and the case of perfect phase-matching ($\Delta k = 0$) [13]:

$$I_s(L) \cong \frac{1}{4} I_{s0} exp(2\Gamma L), \tag{1.14}$$

$$I_i(L) \cong \frac{\omega_i}{4\omega_s} I_{s0} exp(2\Gamma L). \tag{1.15}$$

The ratio of signal and idler intensities is such, that it corresponds to the same number of the generated signal and idler photons. The parametric gain is defined by the equation [13]:

$$G = \frac{I_s(L)}{I_{s0}} = \frac{1}{4} exp(2\Gamma L). \tag{1.16}$$

The maximal gain of the parametric amplification will be achieved once the perfect phase-matching conditions ($\Delta k = 0$) are fulfilled. Since the $\Delta k = k_p - k_s - k_i$ where $k_j = n_j \omega_j / c$, it can be expressed in a further form [13]:

$$n_p = \frac{n_i \omega_i + n_s \omega_s}{\omega_p}. \tag{1.17}$$

This condition can be fulfilled in some birefringent crystals where two different transmission modes are available. Two waves of the same frequency, but perpendicular in polarization, can propagate the nonlinear crystal with different phase velocities. Those are so-called ordinary ("o") and extraordinary ("e") waves, which have a different refractive index. Meanwhile, for the extraordinary wave, it additionally depends on the propagation direction. In the case of negative uniaxial crystals ($n_e < n_o$), which are commonly used in femtosecond OPA's, perfect phase-matching condition (1.14) can be satisfied only if the pump wave is polarized along the extraordinary direction [13]. If signal and idler beams have the same ordinary polarization ($o_s + o_i \rightarrow e_p$), it is called the Type I phase-matching. If one of the waves is polarized parallelly to the pump beam ($e_s + o_i \rightarrow e_p$ or $o_s + e_i \rightarrow e_p$), it is called the Type II phase-matching.

Typically, the phase-matching is achieved by adjusting the temperature [14] or by changing the angle θ_m between the wave vector of the propagating beams and the optical axis of the nonlinear crystal. For Type I uniaxial crystal this angle can be obtained as [13]:

$$\theta_m = asin\left[\frac{n_{ep}}{n_{ep}(\theta_m)} \sqrt{\frac{n_{op}^2 - n_{ep}^2(\theta_m)}{n_{op}^2 - n_{ep}^2}}\right], \tag{1.18}$$

where n_{ep} and n_{op} are the principal extraordinary and ordinary refractive indexes for the pump radiation.

1.3 Optical parametric amplification of ultrashort pulses

In the case of femtosecond OPA, when the short pulse is propagating in the nonlinear crystal, temporal dependence must be taken into account [10–12]. Therefore, coupled amplitude equations (1.6)-(1.8) change to [13]:

$$\frac{\partial A_s}{\partial z}+\frac{1}{v_{gs}}\frac{\partial A_s}{\partial t}=-i\frac{\omega_s d_{eff}}{n_s c}A_i^* A_p \exp(-i\Delta kz), \tag{1.19}$$

$$\frac{\partial A_i}{\partial z}+\frac{1}{v_{gi}}\frac{\partial A_i}{\partial t}=-i\frac{\omega_i d_{eff}}{n_i c}A_s^* A_p \exp(-i\Delta kz), \tag{1.20}$$

$$\frac{\partial A_p}{\partial z}+\frac{1}{v_{gp}}\frac{\partial A_p}{\partial t}=-i\frac{\omega_p d_{eff}}{n_p c}A_s^* A_i \exp(-i\Delta kz), \tag{1.21}$$

where v_{gs}, v_{gi}, v_{gp} are the group velocities of the signal, idler, and pump waves respectively.

The main issues of OPA with ultrashort pulses are related to group velocity mismatch (GVM) between interacting pulses. Due to short duration and different speeds, pulses are temporally separated after a certain propagation length after which amplification stops. This interaction length is limited by the GVM of the pump and signal/idler beams, and can be calculated using the following equation [13]:

$$l_{jp}=\frac{\tau}{\delta_{jp}}, \qquad j=s,i, \tag{1.22}$$

where τ is the pump pulse duration and the $\delta_{jp}=1/v_{gj}-1/v_{gp}$ is the GVM between the pump and signal/idler.

The GVM between the signal and the idler wave limits the phase-matching bandwidth. In order to achieve the broadest amplification, GVM has to be as small as possible over the wide frequency range. Assuming that the central signal frequency fulfills perfect phase-matching condition and Δk is approximated to the first order of the Taylor expansion, phase-matching bandwidth at full width at half maximum (FWHM) within the large gain approximation can be calculated as [13]:

$$\Delta v \cong \frac{2\sqrt{ln2}}{\pi}\left(\frac{\Gamma}{L}\right)^{\frac{1}{2}}\frac{1}{\left|\frac{1}{v_{gs}}-\frac{1}{v_{gi}}\right|}. \tag{1.23}$$

It shows, that the gain bandwidth is inversely proportional to GVM. When the group velocity mismatch is similar ($v_{gs}=v_{gi}$) or the OPA approaches degeneracy ($\omega_s \to \omega_i$) in Type I phase-matching, the bandwidth increases

rapidly and equation (1.23) loses validity, therefore wave vector mismatch has to be expanded to the second-order, giving the further equation [13]:

$$\Delta v = \frac{2\sqrt[4]{ln2}}{\pi}\left(\frac{\Gamma}{L}\right)^{\frac{1}{4}} \frac{1}{\left|\frac{\partial^2 k_s}{\partial \omega_s^2} + \frac{\partial^2 k_i}{\partial \omega_i^2}\right|}. \tag{1.24}$$

For Type I interaction the bandwidth is wider, therefore this configuration is used to achieve the shortest pulse duration [13], meanwhile, Type II interaction is used to obtain a wider tuning range [15].

The breakthrough in the achievable bandwidth was reached when the noncollinear optical parametric amplification (NOPA) technology was developed [16]. In NOPA configuration, pump and signal beams cross at an angle α, at which phase-matching angle can be constant for signal wavelength in wide range. The idler wave is generated at the angle Ω with respect to the signal, which adjusts itself to satisfy the phase-matching condition (Fig. 1.1(a)). For a collinear geometry, signal and idler beams moving at different group velocities get quickly separated (Fig. 1.1(b)), meanwhile in NOPA case a broadband phase-matching can be realized for such angle Ω that the signal group velocity is equal to the projection of idler group velocity ($v_{gs} = v_{gi}\cos\Omega$) [13], as shown in Fig. 1.1(c). This can be satisfied only if the ($v_{gi} > v_{gs}$). In practice, it is more convenient to know the angle α between signal and pump at such conditions, using the following equation [13]:

$$\alpha = \sin^{-1}\sqrt{\frac{1-\frac{v_{gs}^2}{v_{gi}^2}}{1+\frac{2v_{gs}n_s\lambda_i}{v_{gi}n_i\lambda_s}+\frac{n_s^2\lambda_i^2}{n_i^2\lambda_s^2}}}. \tag{1.25}$$

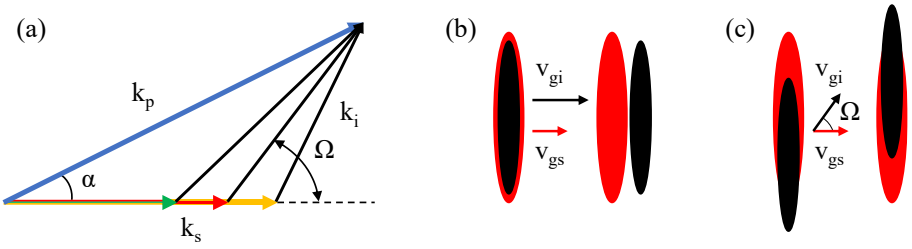

Fig. 1.1. a) Schematic of NOPA. **b)** Signal and idler propagation in OPA. **c)** Signal and idler propagation in NOPA.

An example of phase-matching angle dependence on the wavelength of Type I BBO (β-BaB_2O_4) pumped at 532 nm in collinear ($\alpha = 0°$) and

noncollinear ($\alpha = 2.4°$) configuration is presented in Fig. 1.2. At the NOPA configuration, when the $\alpha = 2.4°$, phase-matching angle is almost a constant over the 700-1000 nm spectral range, therefore ultra-broad amplification bandwidth can be achieved.

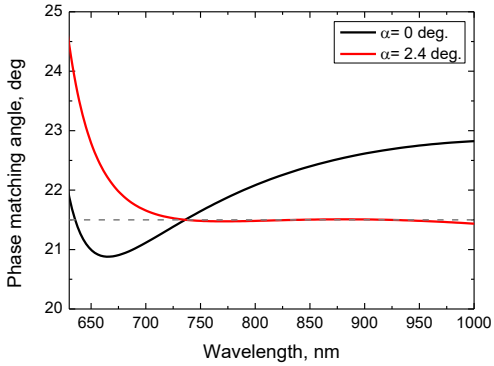

Fig. 1.2. Phase-matching curves in the case of collinear ($\alpha = 0°$) and noncolinear ($\alpha = 2.4°$) geometry for Type I BBO crystal pumped at 532 nm wavelength.

1.4 Sum-frequency generation

Another three-wave parametric interaction process is the sum-frequency generation (SFG) [10–12]. In this case two lower frequency photons at ω_1 and ω_2 are combined to produce a higher energy photon at ω_3 (frequency upconversion). To exploit the SFG process, energy conservation law must be satisfied:

$$\hbar\omega_{SFG} = \hbar\omega_3 = \hbar\omega_1 + \hbar\omega_2. \quad (1.26)$$

In the degenerate SFG case, when the $\omega_1 = \omega_2$, second harmonic (SH) is generated, $\omega_{SFG} = \omega_{SH} = 2\omega_1$. SFG, as well as OPA or DFG, requires crystal materials with a non-centrosymmetric crystal structure where $\chi^{(2)} \neq 0$, and is forbidden under electric-dipole approximation in the bulk of centrosymmetric non-chiral media where $\chi^{(2)} = 0$ [10].

1.5 Spontaneous and stimulated Raman scattering

When the beam of light illuminates the material sample a portion of the light is inelastically scattered. The scattering process which occurs due to the excitation or de-excitation of the material (because of interaction with the vibrational mode) is called spontaneous Raman scattering [10–12]. The scattered light contains frequencies different from the incident (ω_p) ones. The wavelength shift is the property of the material defining vibrational mode:

$\omega_v = \omega_p - \omega_S$. When the incident photon loses the energy to excite the material and shifts to the lower frequencies (ω_S), it is called the Stokes shift. Meanwhile, when the incident photon gains the energy from the excited state of the material and shifts to the higher frequencies (ω_{AS}), it is called the anti-Stokes shift. The scattered light is called the Stokes and the anti-Stokes wave respectively. Graphical illustration of energy level diagrams for both processes is presented in Fig. 1.3. The anti-Stokes lines are much weaker than the Stokes lines because the population of the level E_v is smaller than in level E_0 by the Boltzmann factor $exp(-\hbar\omega_v/kT)$ in thermal equilibrium conditions.

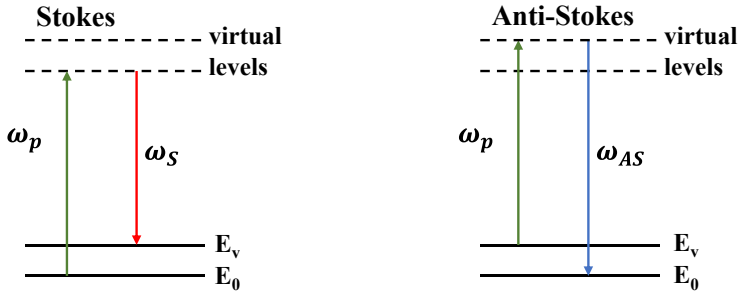

Fig. 1.3. Energy level diagrams describing the Stokes (on the left) and the anti-Stokes (on the right) shift.

The spontaneous Raman scattering is a very weak process, however, under high incidence beam energy stimulated Raman scattering (SRS) can occur [17]. In this case, the material interacts with the two different frequency ω_p and ω_S photons. At first, ω_S photon is generated via spontaneous Raman scattering, then this photon stimulates the emission of another same frequency photon. In a quite intense pump laser field, this evolves in a directed coherently amplified radiation of the Stokes waves. This process is also known as stimulated Raman amplification (SRA). If the intensity of the amplified Stokes wave becomes sufficiently high, it can act as a new pump wave and generate another Stokes wave ($\omega_{s2} = \omega_{s1} - \omega_v = \omega_p - 2\omega_v$), meaning multiple scattering orders are available.

The SRS process is treated as effective $\chi^{(3)}$ interaction given by [18]:

$$\chi^{(3)} = \chi^{(3)NR} + \chi^{(3)R}, \quad (1.27)$$

where $\chi^{(3)NR}$ and $\chi^{(3)R}$ are electronic and vibrational responses respectively.

The $\chi^{(3)NR}$ is responsible for self-focusing, self-phase modulation, etc., but has no direct effect on SRS. Meanwhile, the $\chi^{(3)R}$ causes energy transfer between the pump and the Stokes waves, thus is responsible for SRS.

The vibrational mode of the molecules can be interpreted as a harmonic oscillator of resonance frequency ω_v and damping constant γ, meanwhile $q(t)$ is the deviation of the internuclear distance from its equilibrium value q_0. The optical polarizability of such molecule depends on the internuclear separation $q(t)$ and can be expressed by [18]:

$$\alpha(t) = \alpha_0 + \left(\frac{\partial \alpha}{\partial q}\right)_0 q(t), \tag{1.28}$$

where α_0 is the polarizability of a molecule in which the internuclear distance is held at its equilibrium value. When the molecule is set to oscillation, its polarizability is modulated in time, therefore the refractive index of N coherently oscillating molecules will be modulated in time [18]:

$$n(t) = \sqrt{\epsilon(t)} = \sqrt{1 + N\alpha(t)}, \tag{1.29}$$

Due to temporal modulation of the refractive index, the passing beam of light will be modified and sidebands from incident light at $\pm\omega_v$ will appear.

The SRS process can be described as follows: first of all, the molecular vibrations modify the refractive index of the material, which leads to the creation of the frequency sidebands separated from the incidence beam by a $\pm\omega_v$. Then the Stokes wave at a frequency ω_S can beat the pump wave ω_p to produce a modulation of the total intensity which coherently excites the molecular oscillation ($\omega_v = \omega_p - \omega_s$). These two processes reinforce each other, which leads to a stronger molecular vibration. The resonance Raman susceptibility is given by [18]:

$$\chi^{(3)R}(\omega_S) = \frac{\epsilon_0 \frac{N}{6m}\left(\frac{\partial \alpha}{\partial q}\right)_0^2}{\omega_v^2 - \left(\omega_p - \omega_s\right)^2 + 2i\left(\omega_p - \omega_s\right)\gamma}, \tag{1.30}$$

where m is the reduced nuclear mass. The Raman susceptibility can be expressed by real and imaginary parts $\chi^{(3)R}(\omega_S) = \chi^{(3)R'}(\omega_S) + \chi^{(3)R''}(\omega_S)$.

In the undepleted pump approximation the Stokes intensity on propagation length z can be given by [19]:

$$I_S(z) = I_S(0)e^{g_R I_p z}, \tag{1.31}$$

where g_R is the Raman gain intensity factor given by [19]:

$$g_R = \frac{3\omega_s}{n_s n_p \varepsilon_0 c^2}\left|Im\left(\chi^{(3)R}\right)\right|. \tag{1.32}$$

CHAPTER 2

MID-IR SUM-FREQUENCY GENERATION SPECTROMETER

The literature review of this chapter is dedicated to a discussion of the surface spectroscopy techniques (SHG and SFG), their development, and a few of many possible applications. Comparison of narrowband, broadband, and hybrid SFG spectrometers, as well as the advantages and shortcomings of each system, are also introduced.

The development, experimental realization, and characterization of a hybrid optically synchronized high-resolution broadband mid-IR SFG spectrometer are presented in the experimental section of this chapter.

2.1 Literature review

2.1.1. Development of spectroscopy techniques for surface studies

Soon after the beginning of nonlinear optics when the SH generation was observed in quartz [20], the importance of boundary effects for optical wave mixing in the condensed matter was realized [21]. It was perceived that at the boundary of two media, the layer of the surface had a nonlinearity different from the bulk due to the field discontinuity across the surface, and due to the presence of surface states, which might be dominant [22], but it was not possible to distinguish them experimentally at the time. Early experiments of surface SHG considered that adsorbates on a surface were not detectible. Due to limited knowledge on surface nonlinearity versus surface structure, the structural difference between the bulk and surface was ignored. The first observation of surface composition dependency on SHG signal was made by Chen et al. in [23]. He reported, that the signal of reflected SHG from Ge surface in ultrahigh vacuum showed a significant difference upon a thickness of Na layer on the surface. However, the interest of the scientific community was oriented in the nonlinear optical processes, therefore investigation of the surface structure by using nonlinear optics was not a field of interest at the time.

The discovery of surface-enhanced Raman scattering (SERS) from molecules on roughened Ag [24] triggered active researches on surface SFG.

It was believed, that enhancement arises from the enhanced surface field due to local surface plasmon resonance and due to resonance at the charge-transfer band created by molecule-metal interaction [25]. It was soon realized, that Raman scattering and SHG should experience similar local field enhancement, which was shortly confirmed by Chenson Chen et al. [26]. The subsequent experiments showed, that even centrosymmetric molecules could be detected [27]. It was shown, that 20 mW CW laser was enough for the SHG measurement [28] what leads to a conclusion, that even without surface enhancement, a surface monolayer could be detected if a pulsed laser were used. Positive results encouraged the quest of using SHG to probe surfaces.

Theory of surface SHG [29–31] suggests, that the reflected SHG signal is proportional to the surface ($\chi_s^{(2)}$) and bulk ($\chi_B^{(2)}$) nonlinear susceptibilities. If the medium has the inversion symmetry, nonlinearity of bulk should wannish under the electric-dipole approximation, meanwhile at the interface the centrosymmetry is broken and the nonlinear susceptibility of the surface or interface $\chi_s^{(2)} \neq 0$. Due to suppression of $\chi_B^{(2)}$, the signal induced only by χ_s^2 could be measured. The experiment has shown, that surface SHG is sensitive enough to measure the electronic spectrum of an adsorbed monolayer [32] and its average orientation [33]. In other attempts, it was shown that SHG could be applied to a variety of fields, for example, to study monolayer polymerization [34], soluble molecules at air/liquid interfaces [35], surface-induced alignment and polar ordering of liquid crystals [36], surface magnetization [37], 2D phase transitions of a Langmuir monolayer on water [38], and many more [39,40]. In order to expand SHG capabilities, tunable input could be used for measurement. That allows to measure electronic transition of surface molecules [32], however, electronic resonance bands are often too broad to distinguish molecular species. More informative vibrational spectra (known as fingerprints of molecules) in the IR region are required to identify or selectively probe surface structures or molecules. Unfortunately, SHG cannot be used directly due to a lack of sensitive IR detectors. To overcome this limitation, SHG has to be expanded to IR-visible SFG. SFG, as well as SHG, can be surface-specific, furthermore, tunable IR input allows probing of vibrational resonances.

At the beginning of the SFG spectroscopy, tunable OPA systems were rare in the research labs, therefore the first demonstration of IR-visible SFG spectroscopy was on a coumarin dye monolayer on Si using a pulsed CO_2 laser, discretely tunable at ~10 μm, in synchronization with an Nd:YAG laser which SH at 0.53 μm was used for the visible channel [41]. Several vibrational modes of coumarin were clearly observed, however, due to not very reliable

laser and limited wavelength tuning experiments with this system were limited. Shortly after, experiments were carried out with a continuously tunable IR channel, which was based on picosecond OPA. The vibrational spectra of adsorbed molecular monolayers on various substrates were easily obtained [42]. Further experiments confirmed SFG spectroscopy as a tool to investigate vibrational relaxation of the adsorbed molecules [43], the phase of $\chi^{(2)}$ for adsorbed monolayer [44], neat liquid interfaces [45], and many more [5,40,41,46–48]. One of the most attractive fields at the time was the study of interfacial water spectra [49–51], since there was still very little known about the water interfaces at the molecular level.

2.1.2. Basics of sum-frequency generation spectroscopy

The SFG spectroscopy is based on a resonant nonlinear mixing of tunable infrared (ω_{IR}) and fixed/constant visible (ω_{VIS}) laser radiation, in order to produce an output with the sum-frequency ($\omega_{SFG} = \omega_{IR} + \omega_{VIS}$) [4]. Active vibrational modes of the examined molecules at the interface provide a resonant contribution to the total sum-frequency signal. The SFG signal is generated in the visible spectral range, so that it can be measured efficiently with sensitive detectors (photomultiplier tube (PMT) or charge-coupled device (CCD) camera).

To formulate the basic theory of a surface SFG, a three-layer system was proposed in the early days of nonlinear optics [29,52]. The model of the system is presented in Fig. 2.4, where two semi-infinite dielectric media I and II are connected with an atomically thin interface layer. It is assumed, that medium I is linear and medium II is nonlinear, with the dielectric constants ε_I and ε_{II} respectively. The interface has a structure different from bulk, therefore it is characterized by dielectric constant ε'. Surface and bulk are specified by the nonlinear susceptibilities $\chi_S^{(2)}$ and $\chi_B^{(2)}$ respectively. The two input beams at frequencies ω_1 and ω_2 approach the interface from the medium I, overlap in a surface and generate a sum-frequency $\omega = \omega_1 + \omega_2$. The sum-frequency appears in both reflected and transmitted direction at the angles Θ_R and Θ_T.

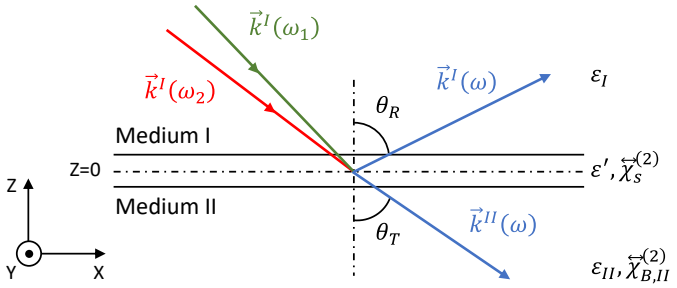

Fig. 2.4. Schematic diagram of SFG process from an interfacial system between a linear (I) and nonlinear (II) medium [53].

The transmitted and reflected SF output could be found by solving the Maxwells equation [40]:

$$\left[\nabla \times (\nabla \times) - \frac{\omega^2 \varepsilon(\omega)}{c^2}\right] \vec{E}(\omega) = \frac{\omega^2}{c^2} \vec{P}^{(2)}, \tag{2.33}$$

where nonlinear polarization $\vec{P}^{(2)}$ in bulk II is expressed by [40]:

$$\vec{P}_B^{(2)} = \overleftrightarrow{\chi}_B^{(2)} : \vec{E}_1^{II} \vec{E}_2^{II} = \overleftrightarrow{\chi}_B^{(2)} : \vec{\mathcal{E}}_1^{II} \vec{\mathcal{E}}_2^{II} e^{i[(\vec{k}_1^I + \vec{k}_2^{II}) \cdot \vec{r} - (\omega_1 + \omega_2)t]}. \tag{2.34}$$

In the thin layer of the surface the nonlinear polarization $\vec{P}_S^{(2)} \delta(z)$ is given by [40]:

$$\vec{P}_S^{(2)} = \overleftrightarrow{\chi}_S^{(2)} : \vec{E}_1^0 \vec{E}_2^0 = \overleftrightarrow{\chi}_S^{(2)} : \vec{\mathcal{E}}_1^0 \vec{\mathcal{E}}_2^0 e^{i[(\vec{k}_1^0 + \vec{k}_2^0) \cdot \vec{r} - (\omega_1 + \omega_2)t]}, \tag{2.35}$$

where the superscript 0 shows that the quantity is related to the interfacial layer at the surface ($z = 0$). The sum-frequency intensity is given by [5]:

$$\begin{aligned} I(\omega) &= \frac{c\sqrt{\varepsilon_I(\omega)} \left| \hat{e} \cdot \vec{E}^I(\omega) \right|^2}{2\pi} \\ &= \frac{8\pi^3 \omega^2 \sec^2 \theta_I}{c^3 \sqrt{\varepsilon_I(\omega) \varepsilon_I(\omega_1) \varepsilon_I(\omega_2)}} \left| \vec{e}(\omega) \cdot \overleftrightarrow{\chi}_{s,eff}^{(2)} \right. \\ &\quad \left. : \vec{e}_1(\omega_1) \hat{e}_2(\omega_2) \right|^2 I(\omega_1) I(\omega_2). \end{aligned} \tag{2.36}$$

For IR-visible SFG vibrational spectroscopy (Fig. 2.5(a)), where $\omega_1 = \omega_{VIS}$, $\omega_2 = \omega_{IR}$, $\omega = \omega_{SFG}$ with ω_{IR} near resonances, surface nonlinear susceptibilities for a continuum resonances can be expressed as [5,39]:

$$\overleftrightarrow{\chi}_{S,\,\text{eff}}^{(2)}(\omega_{IR}) = \overleftrightarrow{\chi}_{NR}^{(2)} + \int \frac{\overleftrightarrow{A}(\omega_q) \rho(\omega_q)}{\omega_{IR} - \omega_q + i\Gamma_q} d\omega_q, \tag{2.37}$$

$$\text{Im}\overleftrightarrow{\chi}_{S,\,\text{eff}}^{(2)}(\omega_{IR}) = \pi \overleftrightarrow{A}(\omega_q) \rho(\omega_q). \tag{2.38}$$

Meanwhile for discrete resonances [5]:

$$\overleftrightarrow{\chi}^{(2)}_{S,\,\mathrm{eff}}(\omega_{IR}) = \overleftrightarrow{\chi}^{(2)}_{NR} + \sum_q \frac{\overleftrightarrow{A}(\omega_q)}{\omega_{IR} - \omega_q + i\Gamma_q}, \tag{2.39}$$

$$\mathrm{Im}\overleftrightarrow{\chi}^{(2)}_{S,\,\mathrm{eff}}(\omega_{IR}) = \frac{\Gamma_q \overleftrightarrow{A}(\omega_q)}{\left(\omega_{IR} - \omega_q\right)^2 + \Gamma_q^2}. \tag{2.40}$$

Here $\overleftrightarrow{\chi}^{(2)}_{NR}(\omega_{IR})$ is the nonresonant background, $\overleftrightarrow{A}_q$, ω_q and Γ_q are, respectively, the amplitude, frequency and damping constant of the q-th resonant mode, and $\rho(\omega_q)$ is the mode density at ω_q.

Since the IR input is tunable, it is scanned over the vibrational resonances, therefore $\overleftrightarrow{\chi}^{(2)}_{S,\,\mathrm{eff}}$ is resonantly enhanced. In case the visible channel (ω_{VIS}) is tunable as well, the electronic resonances will supplement the electronic spectrum. The double resonances could be recorded by scanning both channels (ω_{IR} and ω_{VIS}) [54]. Energy level diagrams for mentioned cases are presented in Fig. 2.5(b).

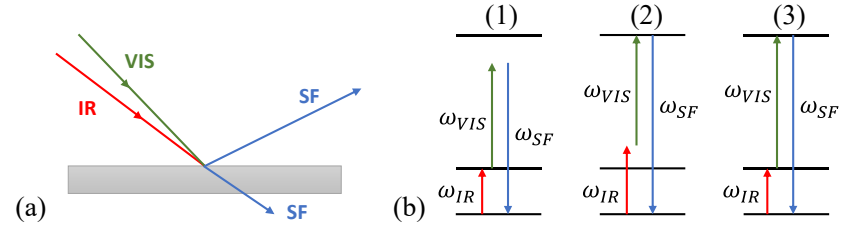

Fig. 2.5. a) Schematics of SFG process. **b)** Energy level diagrams of resonant SFG with (1) ω_{IR} on resonance, (2) $\omega_{IR} + \omega_{VIS}$ on resonance and (3) ω_{IR} and $\omega_{IR} + \omega_{VIS}$ on resonances.

2.1.3. Types of sum-frequency generation spectroscopy systems

The SFG spectroscopy systems can exploit different laser sources which can lead to some advantages and disadvantages comparing together. Nanosecond, picosecond, and femtosecond lasers can be used for experimental SFG setups. Fourier-transform-limited pulses with a longer duration allow achieving better spectral resolution, on the other hand very short pulses improve generation efficiency, signal-to-noise ratio, and data acquisition speed.

There are three types of SFG spectroscopy systems widely used for research: narrowband, broadband, and hybrid. In narrowband SFG systems, mid-IR and visible laser sources with picosecond pulse durations are used. That provides excellent spectral resolution down to few wavenumbers [6,55]. Those systems are already commercially available and extensive research has been done using them. Measurements using these systems are based on

wavelength scanning, which gives good spectral resolution and signal-to-noise ratio, however, it could be a source of systematic errors due to the sample degradation in time [6]. Narrowband SFG system requires high energy of picosecond pulses for sufficient SFG signal generation and the measurement takes a few hundred seconds, therefore they can significantly heat up the sample, and some samples are modified or completely damaged until the end of the measurement. Typically, 30 ps pulse duration radiation, IR pulses energy of 0.3 mJ (up to ~1.2 J/cm^2), and 532 nm pulses of energy from a few μJ up to 0.5 mJ (up to ~2 J/cm^2) are used in that kind of spectrometers [56,57]. Broadband SFG systems use femtosecond laser sources, that allow simultaneous recording of the complete spectrum without laser wavelength scanning and consequently speed up spectroscopic data acquisition. Due to the shorter pulse duration (higher intensity) it requires less energy compared to narrowband systems, therefore samples are less heated and possible systematic errors are eliminated. Nevertheless, spectral resolution is limited to ~10-20 cm^{-1} [6]. To overcome these limitations, spectral narrowing techniques are used to increase resolution down to ~2-4 cm^{-1} [58,59]. However, these methods are usually very ineffective and can cause significant energy losses. A slightly different solution for the increase of resolution was proposed in [60] where Ti:Sapphire oscillator seeded femtosecond and picosecond regenerative amplifiers (RA). In this case, the spectrum of ~1 ps pulses was narrowed with etalon down to the bandwidth of 0.9 cm^{-1}. This approach allowed to reach the SFG resolution down to 1.4 cm^{-1}, although due to only ~5 % transmittance of the etalon the overall efficiency of this system was very low. The nonlinear spectral narrowing technique, based on sum-frequency generation with pulses of equal wavelength but opposite chirp, has shown promising results in [61] regarding the optimization of energy losses. However, the setup of this approach is rather complex and not very simple to implement. Therefore, hybrid SFG systems with femtosecond and narrowband picosecond laser sources can be used as an alternative [62]. An improved spectral resolution of 0.6 cm^{-1} was presented using two separate picosecond and femtosecond lasers [63]. The authors indicated and demonstrated, that high spectral resolution and high signal-to-noise ratio are essential for accurate lineshape registration of the SFG vibrational response. The resonant response often contains signatures of fine molecular interactions and heterogeneity, which are in order of only a few wavenumbers [64,65]. Notwithstanding, this approach required precise electronic synchronization between the two lasers. Due to the complexity and cost systems of such design are not widely used.

2.2 Development and demonstration of optically synchronized hybrid high-resolution broadband mid-IR SFG spectrometer

Material related to this section was published in A1 and A4

The SFG spectrometer design requires to have two laser channels [46]: one narrowband in the visible spectral range, which determines the SFG system spectral resolution, and another tunable and/or broadband, covering the spectral range of molecular vibrational oscillations, i.e., middle infrared spectral range laying in 2 –20 μm. To exploit SFG spectroscopy capabilities for analyzing complex molecular surfaces and interfaces (vibrational SFG spectroscopy) SFG systems with narrowband VIS and broadband mid-IR channels are required. Current SFG systems, that can satisfy these requirements are either very ineffective due to spectral filtration or demand complex synchronization.

We aimed to develop a compact and fully functional system that is energy effective, does not require complex technologies for channel formation or synchronization, and produces optimal parameters for accurate and fast measurements of vibrational SFG spectrometry. The system concept (Fig. 2.1) was based on a multiple-channel picosecond fiber laser [66,67] which serves as a seed for narrowband (~1.5 cm^{-1}) picosecond and broadband femtosecond channels, therefore they are optically synchronized. No spectral narrowing is required for the picosecond channel as the linewidth is determined by an active medium used in the (RA).

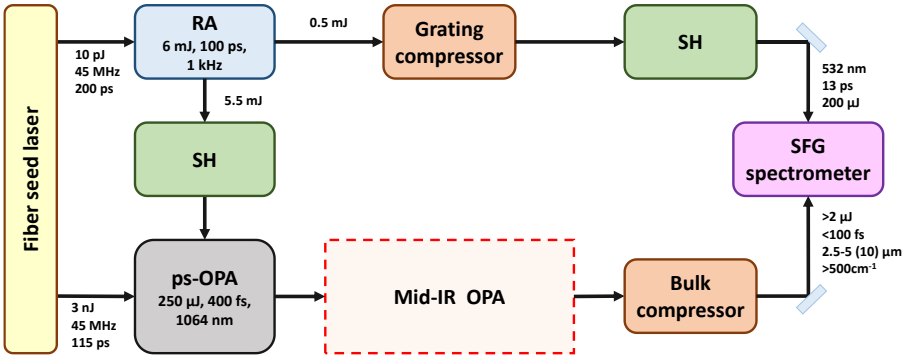

Fig. 2.1. A novel concept of broadband high resolution all optically synchronized SFG system. The abbreviations stand for: RA – regenerative amplifier, SH – second harmonic module, OPA – optical parametric amplifier module.

In order to build a hybrid fully functional SFG system, we had to find an efficient way how to convert our selected pump laser radiation into the mid-IR region, therefore, first of all, we focused our efforts on a broadband femtosecond mid-IR spectral range channel (mid-IR OPA) development and optimization. The broad-bandwidth SFG method was first presented by L. J. Richter et al. in [68] where the term "broad-band bandwidth SFG" referred to spectra obtained over a bandwidth of >200 cm^{-1}. Though it is frequently enough to cover the entire C-H stretch vibrational spectrum, our goal was to cover up to the 500 cm^{-1} range in order to be able to measure the whole SFG spectrum of O-H stretch in the water.

As there are several ways to realize the mid-IR channel scheme, we started with the modeling of different mid-IR wavelength generation and amplification layouts (Fig. 2.2), looking for the most efficient and the most broadband. The aim was to achieve widely tunable (from 2 to 10 μm) microjoule level pulses (>2 μJ) which are required for efficient SFG spectrometer operation. An optimal solution based on modeling results of the broadband mid-IR channel was experimentally realized. Spectrometer resolution and performance were tested using several common specimens in mid-IR vibrational spectroscopy.

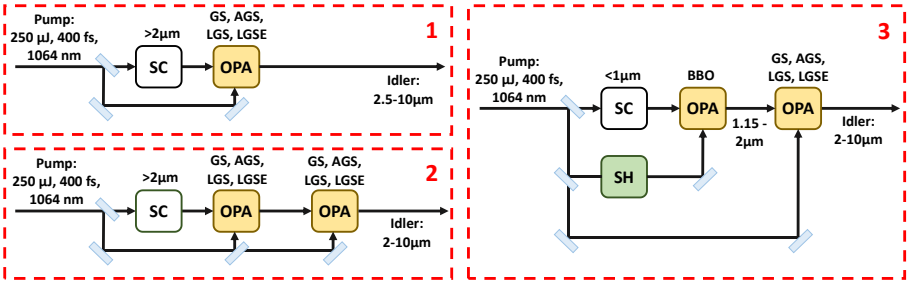

Fig. 2.2. Analyzed schemes of mid-IR OPA configurations. The abbreviations stand for: RA – regenerative amplifier, SH – second harmonic module, SC – broadband seed (supercontinuum) generator, OPA – optical parametric amplifier module.

2.2.1. Numeric simulations of broadband mid-IR stage

The simulations aimed to choose the best suiting scheme for mid-IR channel realization in the broadband high-resolution all optically synchronized SFG system. The next aspect of the task was to select optimal nonlinear crystal along with its length and amplifier parameters to achieve the desired output radiation parameters. The optical characteristics of the pump laser were chosen according to the real experimental values: 250 μJ pulse energy at

1064 nm central wavelength, 400 fs pulse duration. The whole final pump laser setup will be described later in section 2.2.2.

In order to generate widely tunable mid-IR radiation, broadband or widely tunable seed is required. One of the very common methods to produce it is via SC radiation generation. OPA stage seeded with this broadband signal produces idler wave in the desired mid-IR wavelength region [69]. We started with the same approach, however, we were restricted by the pump power and challenging desired output parameters. Nonlinear crystals suitable for broadband parametric amplification in the mid-IR wavelength range were selected for simulations: gallium selenide – GaSe (GS), silver thiogallate - $AgGaS_2$ (AGS), lithium gallium sulfide - $LiGaS_2$ (LGS), lithium gallium selenide - $LiGaSe_2$ (LGSE). Parameters of the investigated crystals at different idler wavelengths are presented in Table 2.1 where d_{eff} - effective nonlinear coefficient, Δν - FWHM phase-matching bandwidth (calculated according to equation (1.23)), LIDT – laser-induced damage threshold.

Table 2.1. List of crystals used for the OPA stage modeling and their parameters. Adapted with permission from [A1].

Nonlinear crystal	**d_{eff}, pm/V**				**Δν, cm^{-1} @1 mm length crystal**				**LIDT, MW/cm^2 (λ=1064 nm)**
	2.5 μm	5 μm	7.5 μm	10 μm	2.5 μm	5 μm	7.5 μm	10 μm	
GS	55.3	57.2	58.4	59	981	243	189	176	30 @10 ns [70]
AGS	13	11.3	10.2	9.64	826	205	172	336	10 @20 ns [71] 34 @15 ns [72]
LGS (xz plane)	-3.98	-4.38	-4.49	-4.4	957	339	4284	99	>240 @14 ns [72]
LGSE (xz plane)	-6.1	7.16	-7.6	-7.8	700	221	191	668	80 @5.6 ns [72]

Our model [73,74] was based on three-wave resonant interaction equations. We used a full 3D grid in time and lateral dimensions of the beam (x and y), meanwhile z being the propagation direction. We were able to define beam parameters (wavelength, bandwidth, diameter, ellipticity, shape), pulse duration, shape, and dispersion. In multiple OPA stages case, the output of the previous stage was used as input for the next stage.

To determine whether a single or multiple OPA stage is optimal, simulations with 1 nJ and 1 μJ seed energies were performed for a set of nonlinear crystals. The pump intensities were chosen according to the LIDT values for different crystals. The beam diameters for seed and pump were 1.5 mm and 1 mm (at $1/e^2$ level) respectively. The simulation strategy was to optimize the crystal length so that the bandwidth of the amplified idler wave

would be larger than 500 cm^{-1} at the 30% level of maximum (sufficient level for reliable SFG spectrum measurement which was determined experimentally), along with the best conversion efficiency. Simulation results for both seeds energies 1 nJ and 1 µJ are presented in Table 2.2 for comparison. Results received using 1 µJ seed energy manifested, that it is a required minimum to achieve desired conversion efficiencies in the second nonlinear amplification stage.

Table 2.2. Comparison of the OPA stage pump conversion efficiencies to the idler wave for different nonlinear crystals at 4 µm and 2.5 µm idler wavelength with the 1 nJ and 1 µJ seed energy. Adapted with permission from [A1].

Seed energy, nJ	Idler, µm	Conversion efficiency, %				
		GS	AGS		LGS	LGSE
		*50 GW/cm^2	*50 GW/cm^2	*100 GW/cm^2	*100 GW/cm^2	*100 GW/cm^2
1	2.5	1.66E-01	2.56E-03	6.22E-03	3.71E-03	1.35E-03
	4	4.47E-02	1.60E-04	3.00E-04	5.50E-04	1.90E-04
1000	2.5	1.40E+00	1.94E+00	2.99E+00	2.48E+00	1.17E+00
	4	2.28E+00	1.51E-01	2.78E-01	4.82E-01	1.82E-01

* Pump peak power used for simulations.

Despite that GS crystal performance was the best at the low seed case, it has some major drawbacks as well. One cannot cut it at any desired angle, and only the z-cut option is possible. This issue results in the need for a large aperture crystal due to the high phase-matching angle (angle of incidence at air-crystal interface ~40-80 deg) for the 1064 nm pump. Another important drawback is that no AR coating can be applied for this crystal due to its extremely low Mohs hardness. As a result, the above-mentioned issues and a quite large phase-matching angle in the crystal lead to tremendous reflection losses. For the cases s(o) + i(e) = p(e) and s(e) + i(o) = p(e) interactions losses approach to 100% and for the s(o) + i(o) = p(e) case losses exceed 80% at 2.5 µm and 30% at 10 µm wavelengths (Fig. 2.3). Therefore, only the last case was analyzed. Here we used the following notations; s-signal; i-idler; p-pump; o-ordinary wave; e-extraordinary wave.

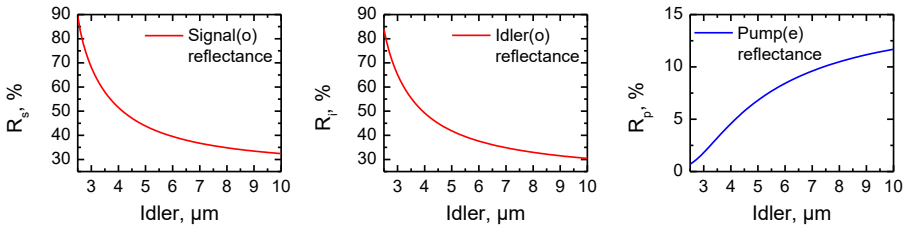

Fig. 2.3. Calculated reflection losses in GS crystal from a single surface (s(o) + i(o) = p(e) interaction) for idler, signal, and the pump signal for different idler wavelengths.

To understand the tendency of conversion efficiency dependence on seed pulse energy, simulations at various signal energy levels from 1 nJ to 20 µJ were performed for AGS crystal at 2.5 µm idler wavelength. A crystal length of 0.36 mm, the seed beam diameter of 1.5 mm (at $1/e^2$ level), pump pulse duration of 400 fs, the pump beam diameter of 1 mm (at $1/e^2$ level), and pump intensity of 100 GW/cm^2 were used in simulations. Two signal pulse duration cases - transform-limited pulses of 29 fs duration and chirped with 1400 fs^2 additional dispersion to 206 fs duration, were compared (Fig. 2.4(a)). The efficiency of conversion increased rapidly when the signal energy was increased from 1 nJ to a few µJ, but saturated at higher seed pulse energies. The saturation level can be increased by applying additional dispersion to the signal pulse. As presented in Fig. 2.4(a) case, an increase of duration by ~7 times lead to an increase of the saturation level by ~ 2.5 times.

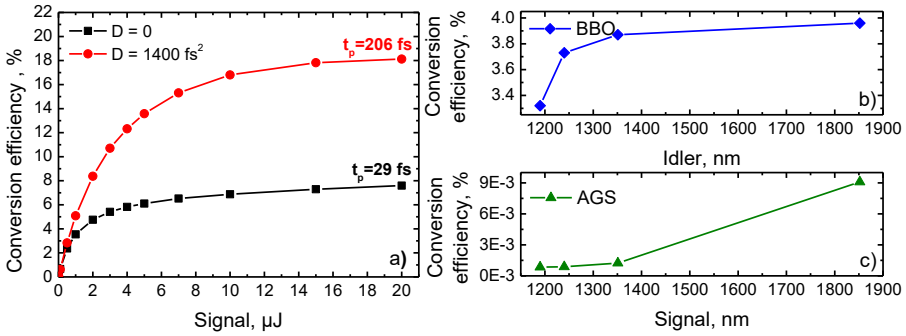

Fig. 2.4. a) Conversion efficiency dependence on the seed energy level of the AGS OPA stage at 2.5 µm idler wavelength. **b)** Conversion efficiency for different idler wavelengths of the BBO OPA stage. **c)** Conversion efficiency for the different seed wavelengths of the AGS OPA stage. Adapted with permission from [A1].

Since the SC energy is at a level of few nJ and additional dispersion influence is noticeable only at energy levels of >0.5 µJ, the best-expected conversion efficiency of the first OPA stage could be ~0.16% at 2.5 µm and ~0.045% at 4 µm only. In the case of two nonlinear amplification stages, pump energy has to be distributed between stages. As the pump laser energy is limited, the first stage efficiency is too low to achieve 1 µJ output energy even under the full pump. Without sufficient seed energy, the second OPA stage will be inefficient, therefore a more effective first stage is required.

As an alternative to the 1064 nm pumped first OPA stage, the SH pumped BBO OPA was analyzed theoretically as well. The BBO crystal has good transmission in the 1190-1850 nm spectral range, as possesses a large nonlinear coefficient, broad amplification bandwidth, and finally, significantly higher LIDT [75,76] than all infrared crystals of interest. A

similar scheme was implemented by M. Bradler et al. in [77] as the first stage in $LiNbO_3$-based broadband mid-IR OPA.

In the model, the first BBO OPA stage was seeded with the same 1 nJ seed energy pulse, with the wavelength in the spectral range from 746 nm to 962 nm. Corresponding idler wavelengths were tuned from 1.19 μm to 1.85 μm. BBO crystal has a higher damage threshold, therefore 200 GW/cm^2 pump intensity was set. The optimized crystal length was set to 2 mm. The final results of the simulation are presented in Fig. 2.4(b). Conversion efficiency was calculated relatively to the 1064 nm pump pulse energy, therefore 66% SH generation efficiency was taken into account. For comparison of schemes, simulations using AGS crystal were performed in the same wavelength range (Fig. 2.4(c)). In that case, the SC wavelengths from 1.19 μm to 1.85 μm were amplified. Pump intensity was set to 100 GW/cm^2 and the crystal length was set to 0.36 mm, which ensured broadband amplification. The results manifested, that conversion efficiency to the idler in the BBO crystal OPA is nearly 3 orders of magnitude higher comparing to conversion efficiency to the signal in the AGS crystal. Higher conversion efficiency in the BBO crystal OPA allows to increase the efficiency of the second OPA stage and achieve ~1 μJ energy seed pulses using only the fraction of the pump laser pulse energy.

A slightly non-collinear configuration for BBO OPA is more suitable due to the easier seed and idler beams separation. The drawback of the non-collinear configuration is the angular dispersion of the idler wave, as it is used as a seed for the subsequent OPA stage. In order to avoid the angular dispersion, we decided to use the red side of the SC radiation as a seed instead of the blue side, in this way whole angular dispersion was transferred to the VIS-NIR spectrum [78]. Simulations of this configuration manifested comparable conversion efficiencies. The angle between the pump and signal has to be minimized to the practical limit required for beams separation as well as optimal crystal length has to be selected in order to maintain a broad spectrum since there is no magic-angle for this configuration.

The final setup of mid-IR OPA is presented in Fig. 2.5. To get more realistic simulation results, the first OPA stage amplification was remodeled with higher input energy - 5 nJ seed instead of 1 nJ, which was evaluated using experimentally measured SC power. Optimization of seed and pump beam diameters along with temporal overlap of the pump and seed pulses were performed. The pump and seed beam diameters of 330 μm and 500 μm (at 1/e^2 level) respectively were used for the final simulations. Calculated conversion efficiencies of the 1064 nm pump pulse energy to idler pulses

(including SH generation losses) reached 4.5-5.4% for NIR wavelengths in the 1852-1190 nm spectral range respectively. Radiation with parameters achieved after the first OPA stage was used as the input signal to the second OPA stage. The pump pulse energy was split to 10 µJ reserved for SC generation, 60 µJ for the first OPA stage, and the rest of the pump energy for the second stage. The calculated signal energy after the first stage was 2.7-3.27 µJ in the 1852-1190 nm spectral range. The simulations and optimization of the second stage OPA were performed for several nonlinear crystals. The seed beam diameter of 1.1 mm (at $1/e^2$ level), pump pulse duration of 400 fs, the pump beam diameter of 1 mm (at $1/e^2$ level), and pump intensity of 100 GW/cm^2 were used. During simulations, the optimization of crystal length, the delay between pump and seed, and seed dispersion was performed. The best results for several crystals are presented in Fig. 2.6. For the modeled crystals the lowest conversion in the second OPA stage was 0.6-2% in the longer wavelength range, which increased up to 2.7-5.5% at the shorter wavelength side. Calculated idler energy after the second stage reached 1-3.4 µJ at 10 µm wavelength and up to 4.5-9.3 µJ at 2.5 µm idler wavelength. The idler pulse bandwidth at the 30% level of maximum was broader than 500 cm^{-1} over almost full mid-IR tuning range, for all investigated nonlinear crystals. Though intuitively it looks that direct conversion of IR pump pulses to the mid-IR spectral range can be more efficient, modeling revealed, that generation of seed using visible light pumped OPA and subsequent mid-IR radiation amplification using IR pump is much more efficient. The reason for this is in the superior efficiency of the BBO crystal-based OPA stage produced a high-energy seed for the mid-IR nonlinear conversion stage. The modeling allowed selection of the layout which enabled the generation of enough mid-IR energy for building an SFG spectrometer.

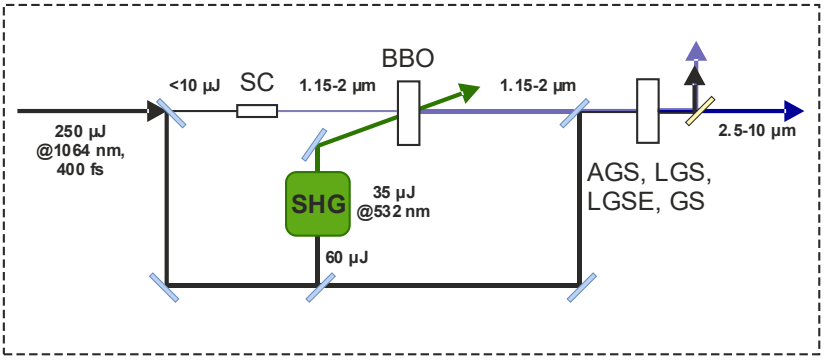

Fig. 2.5. Final setup of the analyzed two-stage mid-IR OPA. Adapted with permission from [A1].

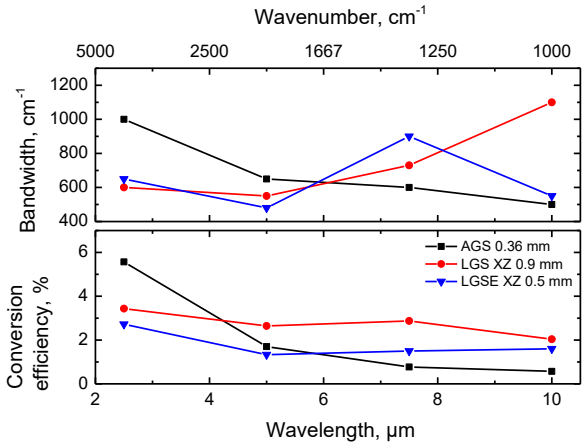

Fig. 2.6. Comparison of mid-IR OPA stage pump conversion efficiencies to idler and idler bandwidth at the 30% level with different nonlinear crystals for 2.5-10 μm idler wavelength. Adapted with permission from [A1].

2.2.2. Experimental realization and characterization of mid-IR SFG spectrometer

Simulation results were taken as a guideline for building the experimental setup, therefore, two-stage OPA for mid-IR radiation amplification was implemented in the SFG spectrometer scheme.

The final setup of the SFG spectrometer is presented in Fig. 2.7. Our hybrid approach of the system front-end part is described in detail in [67]. All-in-fiber 45 MHz repetition rate SESAM mode-locked oscillator operating at 1064 nm wavelength had 3 optically synchronized outputs. One of them was used to seed a picosecond Nd:YVO_4 RA, meanwhile another one was a fusion spliced to fiber pigtailed InGaAs photodetector, from which the RA controls were synchronized. The 1064 nm wavelength pulses in RA were amplified up to 6.1 mJ at a 1 kHz repetition rate, of which 0.1 mJ was used as narrowband SFG channel seed and 6 mJ as a broadband channel pump. The pump pulse duration after RA was 100 ps. The third output provided seed to the Yb-doped fiber amplifier and pulse stretcher module. After the amplification up to a few nJ energy level, the pulse spectrum was broadened up to 14 nm via self-phase modulation in single-mode fiber and then pulses were temporally stretched up to 115 ps using a chirped fiber Bragg grating. These broadband pulses subsequently were amplified in the picosecond BBO OPA.

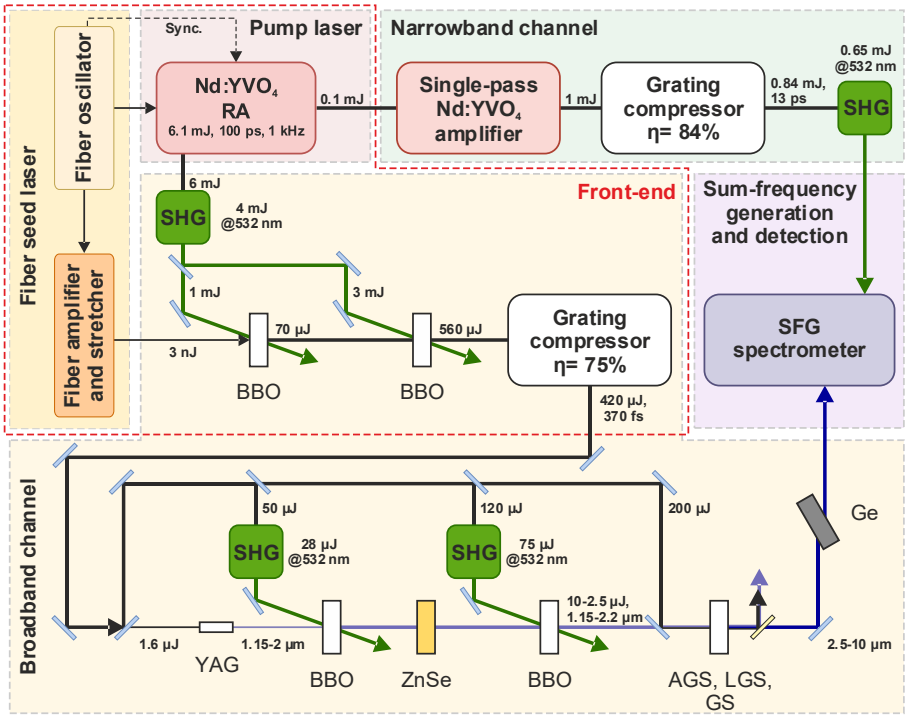

Fig. 2.7. The layout of the assembled optically synchronized SFG spectrometer setup. Adapted with permission from [A1].

Broadband SFG spectrometer channel

Temporally and spectrally stretched broadband 1064 nm wavelength pulses were coupled out of the fiber via free-space collimator and amplified in two picosecond OPA stages up to 560 µJ. The output of Nd:YVO_4 RA (beam diameter of 2 mm (at $1/e^2$ level)) was frequency-doubled in 9 mm LBO crystal with ~67% conversion efficiency and was used as a pump of the ps BBO OPA in the broadband channel front-end. Type I phase-matched BBO crystals of 9 mm and 4 mm length were used for the first and second ps OPA stage respectively. The pump and seed beam diameters of 0.65 mm and 1 mm for the first stage and 1.4 mm and 1.8 mm for the second stage (at $1/e^2$ level) were used. The ratio of the pump energy for each stage was optimized in a way to achieve the best overall conversion efficiency with minimal spatial beam distortions. The optimal pump energy distribution ratio in our system was 1 mJ for the first stage and 3 mJ for the second one what resulted in an overall pump to signal conversion efficiency of 14%.

After the cascade of ps OPA's, amplified broadband pulses were compressed by the transmission diffraction grating compressor using 1600 groves/mm gratings operating at Littrow configuration. The

autocorrelation trace of the compressed pulse was measured by the SHG autocorrelator (APE pulseCheck) (Fig. 2.8(a)). The measured pulse duration was equal to 367 fs according to the Gaussian fit with the contrast of ~96-97%. The efficiency of the compressor was equal to 75%, which resulted in the final pulse energy at the output of the broadband front-end around 420 μJ.

A small fraction of the compressed femtosecond pulse was focused into the 20 mm length yttrium aluminum garnet (YAG) crystal by the lens with a focal length of 75 mm (into a focal spot of ~70 μm (at $1/e^2$ level)) in order to generate the SC radiation. Focusing conditions and pump energy (~1.6 μJ) were optimized to produce smooth, stable, and sufficiently broad, especially in the longer wavelengths SC wing (>2 μm), spectrum (Fig. 2.8(b)).

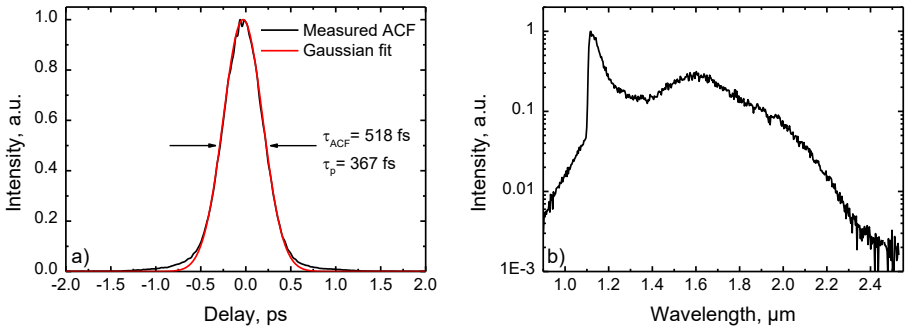

Fig. 2.8. a) The measured autocorrelation trace of the compressed femtosecond front-end output pulses (black) and Gaussian fit (red). **b)** The spectrum of supercontinuum produced in a 20 mm YAG crystal. The pump radiation was filtered using the long-pass filter (1100 nm). Adapted with permission from [A1].

The remainder was used as a pump for the femtosecond noncollinear OPA (fs NOPA). The pump pulse was split into three parts. The first two of 50 μJ and 120 μJ pulse energies (beam diameter of 1.9 mm (at $1/e^2$ level)) were frequency-doubled in 1.5 mm BBO crystals with conversion efficiencies of 56% and 63% respectively and then used as a pump for two stages of fs NOPA where 1150-2200 nm band of supercontinuum was amplified. The pump and seed beam diameters of 0.4 mm and 0.48 mm for the first stage and 0.6 mm and 0.8 mm for the second stage (at $1/e^2$ level) were used. Noncollinear geometry configuration allowed us to separate idler wave without using broadband dichroic mirrors. The Poynting-vector walk-off compensation (PVWC) geometry was used in both stages instead of tangential phase-matching (TPM) to reduce parasitic signals. Schematic representation of both geometries is presented in Fig. 2.9. For example, the BBO phase-matching angle for SH generation from 1350 nm wave is ~20.4°, which is very close to the phase-matching angle (θ_{pm}) of the fs NOPA (~20.66°) pumped by 532 nm

at ~2.5° noncollinearity angle (α), meanwhile, in PVWC geometry this angle differs much more being around 25.66°. Due to the similar phase-matching angles of the SH and NOPA process, the larger part of the signal energy was converted to SH as well as to other wavelengths via four-wave mixing at TPM geometry (Fig. 2.10). To enhance the signal and pump temporal overlap ratio and achieve better conversion efficiencies, the dispersion of signal pulses was controlled using a plate of ZnSe placed between the stages. By tuning the phase-matching angles of BBO crystals and the delay between signal and pump, the SC radiation was amplified up to ~10 μJ at 1150 nm wavelength and up to ~2.5 μJ at 2200 nm (Fig. 2.11).

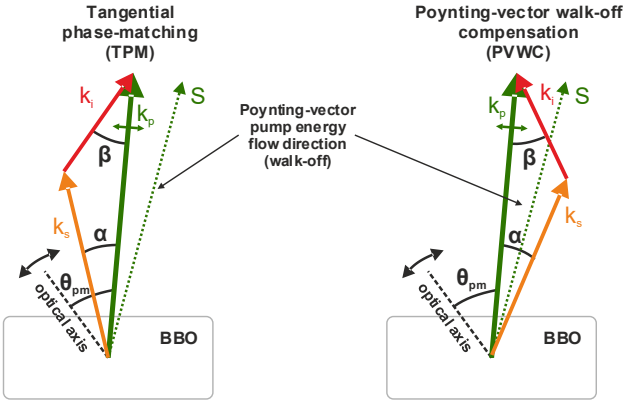

Fig. 2.9. Schematics of tangential phase-matching (TPM) (left) and Poynting-vector (S) walk-off compensation (PVWC) (right).

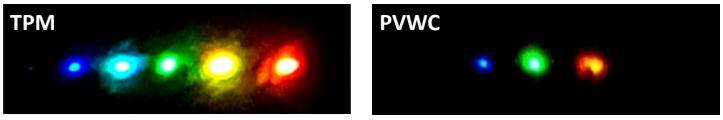

Fig. 2.10. Illustration of multiparametric interactions in the OPA output beams on a white screen after the BBO crystal at TPM and PVWC amplification geometries. Adapted with permission from [A1].

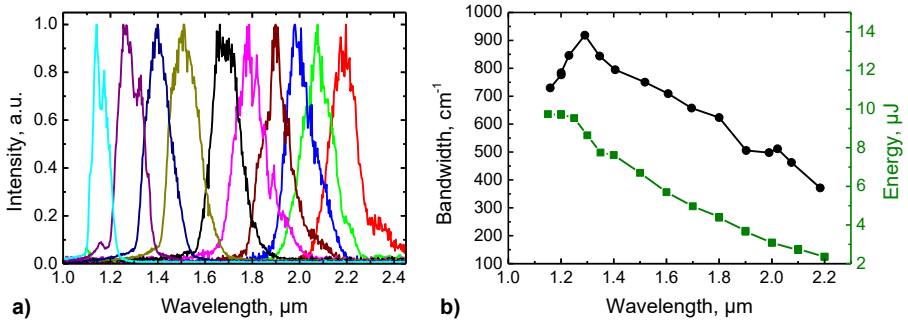

Fig. 2.11. The fs NOPA output spectra **(a)**, spectral bandwidth at a 30% level of maximum and the pulse energy **(b)**. Adapted with permission from [A1].

The last part of the remaining pump (~200 µJ) radiation at 1064 nm wavelength was directed to the mid-IR fs OPA stage collinearly with the broadband signal amplified in fs NOPA. Signal radiation in the 1.15-2.2 µm wavelength range was used to generate 2-13 µm idler waves in AGS, LGS, and GS crystals. Ag coated flat and spherical mirrors were used to guide and shape the signal beam, therefore, around 30% signal energy was lost in the optical path to the last mid-IR fs OPA stage. The beam diameters for signal and pump were 1.8 mm and 1.5 mm (at $1/e^2$ level) respectively. A comparison of the results achieved with different crystals in mid-IR fs OPA is presented in Fig. 2.12. Pulse spectra were characterized using a scanning monochromator and HgCdTe (MCT) detector. We were able to measure up to 13 µm of idler wavelength after mid-IR fs OPA using 0.5 mm length GS crystal, however, tuning range was limited to ~5 µm due to large phase-matching angles and limited aperture of used crystal. The energy of the idler wave decreased from ~0.5 µJ at 5 µm down to ~0.1 µJ at 13 µm, meanwhile, the spectral bandwidth changed from ~222 cm^{-1} down to ~120 cm^{-1} respectively. The highest idler wave energy of 0.4-1.8 µJ in the 2-5 µm spectral range was achieved with the AGS crystal of 0.4 mm length. However, at longer wavelengths (5-10.5 µm) it produced considerably lower energies of 0.1-0.25 µJ. The broadest spectra were achieved with the LGS crystal of 1 mm length. The tuning range of the idler wave using this crystal was 2-9.6 µm, pulse energies of 0.1-1.35 µJ, and bandwidths of 205-550 cm^{-1} (Fig. 2.13).

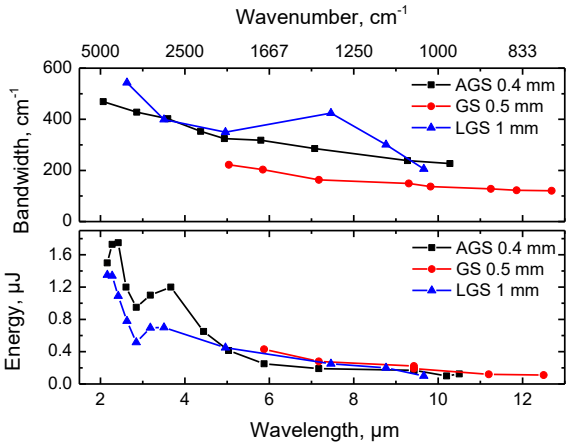

Fig. 2.12. The comparison of AGS, LGS, and GS mid-IR fs OPA idler wave parameters; the output spectral bandwidth at a 30% level of maximum and pulse energies in the wavelength tuning range. Adapted with permission from [A1].

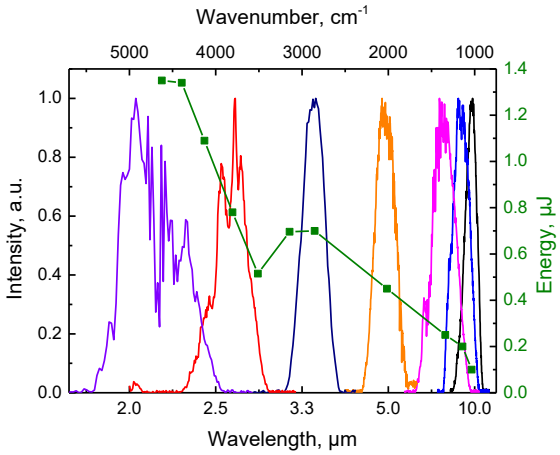

Fig. 2.13. The LGS mid-IR fs OPA idler wave output spectra and pulse energies in the wavelength tuning range of 2-9.6 µm. Adapted with permission from [A1].

Experimental conversion efficiencies differed from the simulated ones. It could be due to a few reasons. One of them was the difference in the pump intensity. We used the ~100 GW/cm^2 value in the simulations, however, during the check of the experimental setup we noticed some light-induced modifications of the AGS crystal, therefore the pump intensity was reduced down to ~60 GW/cm^2. Other reasons were the two-photon absorption and reflection losses. AGS and LGS crystals had reflection losses of ~5-10%, meanwhile GS ~30-35%. Moreover, AGS and GS crystals manifested the transmission dependency on the pump intensity as follows: at ~60 GW/cm^2 total transmission of the pump in the AGS crystal decreased down to ~85% and for the GS crystal down to 50%. No decrease in transmission was observed in the LGS crystal only. The third reason might have been due to a different beam quality and profile used in simulation and experimental setup. The pump beam in the experimental setup was not perfectly Gaussian. Finally, the Sellmeier equations used in simulations might have been inaccurate for the experimentally used crystals.

To increase idler energy, a 1 mm length AGS crystal was tested. With this crystal, the measured idler energy was from 2 to 4 times higher in 2-5 µm wavelength range (2.4-5.1 µJ) and nearly 2 times higher in 5-10 µm range (0.2-1 µJ). Although the higher energy was reached with the longer crystal, the spectral bandwidth of the pulses was inevitably narrower - 200-300 cm^{-1} over the tuning range. To increase the bandwidth of the measurement spectrum, a fast crystal scanning method was tested in the SFG spectrometer setup. For this purpose, the AGS crystal was mounted on a motorized rotating

stage and scanned around the set wavelength position in a range of a few degrees. Since the signal bandwidth was quite broad, the crystal angle scanning ensured phase-matching for a whole spectrum. By integrating the SFG signal of many idler pulses over the whole scanning range broad effective spectrum was registered. Due to signal to pump durations ratio, not all of the signal wavelengths were amplified even by applying scanning technique, which caused that the measured idler bandwidth was narrower than the bandwidth of the seed. A comparison of idler wave spectral bandwidths achieved with static AGS crystal of 0.4 mm length and static as well as scanned 1 mm length AGS crystal is presented in Fig. 2.14. In the wavelength range of 5-10 µm, the bandwidth of the idler wave amplified by the scanned AGS crystal of 1 mm length was similar or even slightly broader comparing with the 0.4 mm length crystal case, and at 2.5-5 µm spectral bandwidths were up to 500-750 cm^{-1}.

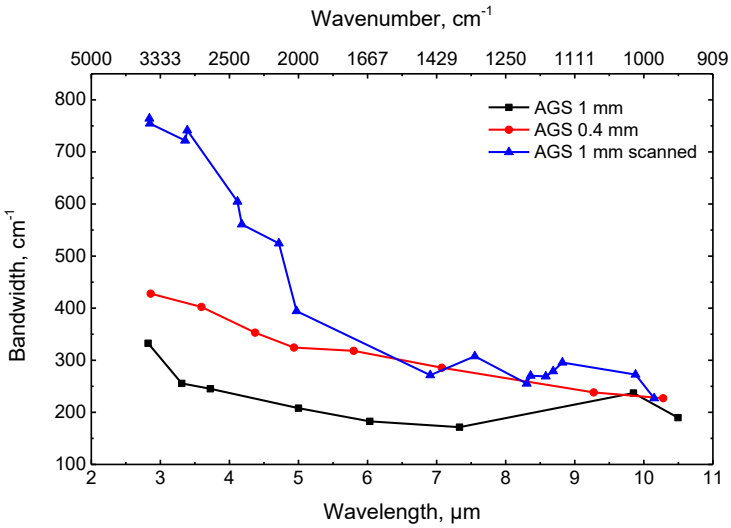

Fig. 2.14. Comparison of the idler pulse bandwidths at a 30% level of maximum for the static case using the AGS crystal of 0.4 mm length and static as well as scanned cases using 1 mm length AGS crystal over the tuning range. Adapted with permission from [A1].

After amplification, the mid-IR fs OPA idler wave was compressed using a germanium plate of experimentally selected thickness and directed to the SFG spectrometer.

Narrowband SFG spectrometer channel

A small part of chirped 100 ps pulses from the regenerative amplifier (100 µJ) was amplified in an Nd:YVO_4 single-pass amplifier up to 1 mJ energy. The

spectrum of amplified narrowband pulses is presented in Fig. 2.15(a). Then the pulses were compressed down to nearly Fourier-transform-limited (FTL) duration ~12 ps with an efficiency of 84% by using the reflection diffraction gratings compressor where 1818 groves/mm gratings were used. The measured autocorrelation trace of the compressed pulse is presented in Fig. 2.15(b). Finally, pulses of ~1.5 cm^{-1} bandwidth were frequency-doubled with 77% conversion efficiency in 6.5 mm length LBO crystal, resulting in 650 µJ pulse energy radiation at 532 nm. The narrowband visible radiation was directed to the SFG spectrometer.

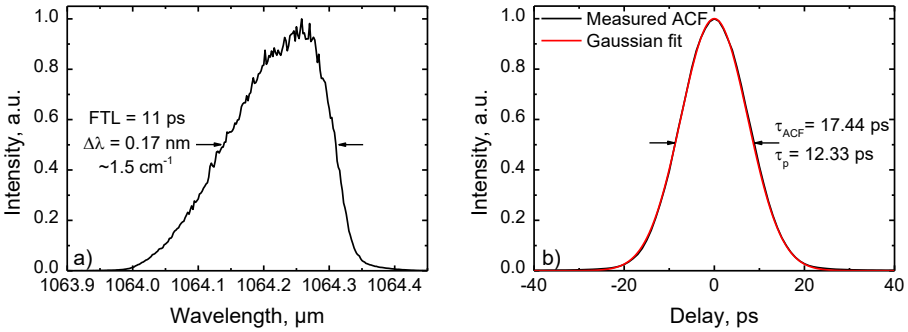

Fig. 2.15. a) The measured spectrum of the amplified narrowband pulses. **b)** The measured autocorrelation trace of the compressed narrowband channel pulses (black) and Gaussian fit (red).

2.2.3. Demonstration of fully functional SFG spectrometer system and sum-frequency generation and detection

The narrowband VIS and the broadband mid-IR pulses were combined on the sample in the SFG spectrometer, a simplified drawing of which is presented in Fig. 2.16. The SFG spectrometer setup used in the experiments was similar to the one available commercially at Ekspla. Mid-IR and VIS beams were arranged in a vertical plane that allows performing measurements of liquid samples as well as at the liquid-air interface. Narrowband channel radiation was focused by a 500 mm focal length lens positioning the beam waist on the sample with the spot diameter of 0.3 mm (at $1/e^2$ level) at the 60° angle of incidence. For the broadband channel radiation parabolic off-axis mirror of 100 mm focal length and 45° off-axis angle was used to avoid pulse broadening by dispersion of traditional transmission optical elements.

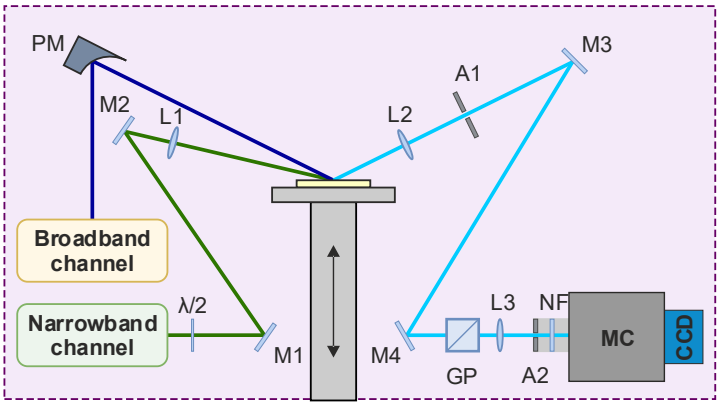

Fig. 2.16. The setup of SFG spectrometer. The abbreviations stand for: PM – parabolic mirror, M1-4 – mirror, L1-4 – lens, A1-2 – aperture, GP – Glan prism, NF – notch filter, MC – monochromator, CCD – charge-coupled device camera. Adapted with permission from [A1].

VIS and mid-IR beam overlap on a sample was adjusted by changing the sample holder height and by adjusting the parabolic mirror. The sample holder had a shift, tilt, and height adjustment. It was possible to change the states of polarization of both VIS and IR beams. The generated sum-frequency signal was collimated by fused silica lens then spatially filtered from scattered and reflected VIS radiation (L2 and A1). After that beam passed through a polarization analyzing Glan prism, it was focused into a monochromator slit. Additional aperture A2 was used to reduce background and scattered radiation and a notch filter to suppress residual VIS radiation. SFG spectrum was registered by the cooled CCD camera. We used Andor Newton 971 EM CCD camera with 1600x400 pixel sensor cooled down to -80˚C and 328 mm Andor Kymera 328i monochromator with 1200 groves/mm density grating.

For SFG spectrometer characterization several test samples were investigated. The measured spectrum of monoolein ($C_{21}H_{40}O_4$) is presented in Fig. 2.17. A narrow dip in the SFG resonance of monoolein C=O stretching vibration at 1738 cm^{-1} is the result of absorption of water vapor in the air which features a narrow line width. This graph is indicative for the evaluation of the resolution of the created spectrometer. The SFG spectrometer setup efficiently exploited the narrowband VIS beam to reach a spectral resolution down to <3 cm^{-1}. At the same time, the measurement spectral range covered by tuning of mid-IR fs OPA span stretches from 4000 cm^{-1} to 950 cm^{-1}.

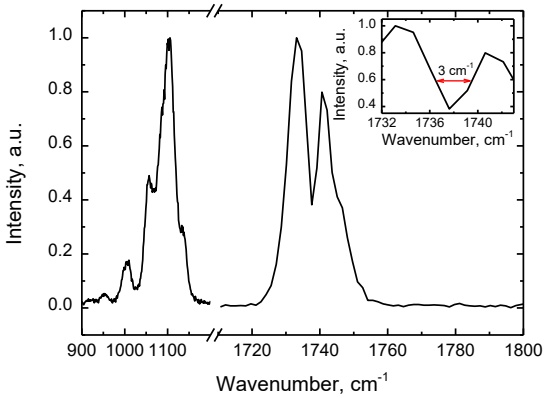

Fig. 2.17. Illustration of the SFG spectrometer resolution and the single measurement spectral range (SFG spectrum of monoolein). Inset: magnified spectrum around the dip in 1740 cm^{-1} line. Adapted with permission from [A1].

The presented SFG spectrometer allowed to perform almost real-time spectra measurement of the air/liquid interface of liquid samples such as ethanol/air interface, which illustrates quite good sensitivity. An exposure time of only 0.1 s was enough to observe the spectrum with a quite good signal-to-noise ratio (Fig. 2.18). Widely used for calibration of SFG spectrometers z-cut quartz generated sum-frequency so efficiently, that the signal was visible by the naked eye on a white screen.

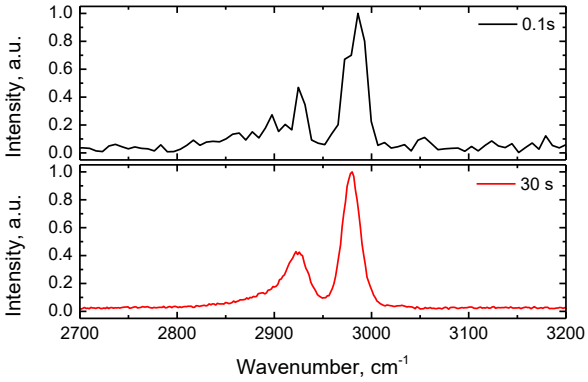

Fig. 2.18. The obtained SFG spectrum of the ethanol/air interface at different exposure times (0.1 s and 30 s). Adapted with permission from [A1].

To evaluate the bandwidth of the mid-IR channel, the gold/air interface was selected. Due to the non-resonant SFG signal, it corresponds to the laser pulse spectrum. The bandwidth of a broadband mid-IR channel allowed us to record up to 300 cm^{-1} spectral range at a single measurement (Fig. 2.19). Applying the crystal scanning technique (extended bandwidth in Fig. 2.19)

mentioned before, we were able to increase the spectral range up to more than 850 cm^{-1}. The crystal angular positions were scanned in less than a second, while measurement of SFG spectrum can take tens of seconds or even tens of minutes. Thus, the scanning technique has a minor effect on the SFG spectrum measurement. Moreover, it even makes spectrum normalization easier thanks to a broader spectral range of signal acquisition and smoothening of the mid-IR radiation spectrum.

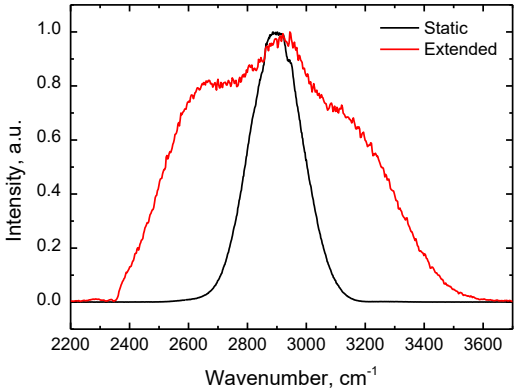

Fig. 2.19. The experimentally measured SFG spectrum of the gold/air interface using the static and the scanning method of acquisition. Adapted with permission from [A1].

2.2.4. Summary of the results

We have designed a hybrid SFG spectrometer featuring a tunable from 2 to 10 µm mid-IR channel with nearly 500 cm^{-1} bandwidth of simultaneous spectral data acquisition while assuring less than 3 cm^{-1} spectral resolution. For this system realization, we assembled a two-channel laser system that generated optically synchronized narrowband (~1.5 cm^{-1}) visible and broadband mid-IR pulses. Before mid-IR channel construction, the detailed energy conversion efficiency to mid-IR in line with the generation of femtosecond pulses of as broad as possible spectral width was modeled.

Three layouts of mid-IR OPA were analyzed. The modeling revealed that the mid-IR OPA stage pumped by 1064 nm femtosecond pulses and seeded by 1 nJ of SC radiation in 1190 nm-1850 nm wavelength range is very ineffective manifesting conversion efficiencies lower than 0.001%, using the available on the market nonlinear crystals. The exception was the GaSe crystal. The modeling showed that GaSe crystal in comparison to the rest of the tested crystals has about 100 times higher efficiency, but is still too low for the realization of SFG spectrometer. It was found, that to achieve acceptable output energies the input signal energy in this kind of OPA should

be of a microjoule-level. Following the modeling results, a two-stage mid-IR OPA scheme was chosen. Modeling manifested unsatisfying output parameters due to the low efficiency of the first mid-IR OPA stage. The alternative approach exploiting the signal wave of BBO OPA seeded with a long-wavelength wing (1150 nm-1850 nm) of SC radiation and pumped by the second harmonic of pump laser at 532 nm presented acceptable performance of energetic seed generation. This approach demonstrated conversion efficiencies from ~0.6 to ~5.5% and several μJ levels of pulse energies amplified in mid-IR OPA, which is 2-3 orders of magnitude higher than produced by mid-IR OPA layouts pumped by fundamental 1064 nm radiation by the same pump energy. In this case, as modeled, the idler pulse energy after the second stage reaches 1-3.4 μJ at 5-10 μm idler wavelength and 4.5-9.3 μJ at 2.5 μm idler wavelength with bandwidth broader than 500 cm^{-1}, which fulfills requirements for the broadband SFG system realization.

Based on the simulation results experimental setup of the SFG spectrometer system was designed, assembled, and examined. The 0.4 mm length AGS, 0.5 mm length GS and 1 mm length LGS crystals were tested for the mid-IR fs OPA stage. We were able to achieve tunability from 5 μm up to 13 μm of the idler wavelength using the GS crystal and from 2 μm up to 10 μm using the AGS and the LGS crystals. Energies up to 0.4-1.8 μJ of idler wave at 2-5 μm wavelengths were achieved using the AGS crystal and 0.2-0.5 μJ at 5-10 μm wavelengths using the LGS and the GS crystals. The broadest bandwidth over the tuning range of 205-550 cm^{-1} was achieved using the LGS crystal, and 230-470 cm^{-1} using the AGS crystal. The experimental results differed from the simulated ones probably due to such factors as two-photon absorption in AGS and GS crystals, lower pump intensity, and reflection losses that were not taken into account in the calculations.

In order to increase the idler energy use of 1 mm length, AGS crystal with angular scanning was analyzed. The increase in the mid-IR energy was from 2 to 4 times in 2-5 μm wavelength range (up to 2.4-5.1 μJ) and ~2 times in 5-10 μm range (up to 0.2-1 μJ), meanwhile, the bandwidth in 5-10 μm spectral range was similar to the case of 0.4 mm length AGS crystal - around 250-350 cm^{-1} while in 2-5 μm wavelength range broader effective spectra of around 500-750 cm^{-1} were achieved.

A fully functional SFG system was tested. The spectral resolution of <3 cm^{-1} and spectral range of measurement stretching from 4000 cm^{-1} to 950 cm^{-1} were achieved. The energy of mid-IR pulses was sufficient to perform real-time measurements of various liquid and solid samples. As an

example, at the 0.1 s exposure time ethanol spectrum was obtained with an acceptable signal-to-noise ratio. The crystal scanning technique allowed achieving more than 850 cm^{-1} bandwidth at 2900 cm^{-1}, having a minor influence on spectra acquisition time.

CHAPTER 3

REPETITION RATE LOCKING OF FIBER OSCILLATOR FOR Ti:SAPPHIRE BASED BROADBAND SFG SPECTROSCOPIC SYSTEMS

This chapter is dedicated to the repetition rate synchronization and locking of ultrafast mode-locked fiber oscillators with the goal to apply those in broadband SFG spectroscopic systems. The aim is to create a ps narrowband seed source for Nd ion-based regenerative or linear amplifier precisely synchronized with Ti:Sapphire femtosecond laser pumped mid-IR tunable source. This approach can be a valuable practical improvement for widely used SFG spectrometer setups allowing straightforward synchronization of narrowband and broadband channels producing lasers and paves a way to enhance the spectral resolution.

First of all, the most common types of mode-locked oscillators are described in the literature review section. Then, an overview of technologies that allow to actively control repetition rate and lock the oscillator to another laser or electrical clock is presented. Furthermore, the measurement methods for oscillator phase noise and jitter are also reviewed.

The demonstration of a synchronized ultrafast Yb-based SESAM mode-locked fiber oscillator utilizing an all-optical repetition rate controller is presented in the experimental section of this chapter. The analysis of timing jitter of different total cavity dispersion Yb-based SESAM mode-locked lasers and characterization of a few all-fiber repetition rate controllers are also introduced there.

3.1 Literature review

3.1.1. Types of mode-locked fiber oscillators

Mode-locked fiber oscillators are essential for many ultrafast laser systems used in applications such as spectroscopy [79], nonlinear microscopy [80], x-ray light sources [81], and frequency-comb spectroscopy [82] due to their reliability, compact size, and low cost. There is a huge variety of techniques and cavity designs that are used for constructing passively mode-locked lasers. In general, all-fiber lasers can be configured into one of two fundamental layouts: Fabry-Perot (standing wave) cavity or ring cavity. Pulse generation

arises from a balance between loss mechanisms and spectra and temporal gain, as well as from a balance between dispersion and nonlinearity.

A simple passively mode-locked fiber laser design can be achieved by implementing an artificial saturable absorber (nonlinear-optical loop mirror [83] or nonlinear amplifying loop mirror (NALM) [84]) into a ring cavity by a fiber coupler [85,86]. Due to the figure-eight cavity shape, these lasers are often called figure-eight fiber lasers. The intra-cavity pulse is split into two equal replicas by beam coupler before entering the NALM that one of them propagates clockwise, meanwhile another counter-clockwise. As a result of the asymmetrically placed amplifier, the counter-propagating pulses have different intensities most of the time in the loop, which leads to a difference in accumulated nonlinear phase after the one roundtrip. The pulses hereafter are recombined and interfere at the coupler before they return to the laser cavity. The nonlinear phase difference between the pulses determines whether the NALM is reflective or transmissive. In that way, NALM acts as a fast saturable absorber. As a result, the low-intensity wings of the pulses are rejected, meanwhile, high-intensity peaks are transmitted and amplified what causes pulses to be shortened in time.

Another type of passively mode-locked fiber laser based on a ring cavity exploits nonlinear polarization rotation (NPR) [87]. During the propagation in the oscillator cavity, the pulse peak and wings exhibit different polarization states what leads to uneven transmittance through the polarizer. The wings of the pulse are suppressed, therefore transmitted pulses become shorter. Since the polarization rotation appears via the Kerr effect, in combination with the polarizer it forms a very fast artificial saturable absorber. That allows attaining a passive mode-locking of ultrafast laser pulses. This mode-locking technique can also be applied to the lasers with the Fabry-Perot cavity design.

The NPR-based fiber laser can be assembled from standard off-the-shelf components with large flexibility in cavity design. The laser self-starting can be initiated from a noise level when sufficient power inside the cavity is reached. Furthermore, due to the origin of mode-locking, there are no degrading elements that fail over time therefore this all-fiber design is compact and seems robust. However, NPR-based lasers typically exploit non-polarization maintaining fibers what leads to instability of polarization state in fiber due to change of temperature or mechanical stress. To minimize this stability problem, polarization-maintaining fiber-based designs [88–90] are proposed, but they are harder to implement in all-fiber schemes. Nevertheless, the long-term exposure to the environmental disturbances will ultimately

produce a polarization drift and probably will lead to failing to mode-lock. Another solution to increase long-term stability and expand NPR laser's abilities is based on electronic polarization controllers (EPC) [91] installed into the cavity, that can accurately adjust the polarization of pulses. EPC altogether with smart polarization control algorithms allows realizing of smart self-starting lasers with electronically selectable pulsation regimes and output parameters [92–94]. These lasers could also automatically recover a mode-locking state which was lost due to some external environmental influence. Due to flexibility and reliability, automatic mode-locking techniques are the field of interest and underwent tremendous growth in the last decade.

A different subclass of passively mode-locked fiber lasers relay on a saturable absorber incorporated in the Fabry-Perot cavity. There are a variety of saturable absorbers made of novel materials which were successfully demonstrated in fiber oscillators such as graphene [95], carbon nanotube [96], perovskite [97], topological materials [98], and transition metal dichalcogenides [99]. However, they are outperformed by an older technology - a semiconductor saturable absorber mirror (SESAM) [100,101]. The SESAM is a device, that can absorb low energy radiation and transmit high energy radiation leading to selective amplification. A common mode-locking regime that allows achieving more stable ultrafast almost transform-limited pulses is called soliton mode-locking [101,102]. In this case, selective amplification is necessary only to start the mode-locking process and stabilize soliton, meanwhile, the pulse formation is caused by the interplay between the self-phase modulation (SPM) and negative group-delay dispersion (GVD). The disadvantage of these oscillators is the long-term degradation of the SESAM module, however, optimized cavity design can ensure a lifetime way above 10000 hours [103].

The total cavity dispersion has to be negative in order to realize a soliton mode-locked fiber lasers, therefore at <1.3 μm wavelengths, where standard silica fiber has normal dispersion, additional challenges have to be solved. To compensate total dispersion addition devices with anomalous dispersion are implemented in the laser cavity, such as prism pairs [104], gratings pairs [89], photonic crystal fibers [105], and chirped fiber Bragg gratings (CFBG) [106]. For the integration of prism pairs and gratings pairs, part of the oscillator cavity inevitably has to be in free space, therefore this solution is more sensitive to environmental conditions. The all-fiber solution can be achieved with the photonic crystal fiber, nevertheless, it has to be relatively long to compensate for total cavity dispersion, which leads to limitations in the

maximal repetition rate of the oscillator. Meanwhile, the CFBG not only can be integrated into all-fiber cavity design, but can also induce from a very small up to relatively large negative dispersion, and does not increase cavity size, therefore, it is the component of choice in most cases.

Lately, a new type of oscillator, the so-called Mamyshev oscillator [107,108], became a field of interest. The principle of operation is based on substantial spectral broadening due to SPM and spectral filtration with two bandpass filters, that have no overlap in transmission. It works as two cascaded Mamyshev regenerators [109]. The bandpass filter is selected in a way, that it blocks initially-launched radiation and only new generated wavelength due to SPM could be transmitted, thus it works as an effective saturable absorber. With another cascade, where the bandpass filter transmittance is shifted to the other spectral side, this effect is enhanced and 100% modulation depth is achieved, therefore, background radiation is strongly suppressed. The mode-locking state depends on the spectral separation between the two filters - the larger the separation the greater spectral broadening is required. The Mamyshev oscillator can support huge nonlinear phase shifts (up to ~60π) and MW level peak powers directly from the oscillator what is around in order higher than from any other technology of mode-locked fiber oscillators [108]. Another advantage of the Mamyshev oscillator is that it can be realized in an all-fiber design [110].

Despite the high output parameters and robust all-fiber design, there are some drawbacks the self-starting is difficult to achieve. There are several methods for starting the oscillator, such as pump diode power modulation [110], external seed pulse injection [107,111], and incorporation of an auxiliary cavity [112]. By solving self-starting shortcomings, the Mamyshev oscillator may become oscillator design of choice with new performance levels which will enable new applications [113].

3.1.2. Repetition rate control methods for fiber oscillators

A common method of repetition rate control is based on movable mirrors mounted on piezoelectric transducers (PZT) in the free-space part of the laser resonator cavity [114–118]. Due to the physical change of resonator length the round-trip time changes as well as the repetition rate. This method has some disadvantages, such as sensitivity to changes of ambient conditions, higher vulnerability to environmental influences, the requirement of high voltage

driving of piezo actuators, and undesired mechanical resonances. The PZT itself has a self-resonance in high frequency, which is determined by the thickness of the element, however, when a PZT is mounted into the resonator, other resonances arise due to acoustic vibration coupling with every component. Various design improvements of PZT mounting were proposed [119–122], that allowed to reduce resonances and increase bandwidth up to 120-500 kHz. However, they are difficult to produce, have a short travel range and the size of the usable mirror is limited, for some cases even down to 2x2x0.7mm [122], therefore, the usage is limited.

Another widespread method, which avoids mechanical resonances is based on an electro-optic modulator (EOM) placed in intracavity [123–126]. When the control voltage is applied to the EOM, it induces a small refractive index change what leads to a small change in roundtrip time as well as to change in the repetition rate. This method is one of the fastest - the reported bandwidths range from several hundred kHz up to a few MHz [127]. However, the EOMs cannot always be implemented, they are not possible in short cavity lengths, add complexity to the system, introduce dispersion, and have limited range, therefore are not suitable for applications where more than μm-level fluctuations of oscillator compensation is required.

To avoid the disadvantages of free space EOM and PZT, all-fiber solutions are desirable. One of the methods to change the repetition rate of the fiber oscillator is very similar to the PZT, but instead of length adjustment in free space, optical fiber is mechanically stretched using the special piezoelectric actuator [127–129]. This all-fiber design approach allows minimizing the direct environmental influence. Nevertheless, due to the fiber-attached PZT solution line becomes much slower in comparison to the free space case, moreover, these devices consist of movable mechanical parts which could wear off over time and have to be replaced.

There are few all-optical methods for repetition rate control in fiber oscillators that eliminate mechanical wear and vibration problems. One of them is based on pump power modulation of the gain fiber [130,131]. However, it utilizes wavelength change and significantly affects other pulse parameters. Therefore, this solution is limited and is not suitable for applications where the fixed wavelength or stable pulses parameters are required.

Another all-optical solution is based on an EPC which is inserted in a mode-locked laser cavity [129,132]. By adjusting the applied voltage on EPC, the mode-locked states could be accurately selected and the repetition rate can

be precisely controlled [94,133]. Since the repetition rate is controlled in a manner of changing the oscillator spectrum, this solution is not suitable for applications where constant pulse parameters are required. Another drawback is that this technology can be only applied to the lasers which are mode-locked by nonlinear polarization rotation [87].

A different approach on fiber laser repetition rate control, which helps to overcome the above-listed shortcomings, exploits refractive index n modification [127,129,134–136]. In this case, optical length D ($D = nL$) is changed, meanwhile geometrical oscillator length L is fixed. The main mechanism of this modification is pump-induced absorption and gain change in an active media, which according to the Kramers-Kronig relation, also changes the refractive index [137]. In addition, due to absorbed pump power, thermal refractive index change is induced, which has the same sign but is significantly slower [138]. This thermal contribution has to be taken into account and compensated with an additional slow control line, for example with temperature control of the oscillator. This all-optical method is compact and robust, can be easily integrated, avoids mechanical wear off and vibrations, therefore, maintenance is not required.

3.1.3. Phase-locked loop technique for mode-locked fiber laser

The most common active repetition rate stabilization method for fiber mode-locked oscillator is based on the phase-locked loop (PLL) technique [139], due to its simplicity and economy [140–142]. The standard setup of the phase-locked laser is presented in Fig. 3.1(a). The phase error circuit is used to lock the laser repetition rate to the external precise reference frequency. Part of the laser output is split into a photodiode to monitor the repetition rate. The registered electrical signal is filtrated from high-frequency noise and amplified up to a similar level as the frequency reference. Then both signals are mixed by the phase detector, which produces a phase-error signal. The loop filter is used to eliminate AC components, thus the only DC signal is extracted. This DC signal is sent to a repetition rate controller (RRC), which tunes laser repetition rate and compensates for the measured phase error. This auto-adjusting circuit realizes standard PLL between the reference source and the laser.

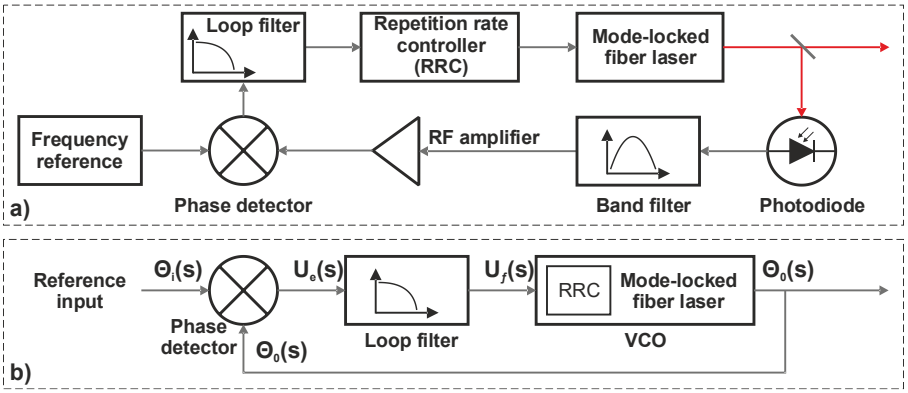

Fig. 3.1. a) Setup of a standard phase-locking of the mode-locked laser. **b)** Block diagram of the standard PLL. The abbreviations stand for: RF – radio frequency, RRC – repetition rate controller, VCO – voltage-controlled oscillator, PLL – phase-locked loop.

To analyze this PLL circuit, it can be cast into a standard form consisting of three basic functional blocks: phase detector, loop filter, and voltage-controlled oscillator (VCO) (Fig. 3.1(b)).

A phase detector is a device delivering an output signal that is proportional to a phase difference between two input signals. In the complex frequency domain, when the phase error signal is small, it can be expressed by its argument [142]:

$$U_e(s) = k_d\Theta_e(s) = k_d\big(\Theta_i(s) - \Theta_o(s)\big), \tag{3.1}$$

where the $U_e(s)$ is phase error signal generated from the detector, k_d is detector gain, $\Theta_i(s)$ and $\Theta_o(s)$ are the phase arguments of the input reference and lase output signals respectively, and $\Theta_e(s)$ is the phase argument of the error signal.

The loop filter is the bandpass filter with the transfer function $F(s)$, which eliminates higher harmonics frequencies from the PD error signal and leaves only filtered DC part ($U_f(s)$) [142]:

$$U_f(s) = F(s)\mathrm{U}_e(s), \tag{3.2}$$

The last block in the diagram is the VCO. In a typical electronics circuit the frequency ω_t of VCO output signal is directly proportional to the control signal U_f [142]:

$$\omega_t = \omega_0 + \mathrm{K}_0 U_f, \tag{3.3}$$

where ω_0 and K_0 are the center frequency and gain of the VCO respectively. However, in this case the VCO is not a single device like in the standard

electronic circuit, it consists of RRC and the laser, therefore a different response model is required.

The repetition rate f_{rep} of the laser is determined by laser cavity length. The original cavity length (or optical length) L_0 is adjusted by RRC adding a small correction $l(t)$, thus the repetition radian frequency is expressed by [142]:

$$\omega_t = \frac{d\Theta_o(t)}{dt} = \frac{2\pi c}{L_0 + l(t)}, \tag{3.4}$$

where $\Theta_0(t)$ is the phase argument of the laser output signal and c is the speed of light. This expression is valid for the ring cavity, therefore in the linear cavity case dominator should be multiplied by 2. By assuming that L_0 is much larger than $l(t)$, we can derive a modified VCO model equation [142]:

$$\Theta_o(s) = \frac{2\pi c k_0}{s(T_0 s + 1)L_0^2} U_f(s), \tag{3.5}$$

where $U_f(s)$ is input control signal, k_0 is the RRC regulation gain and T_0 is the time-delay parameter of the RRC.

Assuming, that the laser is phase-locked, a linear mathematical PLL model can be developed to analyze the system [142]. The mechanism of the PLL is described by three functions: open-loop transfer $G(s)$, closed-loop (system) transfer $H(s)$, and error-transfer $\mathrm{H}_e(s)$ function, which are given by [142]:

$$G(s) = \frac{\Theta_o(s)}{\Theta_e(s)} = \frac{2\pi c k_d k_0 F(s)}{s^2 L_0^2 T_0 + s L_0^2}, \tag{3.6}$$

$$H(s) = \frac{\Theta_o(s)}{\Theta_i(s)} = \frac{2\pi c k_d k_0 F(s)}{s^2 L_0^2 T_0 + s L_0^2 + 2\pi c k_d k_0 F(s)}, \tag{3.7}$$

$$\mathrm{H}_e(s) = \frac{\Theta_e(s)}{\Theta_i(s)} = \frac{s^2 L_0^2 T_0 + s L_0^2}{s^2 L_0^2 T_0 + s L_0^2 + 2\pi c k_d k_0 F(s)}. \tag{3.8}$$

These combined transfer functions could be used to calculate or simulate characteristics of the PLL system, therefore they are essential for analysis and design purposes [143].

3.1.4. Phase noise and jitter measurement methods

The phase noise measurement is one of the most common methods to analyze the oscillator's short-term frequency instability. The power spectrum of an ideal oscillator would be delta function (Fig. 3.2(a)), however, due to repetition rate instabilities phase noise function has sidebands (Fig. 3.2(b)).

The phase noise is a frequency domain representation, usually described by the ratio of the power density in a 1 Hz bandwidth at an offset frequency $f_s + f_m$ from the carrier to the power of the carrier signal [144]. Since these sidebands are symmetrical, phase noise is usually described by a single sideband phase noise power spectrum ($L(f)$) as shown in Fig. 3.2(c), where noise in dBc/Hz is plotted as a function of frequency offset f_m.

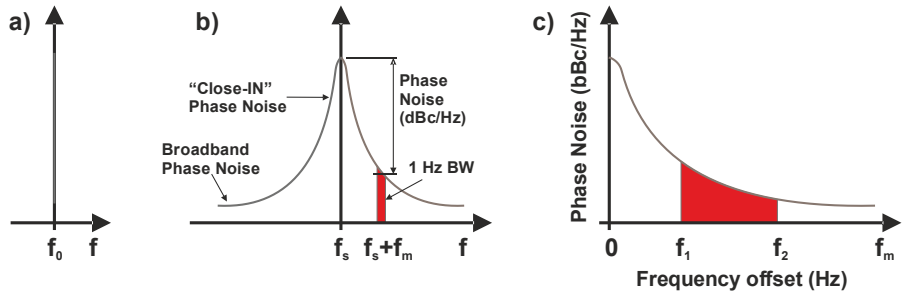

Fig. 3.2. a) Power spectrum of the ideal oscillator. **b)** Oscillator power spectrum due to phase noise. **c)** Phase noise plot.

Due to one sideband, the $L(f)$ includes only half of the noise power, therefore $L(f)$ is related to the phase noise spectrum $\Phi(f)$ as [145]:

$$L(f) = 10\log\left(\frac{1}{2}\Phi^2(f)\right), \tag{3.9}$$

$$\Phi(f) = \sqrt{2 \cdot 10^{\frac{L(f)}{10}}}. \tag{3.10}$$

In the frequency domain, the oscillator's phase noise is equal to jitter scaled by $2\pi f_s$ [145]:

$$\Phi(f) = 2\pi f_s(f)\,. \tag{3.11}$$

To obtain a timing jitter in desired frequency offset bandwidth from phase noise (Fig. 3.2(c)), the phase noise scaled by $1/2\pi f_s$ has to be integrated over frequency range from f_1 to f_2 in power density [145]:

$$\Delta t_{rms} = \frac{1}{2\pi f_s}\sqrt{\int_{f_1}^{f_2}\Phi^2(f)df} = \frac{1}{2\pi f_s}\sqrt{2\int_{f_1}^{f_2}10^{\frac{L(f)}{10}}df}. \tag{3.12}$$

In order to extract timing jitter, first of all, the phase noise power spectrum has to be measured. There is a number of different measurement techniques and methods which have some advantages and limitations, therefore a suitable one has to be chosen for the measured source. Most common, widely used, and listed in order of increasing precision are those [146–148]: direct spectrum

technique, frequency discriminator method, phase detector method (PDM), and two-channel cross-correlation technique.

The direct spectrum technique is one of the simplest and oldest for making phase noise measurements. A typical block diagram of this technique is represented in Fig. 3.3. The signal for the device under test (DUT) is input into a spectrum analyzer which directly measures the power spectral density of the oscillator. Since the spectral density is measured without filtering powerful carrier frequency, this method can be limited by spectrum analyzer dynamic range. Thus, this method is not suitable for close-in phase noise measurements, but it can be used for the evaluation of DOT with relatively high noise. For practical applications, measurements are valid as long as the internal phase noise of the analyzer at the offset frequency is lower than the noise of the DUT. Another important condition is the low amplitude noise. Most of the spectrum analyzers do not differentiate amplitude noise from phase noise, therefore it has to be significantly below phase noise level (~10 dB).

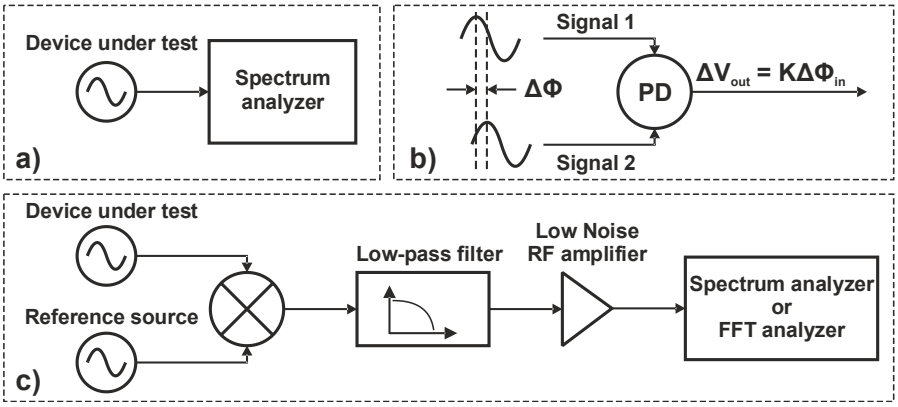

Fig. 3.3. a) The direct spectrum measurement technique. **b)** A basic concept of the phase detector techniques. **c)** The basic block diagram of measurement using the PDM method.

To separate amplitude noise from phase noise, a phase detector technique could be applied. A basic concept is presented in Fig. 3.3(b). The phase detector is a device, which converts the phase difference of two input signals into a voltage at the output. If the phase difference between signals is set to 90°, the nominal output voltage is equal to 0 Volts and sensitivity to amplitude noise is minimal. Any phase fluctuation between two inputs results in a voltage fluctuation at the detector output.

The basic block diagram of the PDM method is presented in Fig. 3.3(c). The DUT and reference signals are combined in the double-balanced mixer.

The system behaves as a phase detector if the reference source is adjusted that both input pulses are at the same carrier frequency f_c and in phase quadrature (phase difference of 90°). The mixer produces sum-frequency ($2f_c$) which is filtered by low-pass filter, and the difference frequency (DC) of the average amplitude of 0 Volts. The DC voltage is then amplified using a low noise amplifier and measured by the signal or fast Fourier transform (FFT) analyzer. The dc voltage fluctuations are directly proportional to the combined noise of the two input signals. For accurate measurement, the reference signal should be well characterized or with much lower noise than DUT.

Setting the two input sources in phase quadrature is not always a very easy task, therefore a feedback system can be used to solve an issue. The feedback forms a PLL that controls the reference signal phase to retain quadrature. The PLL takes feedback from the output of the low pass filter and acts in a way to minimize the signal to 0 Volts. This modified PDM method is called the reference source/PLL method.

Another way to perform noise measurement is the frequency discriminator method. In this case, the signal from DUT is split into two paths, one with the delay line and the other with the phase shifter. Thereafter, two channels are recombined in the mixer (phase detector). The delay line converts frequency fluctuations to phase fluctuations, meanwhile, the phase shifter is used to determine the phase quadrature required for the mixer. Then, the phase detector converts phase delay fluctuations between two paths into voltage fluctuations, that can be measured using a baseband analyzer as frequency noise. Finally, the frequency noise is then converted to phase noise.

A modified version of the analog delay-line discriminator method, which can measure relatively large phase noise, is called the heterodyne digital discriminator method. Differently from the analog case, the DUT signal is down-converted to a fixed intermediate frequency, using a local oscillator which's frequency is locked to the input signal.

Finally, the last listed way to measure phase noise is the two-channel cross-correlation technique. In this case, the DUT signal is split into two identical reference source/PLL systems, then the cross-correlation between the output signals is performed. The noise from the DUT is coherent in both paths and are not affected by the cross-correlation, meanwhile, the internal noise of each channel is incoherent and is suppressed by the cross-correlation at the rate of $\sqrt{M}$, where M is the number of correlations. This technique achieves superior measurement sensitivity at a high number of correlations, however, the increasing number reduces the measurement speed.

Modern signal source analyzers usually have a few of the mentioned techniques already built-in in the device, that can be selected individually depending on the analyzed DUT.

3.2 The development and demonstration of all-optical repetition rate stabilization methods for ultrafast Yb-based SESAM mode-locked fiber oscillator

Material related to this section was published in A2

The precise control of laser frequency is crucial for some applications. For example, high-intensity lasers usually based on the optical parametric chirped pulse amplification (OPCPA) technology [149] require a stable and precisely controlled repetition rate of the oscillator in order to synchronize all experimental equipment. Another example is SFG spectrometry, where hybrid SFG systems are used. It requires the implementation of two different lasers (visible and tunable infrared) which have to be synchronized with the timing jitter lower than the visible channel pulse duration [64]. One of the most common solutions for tunable femtosecond infrared channel is based on Ti:Sapphire systems, which can be often found in research labs, meanwhile narrowband robust picosecond lasers with simple synchronization solutions for the visible channel are required. For precise synchronization of the picosecond laser system, the timing jitter of each subsequent master oscillator pulse must be in the femtosecond timescale [150].

The simple, robust all-fiber design of soliton mode-locked laser is the top choice as a seed for laser systems of mentioned applications among other types of fiber lasers. However, the pulse formation mechanism is rather complex and usually induces an additional frequency noise to the slow thermal variation of the cavity length. Therefore, overall timing jitter is determined by the interplay between an amplified spontaneous emission (ASE), dispersion and nonlinearity of an optical cavity, soliton energy, and spectral filtering [151]. Some induced nonlinear frequency noise could be effectively suppressed within the locking bandwidth of the PLL. Even so, the remaining part of noise outside the locking bandwidth contributes to the overall timing-jitter of the fiber oscillator.

In this section, we introduce an experimental study of timing jitter in all-fiber ytterbium-doped soliton mode-locked all-PM fiber oscillator with various amounts of total anomalous cavity dispersion, determined by CFBG.

Based on this study, a few different all-fiber repetition rate control schemes were tested targeting to use them in a mode-locked fiber laser resonator and to achieve femtosecond timing jitter. Finally, a mode-locked fiber oscillator operating at 1030 nm and using a piece of Er-doped fiber as a phase controller was precisely locked to an external RF source with a typical RMS timing jitter below 200 fs. In addition, a simple setup for timing jitter measurement at lower frequency offsets was proposed and characterized.

3.2.1. Phase noise and timing jitter analysis of ultrafast Yb-based SESAM mode-locked fiber oscillator

The timing jitter of the free-running soliton mode-locked oscillator strongly depends on its design as it determines final pulse duration and energy whose fluctuations contribute to the timing instabilities [151]. At 1030-1064 nm operating wavelength range, for soliton pulse formation, the CFBG with anomalous dispersion is necessary to compensate for the normal dispersion of an optical fiber. To determine the main source of these instabilities we assembled several mode-locked oscillators with different CFBGs, which dispersion was ranging from -0.15 ps^2 to -8.41 ps^2, spectral bandwidth varied from 18 nm to 1.2 nm, and maximum reflectivity was from 15% to 80%. The repetition rate was set to be around ~40 MHz and therefore the total fiber dispersion for a round trip was approximately 0.1 ps^2. For a soliton fiber laser, the amount of total oscillator dispersion (D_2), which is the sum of CFBG dispersion and fiber dispersion, determines oscillator pulse duration and its energy [152]. The schematic of the ytterbium-doped active fiber-based oscillator is shown in Fig. 3.4. For mode-locking and reliable self-starting of an oscillator, a SESAM was used as a second mirror of the fiber resonator. The beam splitter (BS) with a division ratio of 70/30 delivered two outputs (OUT1 and OUT2). The splitter was also used to preserve only one polarization state in the resonator. Depending on the CFBG parameters, the oscillator was pumped with 55-65 mW optical power to achieve a stable single-pulse regime. The output power at OUT1 output was ~1.15 mW for the lowest dispersion (-0.05 ps^2) oscillator and ~6 mW for the highest dispersion (-8.31 ps^2) oscillator.

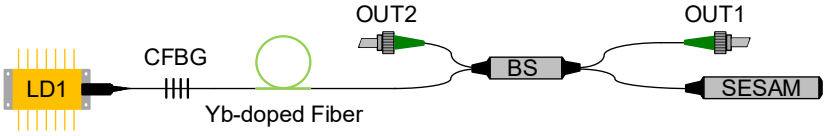

Fig. 3.4. The setup of the soliton SESAM mode-locked Yb-based fiber oscillator.

As illustrated in Fig. 3.5(a), the experimental data of pulse duration and energy of soliton mode-locked oscillator follows the $\sqrt{|D_2|}$ dependence on dispersion. Lower total cavity dispersion of an oscillator determines lower pulse energy and shorter pulse duration. The oscillator pulse shape varies from near to Gaussian at lowest dispersion values to Sech^2 at highest values of anomalous dispersion. For the lowest dispersion oscillator, the amount of total fiber dispersion is comparable to the CFBG dispersion, therefore a longer cavity significantly reduces the transform-limited pulse duration (Fig. 3.5(b)). However, at close to zero anomalous dispersion, the oscillator becomes unstable.

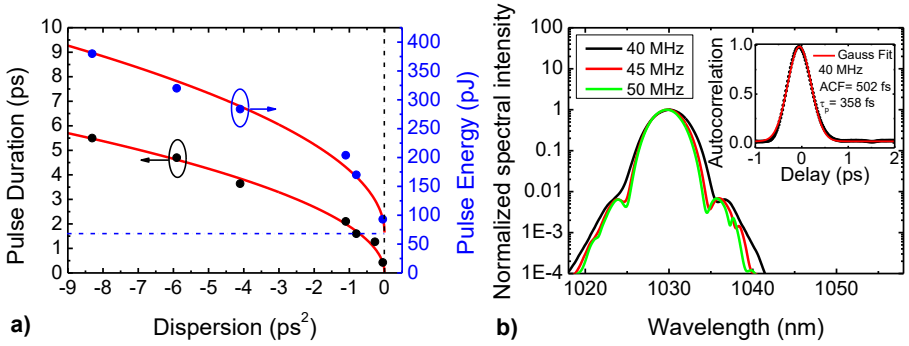

Fig. 3.5. a) The pulse duration and pulse energy of SESAM mode-locked fiber oscillators with different amounts of total anomalous cavity dispersion. **b)** The spectra of mode-locked pulses of the lowest total cavity dispersion oscillator at different repetition rates (-0.05 ps^2 @40 MHz, -0.06 ps^2 @45 MHz, -0.07 ps^2 @50 MHz). The inset shows an autocorrelation trace of the shortest pulse delivered from the SESAM mode-locked oscillator using -0.15 ps^2 CFBG with the total cavity dispersion of -0.07 ps^2.

In order to determine the source of instabilities, it is a common practice to measure phase noise in the frequency domain instead of measuring period jitter in the time domain. For phase noise measurements Keysight E5052B signal source analyzer (SSA) was used. Measurement results of -0.07 ps^2 and -1.12 ps^2 total cavity dispersion oscillators are shown in Fig. 3.6(a). The green dashed line indicates the theoretical quantum-limited phase noise of each oscillator which was estimated by using the following equation [151,153]:

$$L(f) = C\frac{\theta h\nu}{P_{avg}}(f_{rep}\tau_p)^2 l_{total}\frac{1}{(2\pi f)^2}. \quad (3.13)$$

Here, the $L(f)$ is double-sided timing jitter power spectrum density (PSD), C is the constant for soliton pulse shape (0.53 for sech^2 and 0.66 for Gaussian

pulse), θ is the excess noise factor, $h\nu$ is the photon energy, P_{avg} is the intracavity average power, f_{rep} is the repetition rate of the oscillator, τ_p is the pulse duration at FWHM, l_{total} is the total roundtrip intracavity losses, and f is the frequency offset. To calculate the timing jitter for -0.07 ps^2 dispersion oscillator, we used a constant for Gaussian pulse shape of 0.66, an excess noise factor of 3, the calculated intracavity power of 2.68 mW, the repetition rate of 56 MHz, 550 fs pulse duration, and the total intracavity losses of 80% were used. Meanwhile, for -1.12 ps^2 dispersion oscillator constant for sech^2 pulse shape of 0.53, an excess noise factor of 3, the calculated intracavity power of 5.65 mW, the repetition rate of 52.8 MHz, 2770 fs pulse duration, and the total intracavity losses of 80% were used. The intracavity power was calculated from measured output power at a 30% port of 30/70 beam splitter. The measured Phase noise over the whole frequency offset was slightly larger than theoretical quantum-limited phase noise because of other timing jitter sources such as Gordon-Haus timing jitter [154]. The difference above 100 kHz was caused by measurement setup limitations. For -1.12 ps^2 dispersion oscillator below 1 kHz offset, there was a notable increase in phase noise compared with the theoretical simulation which was not the case for -0.07 ps^2 dispersion oscillator. This indicated higher sensitivity to vibration and thermal perturbations for this type of oscillator. In addition, an oscillator with the lower total cavity dispersion demonstrated smaller theoretical and measured phase noise over the whole frequency range. These results could be used to design a low phase noise oscillator and to choose a suitable delay line for a PLL for further noise reduction.

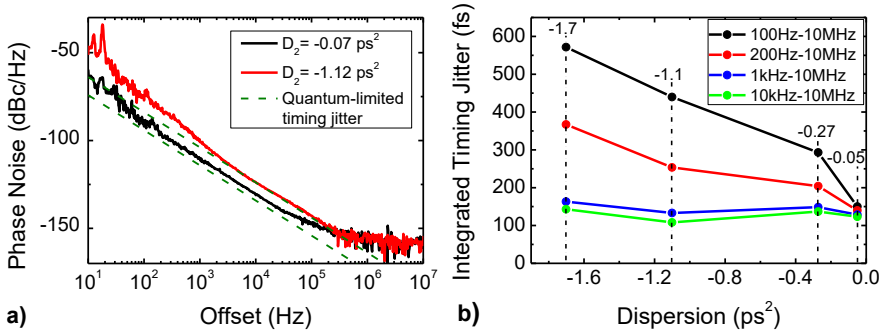

Fig. 3.6. a) Phase noise measurements of fiber oscillators with different total cavity dispersion. Measurements were made at 500 MHz carrier frequency. **b)** The integrated timing jitter of fiber oscillators with different net cavity dispersion, measured at several offset frequencies.

By integrating the measured phase noise from different frequency offsets, it was important to show the main difference of total timing jitter for different oscillator configurations. The measured phase noise of four mode-locked oscillators with -0.05 ps^2, -0.27 ps^2, -1.1 ps^2, and -1.7 ps^2 total cavity dispersion was integrated at different offsets from 100 Hz, 200 Hz, 1 kHz, and 10 kHz in order to distinguish the difference at each segment (Fig. 3.6(b)). Most of the timing jitter arose from the lower frequency contribution and this contribution was higher when the total oscillator dispersion was higher. Although the same total timing jitter value can be achieved at different frequency offset ranges, noise suppression within lower bandwidth is required for a lower total dispersion oscillator. For OPCPA systems, the timing jitter has to be only a few hundreds of femtoseconds [155], which is possible to achieve with all mentioned oscillator configurations by using PLL and delay lines with different response times. However, higher frequency electronic devices are more complex. The commonly used all-fiber piezoelectric actuators usually have undesirable resonances which could degrade phase noise at higher frequencies. In contrast, there is a simple all-fiber solution for frequency control based on Er-doped fiber. By choosing certain pumping power of an active fiber or using a feedback loop, there is a possibility to induce fast and controllable phase shift, which is suitable for noise suppression down to 1 kHz offset range [138]. Furthermore, to avoid a complex design of low noise fiber oscillators, lower cavity dispersion could be an optimum choice, which would allow implementing a low bandwidth (<100 Hz) fiber delay line and simpler feedback electronics scheme.

3.2.2. Demonstration and characterization of all-fiber repetition rate controllers

In order to define the response time and other parameters of the Er-doped fiber-based delay line, we tested it separately, without the fiber resonator. To measure the induced phase shift in a fiber arm, the Mach-Zehnder interferometer setup was used (Fig. 3.7). The input signal for the interferometer was generated from a SESAM mode-locked Yb-doped fiber oscillator, operating at 1030 nm wavelength. The signal beam was split into two paths using a 50/50 splitting ratio fiber beam splitter. One arm was fusion spliced with the test device and another arm had two adjustable free space collimators against each other to compensate for the initial delay between the two paths and to control interference after combining beams by another 50/50

splitter. The function generator (Agilent 33521A) was used to modulate the control signal for the pump diode of Er-doped fiber. The signal from the interferometer was detected by a germanium photodetector (Thorlabs PDA30B-EC) connected to the oscilloscope (Tektronix MDO3012). We analyzed three different types of delay lines: phase shifter (1), erbium-doped fiber (2), and erbium-doped fiber with feedback loop (3).

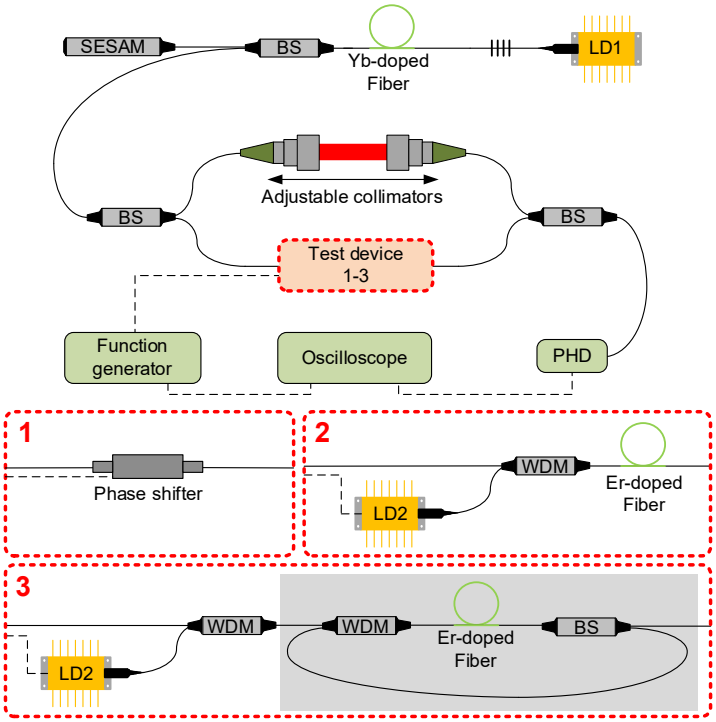

Fig. 3.7. Experimental setup of fiber-based interferometer which was used for characterization of: **(1)** all-fiber phase shifter **(2)** erbium-doped fiber **(3)** erbium-doped fiber with feedback loop (gray area). The abbreviations stand for: LD - laser diode, CFBG - chirped fiber Bragg grating, BS - beam splitter, SESAM - semiconductor saturable absorber mirror, PHD – photodiode, WDM - wavelength division multiplexer.

First, to test the interferometer and to have a reliable reference, we measured the phase shift vs frequency of a commercial all-fiber piezoelectric phase shifter (General Photonics FPS-001), which's operation principle is based on mechanical tensions of the fiber (Fig. 3.7(1)). Sine wave modulation at desired frequency was applied directly from the function generator. For fixed 2 V amplitude the measured frequency response bandwidth (Fig. 3.8) at -3 dB level was around 10 kHz, with an almost flat response up to 5 kHz. However, at higher repetition rates the undesirable resonances from the

piezoelectric actuator were observed. These resonances are inevitable for this type of device and could affect PLL stability. Therefore, the useful frequency response range of the phase shifter was up to 5 kHz.

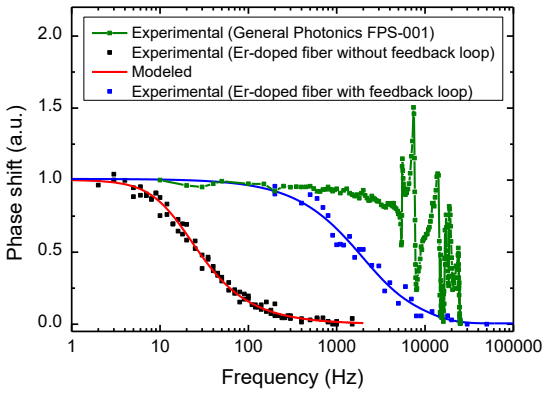

Fig. 3.8. Comparison of the all-fiber phase shifter, erbium-doped fiber, and erbium-doped fiber with feedback loop phase shift versus modulation frequency.

After the test of the interferometer, 80 cm of erbium-doped fiber which was pumped with a 976 nm laser diode was spliced in the interferometer (Fig. 3.7(2)). The wavelength division multiplexer (WDM) was used to combine the signal and pump channels. As there was no mechanical stretching of the fiber, the required change in an optical path length occurred due to refractive index modification of active fiber. By applying the sine wave modulated voltage (2 V amplitude), we were able to modulate laser diode power from 0 mW to 5 mW. The measured frequency response bandwidth of Er-doped fiber (Fig. 3.8) was around 25 Hz at a -3 dB level. To compare obtained results with the theoretical limit, we modeled an Er-doped active media using rate equations. The pump modulation induced phase shift is related to the nonlinear refractive index change due to modulation of the upper laser level [138]. This modulation could be expressed in differential equation (2), which includes erbium Er^{3+} ion spontaneous emission term $(-N/\tau)$ with lifetime τ and sine shaped pumping term $(\sin(t \times 2\pi f) + 1)$ with modulation frequency f. By solving this equation, it is possible to determine relative population change (ΔN) at a steady state (Fig. 3.9). This change of excited erbium atoms depends on both – pump modulation frequency f and the spontaneous emission lifetime τ. By fitting the measured phase shift at a different pump modulation frequency and choosing constant lifetime τ=10 ms, we got a good model agreement with the experimental data (red line in Fig. 3.8).

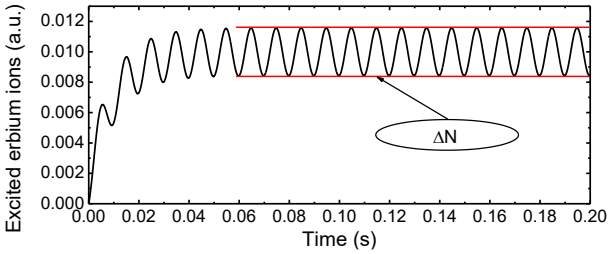

Fig. 3.9. Simulation of concentration of excited atoms in erbium fiber versus time at 100 Hz pump modulation.

$$\frac{dN}{dt} = -\frac{N}{\tau} + (\sin(t \times 2\pi f) + 1). \tag{3.14}$$

To reduce the lifetime of an active media, the novel concept using a positive feedback loop was proposed (Fig. 3.7(3)). In this case, an additional WDM and BS were used to direct the feedback signal to the Er-doped fiber amplifier. Feedback forces closed loop with Er-doped fiber to start lasing at around 1556 nm wavelength, thus shortening the lifetime of the lower excited levels of erbium ions, and therefore the overall lifetime of an active media. For this reason, the frequency response of refractive index modulation changes and depends on the amplifier parameters. As it can be seen from Fig. 3.8 (blue dots), the bandwidth of the frequency response of phase shift at -3 dB level increases to nearly 1 kHz, as compared to 25 Hz without the loop. For this frequency response measurement, the laser diode (LD2) power was modulated with the same sine wave and 2 V amplitude as in the case without the feedback loop, but setting a constant offset to increase overall power from the laser diode. This offset was required to reach the lasing threshold. The measured Er-doped fiber emission spectra at different pumping powers are shown in Fig. 3.10(a). Using a feedback loop, at a certain pumping level, an active media started lasing. This manifests itself as a sharp line in emission spectra at 187 mW and 259 mW pump powers. Moreover, at lower pump powers the spectrum was changing significantly when pumping was increased, though the lasing threshold was not yet reached. The impact of these spectrum changes on the response time of phase shift could be seen in Fig. 3.10(b). By increasing the pump power, the response time of the loop in the interferometer is constantly shortening, but at lasing threshold (187 mW) changes dramatically. Though it looks like a very attractive tool to enhance response time, it manifested an upper limit. After the pump offset was increased above 259 mW, the signal became unstable due to the thermal effects as the absorbed power also produced heat. The total amount of heat

generated along 80 cm of active fiber slightly changed the refractive index of the fiber and consequently the optical path length of the loop. Actually, thermal response input could be seen from all curves in Fig. 3.10(b). The response time of phase shift consists of two parts – fast arising from Kramers-Kronig relation and the slow caused by thermal effects. In order to use this feedback loop as a very fast delay line (>1 kHz) in a PLL system, thermal contribution influence has to be reduced, and therefore, more studies are required.

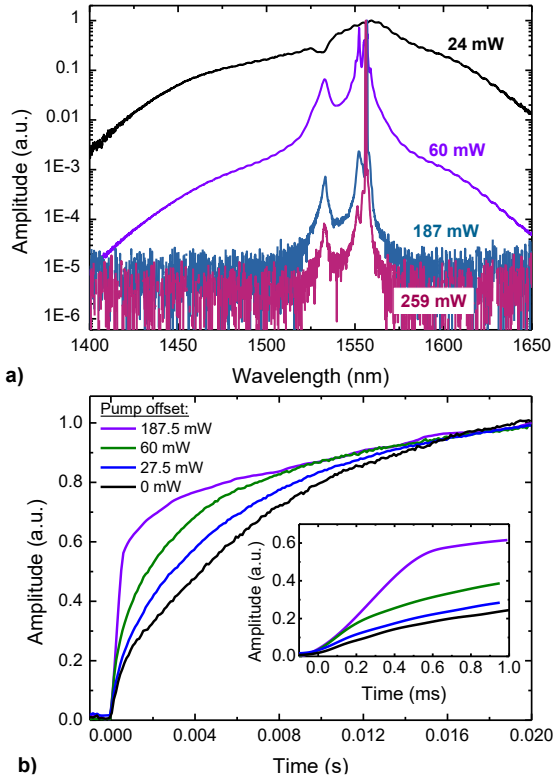

Fig. 3.10. a) Measured spectra at the feedback loop output at different pump power levels. **b)** Measured photodiode response illustrating active fiber loop response speed at interferometer output. Inset: magnified dependence in a shorter time scale.

3.2.3. Repetition rate stabilization

The analysis of fiber oscillators design and repetition rate controllers allowed us to select optimal components for the final PLL setup. For practical reasons, we decided to use an oscillator with slightly higher anomalous dispersion of -0.27 ps^2, as in this case, the self-staring of the mode-locking regime was easier to achieve at higher insertion losses from PLL components.

Nevertheless, the integrated timing jitter of the free-running oscillator at an offset from 100 Hz to 10 MHz was below 300 fs (Fig. 3.6(b)). To avoid piezoelectric resonances, we chose to use an Er-doped fiber-based phase shifter for the fast repetition rate control. To keep away from undesirable thermal effects, we used moderate powers for Er-doped fiber pumping (≤28 mW). The final layout of the fiber oscillator with the PLL option is presented in Fig. 3.11. SESAM mode-locked oscillator consisted of ytterbium-doped fiber as a gain medium, CFBG for dispersion management as well as for 1030 nm central wavelength selection, an erbium-doped fiber performing as a precise delay line, and fiber heating unit acting as a coarse delay line. Two separate laser diodes were used – one (LD1) to pump Er-doped fiber for repetition rate control and another (LD2) to pump Yb-doped fiber. The lengths of the used erbium and ytterbium active fibers were 84 cm and 40 cm respectively. The signal from InGaAs photodiode (PHD) was used to provide the oscillator pulse repetition rate for PLL electronics. The phase shift between an oscillator and a precise electronic clock produced by an RF generator (Rohde & Schwarz SMA100A) was measured and compensated by controlling precise and coarse delay lines.

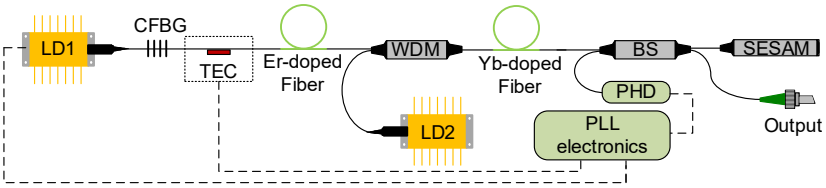

Fig. 3.11. The layout of the repetition rate controlled all-fiber oscillator. The abbreviations stand for: LD1 - repetition rate control laser diode (976 nm), LD2 - oscillator's pump laser diode (976 nm), CFBG - chirped fiber Bragg grating, TEC - thermoelectric cooler, WDM - wavelength division multiplexer, BS - beam splitter, SESAM - semiconductor saturable absorber mirror, PHD - photodiode, PLL - phase-locked loop.

The mode-locked fiber oscillator was designed to operate at ~50 MHz repetition rate producing an average power of 2 mW from the 30% port of 70/30 output beam splitter. As an additional means to avoid the drift of repetition rate, oscillator housing was thermally stabilized using Peltier elements. The temperature control of oscillator housing also allowed us to tune the repetition rate up to ~10 kHz by changing the optical path length of the fiber resonator. For precise adjustments, another Peltier element heated a short segment of fiber in order to compensate for fast thermal instabilities. An Er-doped fiber-based phase shifter was used as a fast delay line with a tuning

range of ~8 Hz. By controlling a fast delay line, the oscillator repetition rate was locked to an external 500 MHz master clock produced by an RF generator.

For precise phase noise measurements at frequency offsets below ~1 kHz, we used a simple phase detector method (PDM) [148] which could be an alternative to the direct noise measurements using a special SSA device. The phase detector consisted of a frequency mixer (Mini-Circuits ZEM-2B+) and a low-pass filter (Mini-Circuits SLP-1.9+). The optical signal from the oscillator output was registered by the fixed gain detector (Thorlabs PDA10A) and mixed with the 500 MHz RF clock signal using a mixer. The phase difference at the mixer output was filtered and registered with a digital phosphor oscilloscope (Tektronix DPO72004C). In order to measure the phase noise, the differential signal had to be saved over the long record length. Using the FFT function of the oscilloscope, the waveform was converted into frequency domain spectra. The registered spectra consisted of the phase difference between the low noise RF signal and oscillator signal. As the phase noise of RF generator signal at 560 MHz carrier frequency was significantly lower (black dots in Fig. 3.12) than phase noise of oscillator (blue dots in Fig. 3.12) at offsets below 1 kHz, the phase fluctuation mainly occurs due to repetition rate instabilities of fiber oscillator.

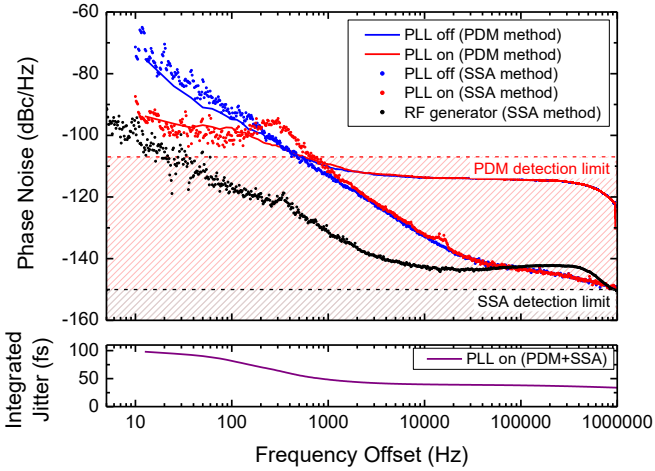

Fig. 3.12. Phase noise measurements of the lowest dispersion (-0.05 ps^2) oscillator using two different methods: PDM and SSA. Measurements were made at 560 MHz carrier frequency.

First, we compared the results obtained using the proposed PDM method with the ones measured using SSA (Keysight E5052B Signal Source Analyzer). The phase noise measurements of the lowest dispersion oscillator

(-0.05 ps^2) are shown in Fig. 3.12. Here, instead of Er-doped fiber, we used a piezoelectric phase shifter (General Photonics FPS-001) for PLL realization. The results of phase noise coincide very well up to ~500 Hz offset frequency, which is approximately a limit of low pass filter. Most of the timing jitter arises from the segment below 1 kHz offset (purple line). Using the PDM method, the intensity noise is subtracted by a frequency mixer, and therefore, the measured phase noise is lower than measured by SSA when PLL is on (red line and dots). At frequency offset below 500 Hz, the integrated timing jitter was ~100 fs, which is an approximate limit for the PDM method.

Using the PDM method we measured the phase noise of the final version of the oscillator (-0.27 ps^2 dispersion) depicted in Fig. 3.11. The results are shown in Fig. 3.13(a). Er-doped fiber-based phase shifter was pumped by 15 mW and 28 mW pump powers. The PLL electronics allowed to modulate laser diode power with ~15 mW amplitude. Without the offset (green curve), the measured singe sided frequency response of the Er-doped fiber delay line was up to ~35 Hz. At a higher pump power level (blue curve), the single-sided response time reached ~90 Hz due to decreased excited state relaxation time of Er-doped fiber. We were unable to stabilize oscillator frequency when the pump power was further increased above 28 mW. The thermally induced frequency shift was too large and too fast to compensate it using slow coarse delay lines. However, the frequency response of the Er-doped fiber-based phase shifter was fast enough to reduce the integrated timing jitter down to below 200 fs (Fig. 3.13(b)). To the best of our knowledge, it is the first time when the repetition rate of the Yb-doped mode-locked fiber oscillator was stabilized using an Er-doped fiber-based phase shifter.

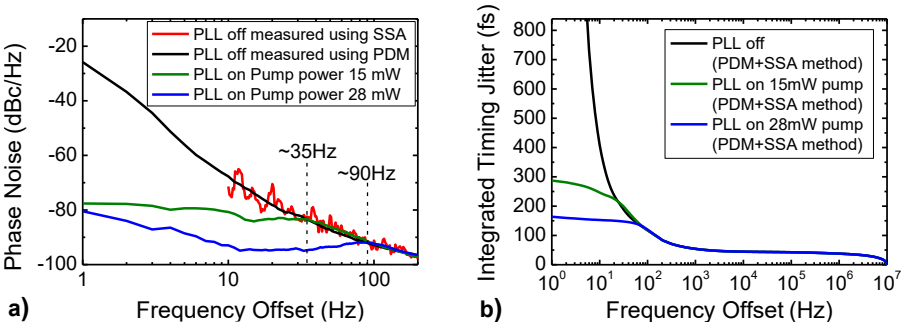

Fig. 3.13. Phase noise measurements results of the mode-locked oscillator with -0.27 ps^2 of total cavity dispersion using PDM method **(a)** and integrated timing jitter calculated from measured phase noise using both PDM and SSA methods **(b)** at two different pump levels of Er-doped fiber: 15 mW (green curve) and 28 mW (blue curve). Measurements were made at 500 MHz carrier frequency.

3.2.4. Summary of the results

In this chapter, we demonstrated a practical design of a frequency-locked mode-locked fiber oscillator operating at 1030 nm wavelength by using an Er-doped fiber as a phase shifter. At moderate Er-doped fiber pump powers (15-28 mW), we achieved stable locking of pulse repetition rate to an external RF source with RMS timing jitter below 200 fs. To increase the speed of phase control, we introduced a novel concept of the Er-doped fiber phase shifter with a feedback loop, which retained an advantage of standard Er-doped modulator robustness, but the frequency response was much faster. We were able to achieve an improvement in speed around 100 times, thus it is comparable to the standard solution of an all-fiber phase shifter. The speed of the created phase delay line could be increased even more with a higher pump offset, but requires more studies to find a way to cope with delay instabilities arising due to the increased thermal load. We have also demonstrated, that at offset frequencies from 100 Hz to 100 kHz, the lowest anomalous dispersion fiber oscillator manifested the best noise performance with an integrated RMS timing jitter below 150 fs. In contrast, the noise of the oscillator with the highest tested anomalous dispersion reached 575 fs. In order to compensate thermal and other noises at offsets below 100 Hz and to maintain strictly all-fiber configuration, an Er-doped fiber-based phase shifter could be an alternative to other types of delay lines when the integrated timing jitter below 1 ps is required. Concerning application in SFG spectroscopic systems, one needs to determine target spectral resolution and select time-bandwidth limited pulse duration accordingly. It would be preferable that the timing jitter between mid-IR femtosecond pulses and narrowband picosecond pulse would be lower than 10% of ps pulses duration. In that way, nonlinear signal fluctuations due to the timing jitter would be minimized. For example, narrowband pulses of 10 ps duration feature ~1.5 cm^{-1} bandwidth. Thus, our demonstrated method with <1 ps timing jitter between ps and femtosecond mid-IR pulses is a good choice for building a broadband SFG system.

CHAPTER 4

THE DEVELOPMENT OF THE FEMTOSECOND NIR LASER SOURCE DEDICATED FOR NONLINEAR MICROSCOPY APPLICATIONS

One of the most attractive applications for NIR laser sources is nonlinear microscopy. This application has some specifics that mainly depend on research objects – biological tissues. The nonlinear signals generated in bio tissues are quite weak, so long irradiation of the research object is needed to achieve an acceptable signal-to-noise ratio in the receiver. It means that the shortest possible pulse durations which will raise the nonlinear signal generation and as high as possible repetition rates for fast signal acquisition are preferable. At the same time, there is the upper limit in total illumination power, which is determined by biological objects degradation. Another aspect of nonlinear microscopy is pump and nonlinear signal wavelength selection. Both need to fit in a material transmission band and usually are not required to be tunable. Widely used Yb-based femtosecond lasers running at higher than 1 MHz repetition rates are attractive and robust solutions for such microscopy applications, however, the wavelength has to be shifted to the biological tissue transparency region. That motivated a search for a simple and robust method to convert laser wavelength. The following sections are dedicated to the investigation of femtosecond sources in the NIR spectral range using stimulated Raman scattering phenomena.

First of all, the advantages of femtosecond NIR sources for nonlinear microscopy are described in the literature review section. The discussion of common methods for femtosecond NIR radiation generation is also introduced. Furthermore, the synchronous pumping technique advantages and shortcomings are presented.

The development of a compact and robust femtosecond NIR laser source is presented in the experimental section of this chapter. Firstly, the search and analysis of the suitable crystals for low energy SC generation are introduced. Secondly, the validation of SC seeded SRA in the diamond crystal is shown. Finally, the novel synchronous pumped laser concept is presented.

4.1 Literature review

4.1.1. The need for femtosecond NIR laser sources

There is a huge interest in femtosecond sources of the VIS and NIR regions. They are required for many applications, such as time-resolved spectroscopy [156], multi-photon microscopy (MPM) [157,158], and frequency metrology [159]. Laser sources, generating femtosecond pulses in the infrared spectral range of 0.7-2.5 μm found their application especially in microscopy of biological tissues [160].

The penetration depth and resolution in microscopy of biological samples are limited due to light absorption and scattering. In tissues, the absorption of light arises mostly from water, collagen, hemoglobin, and lipids. Meanwhile, the scattering is caused by cells or intracellular matrix [161]. Most of the earlier research was focused on the first biological transparency window at 650-900 nm, where water and hemoglobin have a local minimum in absorption. However, due to Rayleigh and Mie scattering, the light is more scattered at shorter wave lengths, therefore longer wavelengths become the field of interest. It was shown, that despite the higher absorption (due to lower scattering), penetration depth can be maximized in the second optical window located at 1100-1350 nm between two water absorption peaks [162–164]. Limited studies have been done because of the lack of 2D NIR-CCD cameras at the time. With the improvements of NIR-CCD, their spectral response was increased up to 2200 nm, which encouraged the search for further optical windows. Shortly after, the third window at 1600-1870 nm was experimentally tested and showed even greater penetration depths [161,165]. Furthermore, the new fourth window at 2100-2300 nm was proposed, which was later tested and manifested promising results for the analysis of bone samples [166].

Another way how to increase the penetration depth and contrast of the registered image is the implementation of nonlinear microscopy [167,168]. Most common are multiphoton excited fluorescence microscopy, second and third harmonic generation microscopy, and coherent anti-stokes Raman scattering microscopy [167]. The efficiency of the nonlinear process depends on the temporal and spatial distribution of excitation light, therefore it has to be concentrated in space and time to generate sufficient signal. The key benefit of nonlinear microscopy is that the multiphoton interaction is available only in a tiny focal volume in a thick sample, thus at the out-of-focus, there is no

emission. It improves the resolution and the contrast of the registered image. The localization of the excitation is important for deep imaging as well, since all photons originated from near focus they can provide useful information. Furthermore, the located interaction allows to create the 3D images of the samples and reduces photodamage. Since high intensity is required for the multiphoton interaction, short pulse duration lasers are desirable.

By combining mentioned methods, it is possible to further enhance the parameters of microscopy systems. For example, the NIR radiation can be selected to be in the second or third optical window, meanwhile generated second or third harmonics can fit the first transmission window [169,170]. Similarly, multiphoton fluorescence excitation is easily detectable and can penetrate to a much higher depth compared to single-photon imaging [171,172], due to the large excitation and fluorescence wavelength difference.

In short, the femtosecond lasers emitting in NIR spectral range fit well both for the excitation of multiphoton fluorescence as well as for harmonics generation and allows to increase performance, thus the compact and robust laser sources for biological microscopy are needed.

4.1.2. NIR laser sources for biological microscopy

Due to the limited availability of laser sources in the NIR spectral region, nonlinear light conversion methods are often used to achieve desired parameters. One of the most established techniques to produce broadband femtosecond radiation covering the ultraviolet, visible and near-infrared spectral range is a supercontinuum generation [173,174]. To increase the spectral density of radiation at the desired wavelength, the well-established technique of OPA is used [13].

At first, the OPA was used to extend Ti:Sapphire laser systems wavelength, however, this solution is optimal for high energy and low repetition rate systems (few kHz) due to thermal load limitations [175], meanwhile, for biological imaging applications high repetition rate (MHz level) is desirable. Another drawback of this approach is the complexity and price. With the emerge of Yb-doped fiber lasers as well as Yb:KGW and Yb:YAG solid states lasers optimal compact configurations for biological microscopy were proposed [7,176,177]. They produced pulses of <50-60 fs duration in the energy range of 0.01-1 μJ and in the frequency range of 1-90 MHz with a 30-50% conversion efficiency of pump pulses to NIR region.

Another nonlinear amplification technique one can think about is Raman amplification. Each individual Raman active material has its own Raman shift, thus by selecting material and exploiting multiple Stokes orders, it is possible to design desired discrete wavelengths laser sources. Raman amplifiers is a well-developed technology in fiber optics. Starting from the pioneering article of Stolen and Ippen [178], it was followed by numerous investigations. However, as a nonlinear amplification technique of femtosecond pulses, it is not well developed yet, particularly in crystals at the NIR spectral range from 1.1 to 1.4 μm [17,179].

If the duration of the pump pulse used for SRA is similar or even shorter than the dephasing time of Raman active material molecular vibrations, the Raman gain is low. A compact single-pass configuration with a femtosecond pump, dedicated for biological microscopy, was suggested in [8]. It produced 1175 nm wavelength 25 nJ energy pulses at a 1 MHz repetition rate, however, conversion efficiency reached only around a few percent. Nevertheless, it is possible to obtain spectral broadening of the Stokes wave. The effect is induced by nonlinear processes, which highly compete with SRA and reduce Raman gain. In the case of the use of femtosecond pump pulse, it is true for all known Raman crystals. A broader spectrum of pulses obtained during Raman amplification can be compressed up to a few times shorter than pump pulse duration [179], which is favorable for nonlinear microscopy applications.

When starting from the noise level of initial signals, the threshold of SRS is high and the efficiency of generation of Stokes radiation is quite low, but seeded by proper wavelength coinciding with Stokes one, can result in efficient amplification [179,180]. Seeding of the femtosecond Raman amplifier can help in reducing the negative influence of process non-stationarity [181]. Single-stage SC seeded Raman amplifier can achieve around 10% energy conversion efficiency, therefore the multiple-stage solution is required for efficient amplification, which increases system complexity.

Another way to improve efficiency is the synchronously pumped Raman laser configuration [182,183]. In this case, a Raman crystal is placed in a ring cavity which is constructed in a way that the round-trip time is closely matched to the pump lasers pulse period. The mirrors in the cavity are highly reflective at Stokes wavelength except one, which has a typical transmission of <10% and realizes the output of radiation.

Energy effective setup with the 80 MHz Ti:Sapphire oscillator as a pump laser and 8 mm diamond crystal [9] demonstrated over 30% conversion efficiency. However, the length of the ring cavity of four mirrors had to be ~3.75 m due to laser repetition rate, which increases system dimension. Another drawback of this system is the 800 nm wavelength of the pump laser, thus the first Stokes of it is only at 890 nm, meanwhile for biological microscopy >1.1 μm wavelengths are desired. With such wavelength pump lasers, this can be achieved only in multiple Stokes order regime [184], which reduces total conversion efficiency. Due to complexity and large system dimensions, this solution is not very attractive for microscopy systems.

The more suitable system was proposed in [185], where the same 8 mm length diamond crystal was pumped with the 80 MHz 1055 nm Yb-doped fiber laser, therefore the first Stokes wavelength was at 1240 nm. The ring cavity was constructed of 6 mirrors, which allowed to maintain a footprint of <1 m in length. Despite the advantages in reduced complexity, size of the system, and desirable wavelength, the higher number of mirrors induced additional losses. Furthermore, stability requirements for a 3.75 m length cavity were almost the same.

4.2 Experimental results

Material related to this section was published in A3 and described in patent P1

Compact, reliable, and commercially available laser sources providing 1-3 μJ, <500 fs laser pulses at 1-1.1 μm spectral range, operating at MHz repetition rates and 3-5 W mean power are attractive candidates for pump sources. The SC generation could be a universal seed source both for OPA and SRA-based femtosecond laser systems. However, due to a quite low pulse energy, only a small fraction of the output could be used for SC generation, while the rest would preferably be used for pumping of the nonlinear amplifier. Therefore, bulk crystals featuring the lowest generation threshold are required. In this section we performed research of SC generation in several commonly used crystals and rarely tested for SC generation crystals (such as two sesquioxides and diamond) for subsequent nonlinear amplification, targeting femtosecond pulses generation in the NIR spectral range for potential MPM applications.

Fiber-based industrial-grade FemtoLux 3 laser (*Ekspla*) [186] was used as a pump source for all experiments. It provided up to 3 W output power at a

1 MHz repetition rate and delivered <300 fs pulses at 1030 nm central wavelength. Laser already showed positive results in wide-field SH generation microscopy [187], however, it has a fixed wavelength. To expand laser applicability to more MPM applications, the SRA scheme seeded with SC (generated in the optimal crystal) was tested and analyzed for the ability to be used as a single-pass wavelength shift add-on for FemtoLux 3 laser. A novel synchronously pumped self-seeded scheme with modified FemtoLux 3 laser was also presented.

4.2.1. Supercontinuum generation

Starting from relatively low energy pulses, optimal balance for initial pulse energy redistribution between the seed (SC) generation and pump pulses for nonlinear amplification has to be selected. Both processes are energy and intensity-demanding. The higher intensity, the higher the nonlinear conversion efficiency. It means that the pump pulse energy required for SC generation has to be minimized, but still, high enough to obtain sufficient seed energy in the desired spectral range.

SC generation research starting from the first publication on the phenomenon in a pioneering article by Alfano [173] was presented in many research articles [174,188–190]. Those articles indicate that when selecting the material for SC generation, the following parameters shall be taken into account: nonlinear refractive index, bandgap, transparency, damage resistance, and thermal conductivity. That set of requirements was our guide for material selection. The most important aspect was damage resistance, as at MHz repetition rate the most probable reason for damage – color center generation [191,192]. At a very high repetition rate, the accumulation of color centers until SC generation is fully blocked comes quite fast, so the material selection is a challenge. Transparency and thermal conductivity play an important role in the damage threshold at the high average power case. If the crystal has low transparency, a huge part of the radiation is absorbed and translated to heat, therefore increased temperature of the crystal reduces the damage threshold. Nevertheless, to have a sufficient and not limited spectrum, the crystal transparency window should cover the whole desired SC spectrum range. Low thermal conductivity at high average power affects the damage threshold in the same manner as well, the heat is not dissipated fast enough through the crystal, therefore temperature increases locally, which leads to a reduced damage threshold. It was shown by A. Brodeur et al. [193,194], that

the SC generation process depends on the material's bandgap. Results revealed, that with the increase of bandgap the blue-shift of SC increases respectively. This effect is related to a free-electron generation via multi-photon excitation (MPE), which stops the catastrophic collapse of the pulse due to self-focusing. It was shown, that the blue-shift is inversely proportional to the n_2. Self-phase modulation theory predicts, that spectral bandwidth increases at a higher value of n_2, however, due to MPE contribution bandgap plays the main role. Materials with a high n_2 inevitably come with a low bandgap [195,196], therefore materials with a high bandgap and low n_2 are the best choice to generate a blue side of the SC spectrum.

We observed some SC spectra anomalies around Raman resonance in Raman active materials, which need further investigation to understand underlying phenomena. Targeting MIR SC, we hoped that Raman active crystals will be the most efficient in shifting SC spectra to long wavelengths due to Raman assistance. The experimental results justified the said assumption.

Since the pump radiation had to be shared between the SC generator and the nonlinear amplifier, it was decided to limit the energy dedicated for SC generation to 1 μJ, while leaving the remainder for nonlinear amplification. The experimental setup of SC generation is presented in Fig. 4.1. The pump energy was controlled in the range of 10 - 1000 nJ by a waveplate (λ/2) and a polarizer (P). The transmitted optical power was measured by a power meter (PM) and used for the precise determination of the pump radiation reaching the nonlinear crystal. The second λ/2 phase retardation plate was used to control pump polarization. Then, the 3.8 mm diameter (at $1/e^2$ intensity level) collimated beam was focused into the crystal by using a lens (L1) placed on a translation stage, so that the position of the crystal respective to the focused beam waist was precisely controlled. In order to perform spectral measurements in the whole spectral range of the generated SC radiation, the beam was directed to two paths, which were selected by a flipping mirror (FM). In the first path, the Vis and NIR part of the SC spectrum was analyzed. Part of the beam reflected from a wedge (W) was used to characterize the beam profile with a CCD camera. The transmitted beam was used to measure the spectrum from 200 to 1100 nm using Avantes AvaSpec 3648 spectrometer (S1). In the second path, the IR part of the supercontinuum covering the spectral range from 900 to 2500 nm was measured with an Ocean Optics NIRQuest spectrometer. A lens (L2) and a silver-coated spherical mirror (SM) were used to focus SC radiation into fiber-optic inputs of spectrometers. For

separation of the pump radiation from the SC signal, a short-pass filter (F1) with a cutoff wavelength at 1000 nm (FESH1000, THORLABS) for the Vis-NIR region and a long-pass filter (F2) with a cutoff wavelength at 1050 nm (FEL1050, THORLABS) for IR region were used.

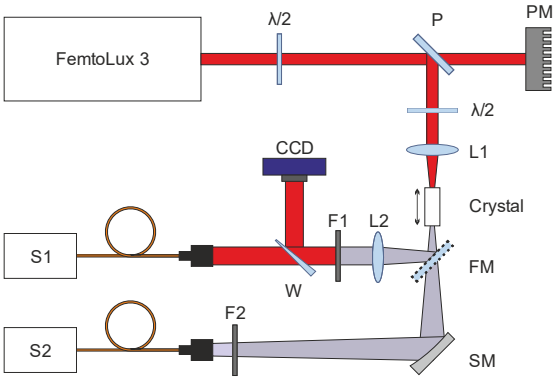

Fig. 4.1. Experimental setup of SC generation. Where λ/2 – half-wave plate, P – polarizer, PM – power meter, L(1-2) – lens, FM – flipping mirror, F(1-2) – filter, W – wedge, CCD – charge-coupled device camera, S(1-2) – spectrometer, SM – spherical mirror.

The following crystals were used in our experiments: 4 mm length potassium gadolinium tungstate (KGW), 5 mm length yttrium aluminum garnet (YAG), 4 mm length yttrium vanadate (YVO_4), 6 mm length diamond, 5 mm length yttrium oxide (Y_2O_3), 13 mm length calcium tungstate ($CaWO_4$), 5 mm length lutetium oxide (Lu_2O_3) crystals, and 5 mm length Y_2O_3 ceramics (Fig. 4.2). All samples were uncoated, undoped, and tested at room temperature. The summary of the properties of materials under investigation (linear (n_0) and nonlinear (n_2) refractive index, bandgap (E_g), thermal conductivity (k), and optical damage threshold) are presented in Table 4.1. We have calculated critical power (P_{Cr}) at which self-focusing appears for each material too, as self-focusing is important to start filamentation. For Gaussian beam the self-focusing threshold is defined by the threshold power [174]:

$$P_{Cr} = \frac{3.72\lambda^2}{8\pi n_0 n_2}. \quad (4.1)$$

where λ is the laser wavelength, n_0 and n_2 is the linear and nonlinear refractive index. Since the experimental n_2 usually contains a large measurement error, we used the predicted n_2 values for precise P_{Cr} tendency calculation. Predicted n_2 values were calculated using formalism in [195,196]. SC generation thresholds and spectral broadening were measured with a set of focusing lenses (L1) of 50 mm, 75 mm, 100 mm and 150 mm focal distances. For all

experimental focusing conditions, the position of crystals and the pump energy were adjusted in order to achieve an unmodulated spectrum (single filament conditions) and did not reach the damage threshold.

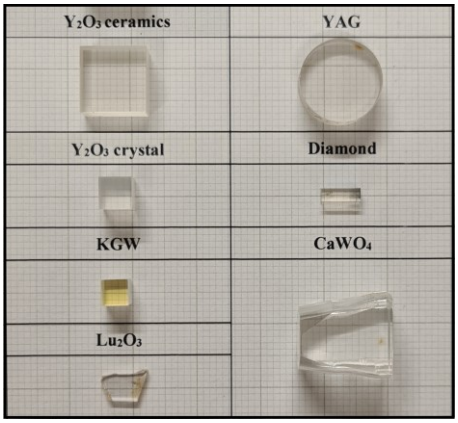

Fig. 4.2. Picture of samples of the crystals and ceramics used in the SC generation experiments.

Table 4.1. List of materials used for continuum generation and their properties.

Material	n_0 @1030 nm	n_2, 10^{-16} cm^2/W (Calc.)	P_{cr}, MW	Bandgap, eV	k, W/(m·K)	Damage threshold
KGW	2.01 (n_m) [197]	33.16	0.236	3.9 [198]	2.6 [199]	~10 GW/cm^2 [199,200]
YAG	1.82 [201,202]	6.48	1.331	5.9 [198]	9.48 [203] 13 [204]	~100 J/cm^2 @1064 nm, 10 ns [205] ~4.1 J/cm^2 @800 nm, 250 fs [206]
Diamond	2.39 [207]	5.07	1.295	5.5 [208]	~2200 [209] [210] 2000 [211]	~75-84 GW/cm^2 @1064 nm, 32 ps [212] 11.2 J/cm^2 @1064 nm, 20 ns [213] 250-280 GW/cm^2 @1064 nm, 40 ps [214]
Y_2O_3 ceramics	1.89 [215]	10.92	0.761	5.14 [216]	15.1-15.4 [217]	1.4 J/cm^2 @1064 nm, 8 ns, 0.7% doped with Ho [218]
Y_2O_3 crystal	1.89 [219]	18.98	0.438	4.54 [220]	27 [204]	-
Lu_2O_3	1.91 [219]	7.94	1.035	5.5 [221]	12 [222]	-
$CaWO_4$	1.89 (o) [223] 1.91 (e) [223]	5.6 5.48	1.484 1.5	6 [224]	4.69 [225] 16 [226]	0.5 GW/cm^2 [200]
YVO_4	1.96 (o) [197] 2.17 (e) [197]	51.02 41.62	0.157 0.174	3.6 [198]	5.23 [227] 12.1 5.1 [227] 8.9	1 GW/cm^2 [200] 6.8-10.3 GW/cm^2 @1064 nm, 40 ps [214]

Most of the investigated materials did not show any damage over time (approximately over 10 hours for each sample at the different focusing conditions) at the chosen stable single filament conditions. The only

exceptions were Y_2O_3 ceramics, which was degrading in a matter of minutes as well as Y_2O_3 crystal, which degraded instantly. From crystal optical, thermal, and physical properties (P_{Cr}) one can expect for a perfect operation as an SC generator, but in practice, it was contrary. Despite perfect optical transparency, it looks like there are too many crystalline structure defects, that trap free electrons and cause the formation of color centers. During the process of SC generation, the number of accumulated color centers grows until catastrophic damage occurs. The speed of material degradation depends directly on the number of crystalline defects. In that case, one could expect that a single crystal will operate longer than polycrystalline ceramics, however, in our experiment the results were the opposite. We can only explain this by poor crystal quality. Evolution in time of the SC spectrum in Y_2O_3 ceramics is presented in Fig. 4.3(a), in the case of focusing 390 nJ pump pulses by using a 75 mm focal length lens. The spectrum was combined from data of two spectrometers, therefore actual energy density over the whole spectrum is not accurate. A dip in the spectrum around 1 μm is due to spectral filtering of the pump signal, which could oversaturate or even damage spectrometers. The dynamic range of the spectrometers was too low to measure attenuated spectra without spectral filtering. The sample of Y_2O_3 crystal was degrading in a matter of seconds, therefore it was not possible to measure its spectrum properly. Evidence of color centers formation in Y_2O_3 materials was indicated by the visible glow inside the sample along the beam propagation path when pumped below the SC generation threshold, see Fig. 4.3(b-c).

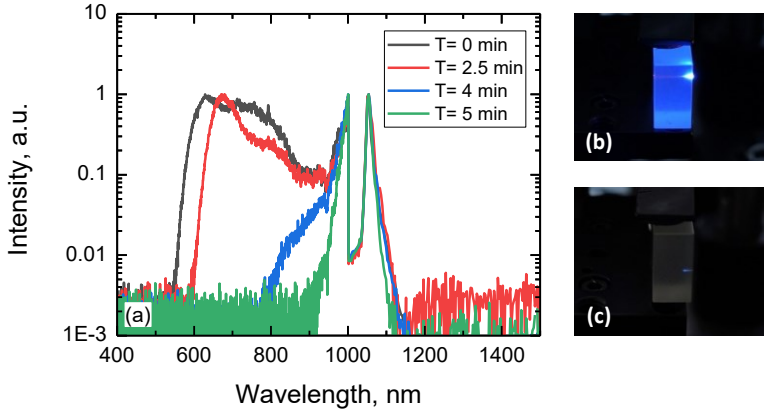

Fig. 4.3. a) Evolution in time of the SC spectrum generated in 5 mm length Y_2O_3 ceramics. **b)** View from the side of Y_2O_3 ceramics when the pump energy is higher than the SC threshold. **c)** View from the side of Y_2O_3 ceramics after a few minutes when the pump energy is lower than the SC threshold.

The summary of the SC measurement results is presented in Table 4.2. Measurements of $CaWO_4$ and YVO_4 were made at $E \perp c$ polarization, meanwhile, KGW was measured at $E \| N_m$ polarization. The threshold energy (E_{Th}) of the SC generation at which spectrum immediately broadens and filament in the crystal appears, as well as Vis-NIR and IR cutoff wavelengths and SC average power of each side ($P_{Vis\text{-}NIR}$, P_{IR}) at maximal single filament pump energy (E_{SF}), were compared for tested crystal samples at different focusing conditions. Due to limited pump energy, some samples at certain focusing conditions did not reach the threshold of multifilament condition therefore average power and cutoff wavelengths were measured at full energy equal to 950 nJ. Data for YVO_4 crystal are limited due to a very short availability for experiments in OPA. YVO_4 and KGW crystals manifested the lowest SC generation threshold, as can be expected from the results described in [198].

Table 4.2. The performance of various crystals used for the SC generation at different pump focusing conditions.

f_{L1}, mm	Material	E_{Th}, nJ	E_{SF}, nJ	Vis cutoff, nm	NIR cutoff, nm	$P_{Vis\text{-}NIR}$, mW	P_{IR}, mW
+50	KGW	220	600	585	1700	16,2	35,1
	Diamond	330	750	580	1700	38,2	77,2
	$CaWO_4$	480	850	560	1550	13,4	87,4
	YAG	770	950	480	1140	21,73	149,25
	YVO_4	200	400	570	-	5,1	-
+75	KGW	200	400	570	1810	18,67	68,38
	Diamond	320	900	600	1750	63,4	85,8
	$CaWO_4$	460	800	530	1670	25,2	114
	YAG	700	950	500	1220	32,86	171,63
	Y_2O_3 ceramics	360	390	550	1150	13,78	52,88
	Lu_2O_3	550	750	550	1280	26,84	89,75
+100	KGW	240	500	560	1850	20,51	72
	Diamond	400	600	590	1800	44,7	55,6
	$CaWO_4$	470	800	525	1770	43,16	135,5
	YAG	870	950	500	1165	19,8	134,5
	Lu_2O_3	540	900	500	1340	25,71	92,88
+150	KGW	470	750	560	1950	17,45	55,25
	Diamond	690	950	570	1900	38,06	66,13
	$CaWO_4$	500	900	530	1900	45,1	141,38
	Lu_2O_3	950	950	520	1140	4,1	31,8

Results of SC generation thresholds measured with 50 mm and 75 mm focal distance lenses, which were used for focusing pump radiation, were

compared with the critical power of self-focusing, see Fig. 4.4. As the SC threshold is directly proportional to the critical power as shown in [198], we would expect a lower SC threshold for materials with lower self-focusing power. However, the tendency was not exactly as expected despite the quite good match with the experimental data of Raman nonactive crystals, as Raman active crystals (diamond and $CaWO_4$) indicated lower values. We think that the difference between the measured and calculated value is due to the change of the nonlinear refractive index within the material, when the femtosecond laser pulse starts the SRS process and which resonantly contributes to n_2 as shown in [228]. By comparing the experimental data of those crystals with the theoretical curve of P_{Cr}, we can calculate the predicted change of the nonlinear refractive index. In order to match the theoretical curve, the n_2 should be ~2.5 and ~1.6 times higher for the diamond and $CaWO_4$ crystals respectively.

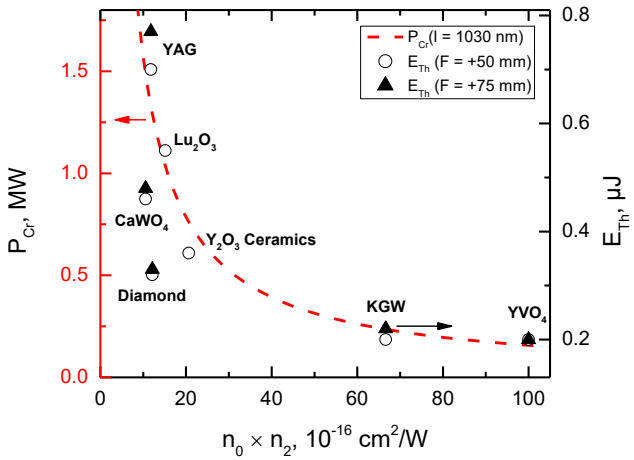

Fig. 4.4. Calculated critical power for self-focusing (*red dotted line*) and measured threshold energy for SC generation, using 50 mm (*squares*) and 75 mm (*triangles*) focal distance lenses for investigated materials.

The largest SC blue side spectral broadening of 480 and 500 nm (Fig. 4.5(a)) was achieved in YAG crystal at 950 nJ pump energy focused by using a 50 mm focal length lens and with Lu_2O_3 crystal at 900 nJ by using a 100 mm lens. The results corresponded well with the high bandgap of the materials, which is the limiting factor for the maximal cutoff position. Meanwhile, the longest wavelength at the red side of SC (~1900-1950 nm) (Fig. 4.5(b)) was achieved in KGW crystal at 750 nJ pump, diamond crystal at 950 nJ pump, and $CaWO_4$ crystal at 950 nJ pump, using the same focusing

conditions (150 mm lens). It can be noticed from the experimental data, that by focusing with longer focal length lens generated SC spectrum was broader in the IR region. For example, the SC spectrum in KGW and diamond crystal extended up to 1700 nm when the pump was focused by 50 mm lens, and up to 1900 nm when the pump was focused by 150 mm lens. However, the SC generation threshold increased more than 2 times from 220 nJ to 470 nJ for KGW, and from 330 nJ to 690 nJ for diamond. There was no clear dependency on focusing conditions of cutoff position on the blue side (Vis-NIR) of the SC spectrum. These results could be explained by the space-coupling effect. When the SC is generated, the intense ultrashort pulse is strongly reshaped and splitting into two, leading and trailing sub-pulses which are responsible for red-shifted and blue-shifted spectral broadening respectively [229]. It was shown by V. Jukna et al. [230], that loose focusing conditions enhanced spectral broadening to longer wavelength due to the increased nonlinear propagation of the leading sub-pulse, meanwhile trailing pulse is not affected, therefore, the blue side of the SC remains fairly constant.

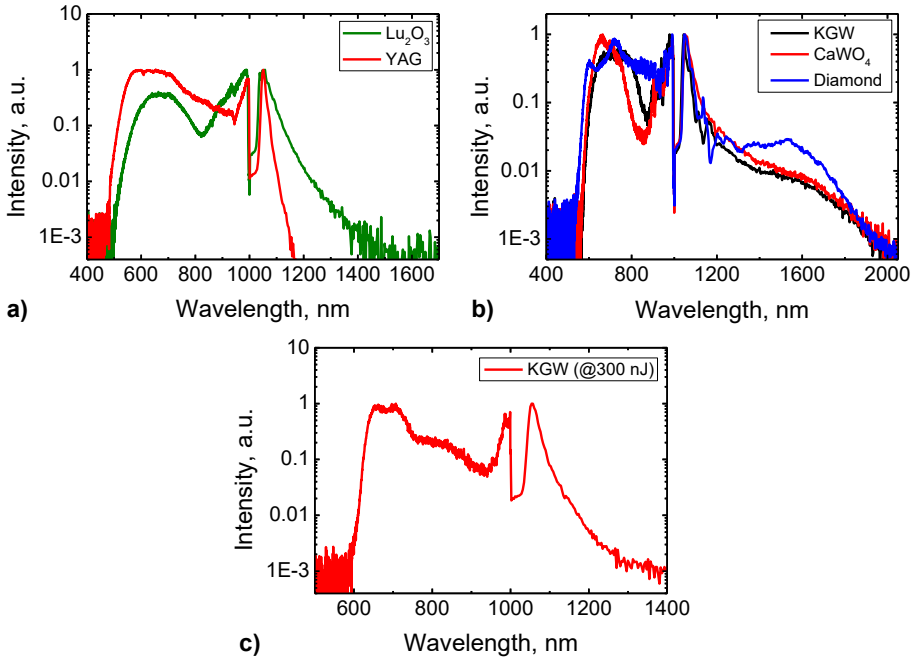

Fig. 4.5. a) Spectra of the SC generated in 5 mm length Lu_2O_3 and YAG crystals in which the largest blue side spectral broadening was achieved. **b)** Spectra of the SC generated in 5 mm length KGW, 6 mm length diamond, and 13 mm length $CaWO_4$ crystals in which the largest SC red side broadening was achieved. **c)** Spectra of the SC generated in 5 mm length KGW at pump energy level used for SRA experiment.

Our goal was to find optimum seed pulse generation conditions for low-energy femtosecond lasers, running at MHz repetition rates. Due to the pump energy limitation, we intended to distinguish materials suitable for the SC generation and pump conditions that require the lowest possibly pump radiation energy for stable and sufficient SC spectrum generation for subsequent amplification. The best choice for Vis-NIR spectrum amplification was YVO_4 for which the SC threshold using 50 mm lens was around 200 nJ and for the IR part, it was KGW crystal for which the SC threshold using the 75 mm lens was similar to YVO_4. Since we aimed for the SRA wavelength conversion approach the following experiment was performed with KGW crystal. The SC spectrum obtained at the pump level used for the experiment is presented in Fig. 4.5(c).

4.2.2. Stimulated Raman Amplification

Schematic representation of the SRA experiment is shown in Fig. 4.6. The layout was optimized for the first-order Stokes wave amplification. Diamond crystal was chosen as an amplifier active medium, as it featured the largest Stokes shift of 1332 cm^{-1}, which produced 1194 nm Stokes wavelength at 1030 nm pump. KGW crystal was chosen for the seed generation due to its lowest SC generation threshold compared with the other investigated materials. 300 mW of the pump focused by 75 mm lens (L2) was used for SC generation in KGW crystal (C1). The SC radiation (Fig. 4.5(c)) was separated from the pump with a dichroic mirror (DM1) and additionally filtered by using a 1050 nm long-pass filter (F1). Dichroic mirror coating with a high reflection coefficient in the first-order Stokes spectral region (HR@1194 nm) was selected. Moreover, both the pump and the higher-order Stokes spectral regions were successfully transmitted (HT@1030+ 1419 nm). Seed and remaining pump radiation were combined in a diamond crystal (C2) using the second dichroic mirror (DM2), while the delay between pulses was controlled by translating roof mirror (RM) on a precise positioning stage. The amplified signal was separated from the pump with a long-pass 1100 nm filter (F2) and the output spectrum was registered using an Ocean Optics NIRQuest spectrometer (S). Due to limitations of the optical scheme at higher pump energies, SC generation appears in the diamond crystal at the amplification stage and that disrupts results. Total pump power from FemtoLux 3 laser was intentionally limited from a maximum of 3 W to 1.5 W to prevent SC influence on amplification results.

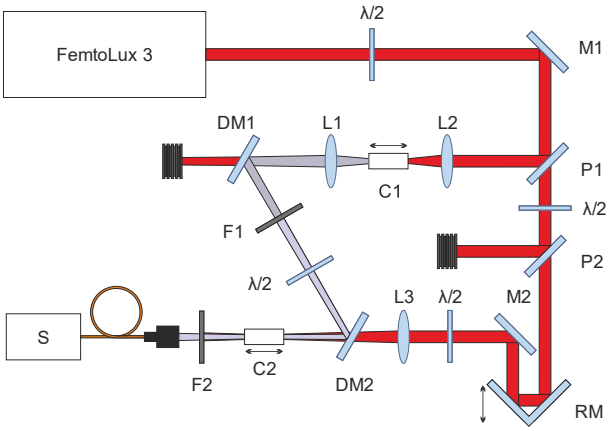

Fig. 4.6. Experimental setup of Raman amplification. Where λ/2 – half-wave plate, M(1-2) – mirror, P(1-2) – polarizer, DM(1-2) – dichroic mirror, C(1-2) – crystal, RM – roof mirror, L(1-3) – lens, F(1-2) – filter, S – spectrometer.

The measurements were made at different pump levels. The change in the output power is presented in Fig. 4.7(a). At the remaining maximum pump power of 1.1 W measured output power was around 130 mW, which corresponded to around 11.3% of conversion efficiency (gain of 25 times) in 6 mm length diamond crystal and about 9% of total conversion efficiency, including part of the pump used for seed generation, and around 100 mW loses due to reflections and absorptions in the optical path.

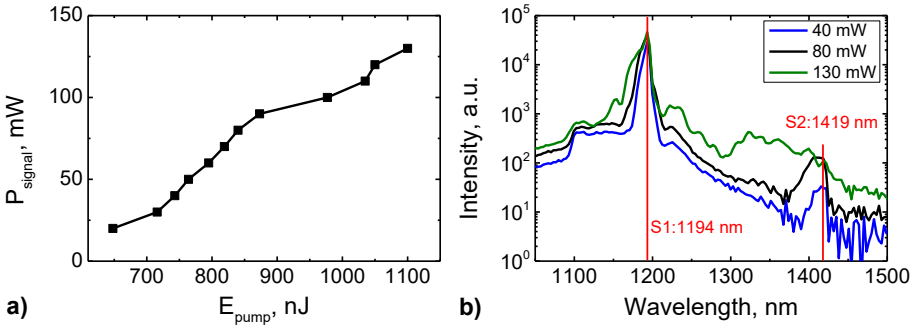

Fig. 4.7. Experimental results of Raman amplification. **a)** Measured amplified signal power versus pump power. **b)** Measured signal spectrum at different output power.

Measured spectra (Fig. 4.7(b)) clearly show the first-order Stokes wave amplification at around 1194 nm. However, despite the seed signal filtering by using a dichroic mirror, some signal of the second-order Stokes was observed at ~1419 nm. The second-order Stokes radiation was probably generated due to sufficient energy of the first-order Stokes wave, which performed as a new pump inside the crystal. The positions of peak centers

corresponding to Raman amplification manifested a tendency to broaden in the shorter wavelengths direction when pump power was increased. Furthermore, the spectrum of the amplified Stokes wave was accompanied by weak SC generation at higher pump energies. The tendency of Stokes wavelength shift could be explained as by "hot" lattice (heat up to several hundred degrees K [231,232]) due to intense pump-crystal interaction, as well by nonlinear spectrum broadening. As it was demonstrated previously by P. Mackonis et.al.[179], amplified in SRA and spectrally broadened pulses are compressible. The broadened spectrum in the case of 130 mW output power corresponded to transform-limited pulses of ~100 fs. It was interesting, that during SRA the seed SC radiation was amplified in a much wider spectral range than the resonant wavelength. Unfortunately, we have no reasonable explanation for that effect. The amplified Stokes pulses may generate the SC radiation. If that would be the case, compressible spectrum could be even broader resulting in shorter than 100 fs pulses. This phenomenon, however, requires more investigations.

4.2.3. A concept of the mid-IR laser source based on synchronous pumping and SRA.

The synchronous pumping of SRA allows to significantly increase efficiency. The main disadvantage of currently demonstrated solutions is the large length of the ring cavity. A new approach that solves the mentioned problem was presented by X. Gao et al. in [233]. The linear two-mirror cavity was pumped with 1.25 GHz burst packets at a repetition rate of 1 kHz. That allowed to reduce cavity length down to ~24 cm. However, the pump laser was operating at 532 nm wavelength and the pulse duration was ~30 ps. Furthermore, the number of pulses in the burst was limited up to 6. Due to the long pulse duration and short pump wavelength, this solution is not optimal for biological microscopy.

By combining synchronous pumping of Yb-doped fiber laser which provides burst packets with ultra-high (~1 GHz) pulse repetition rate [A7] and SC seeded SRA approach, the compact and robust laser for nonlinear biological microscopy can be constructed. The full detailed description of this invention is presented in the patent application P1. In this section, the main focus is dedicated to the optimized configuration for a first Stokes wave.

The block diagram of the modified FemtoLux 3 laser is presented in Fig. 4.8(a). The pulses from the oscillator are amplified and stretched,

afterward directed into the GHz burst generator stage. Therein, via the active fiber loop technique, the burst of a selected number of pulses are generated with the desired amplitude and designed period T1 between them. A detailed description of the operation of this technique and possible configurations is presented in article A7. After the burst formation, the pulses are amplified in a fiber amplifier up to ~3 W and then compressed with the free space grating compressor down to <300 fs. The advantage of this burst formation addon in laser is that the desired number of pulses can be selected and the maximal repetition rate of the packets is equal to the lasers oscillator repetition rate divided by the number of pulses in the burst. The repetition rate of the 10 pulses packet in modified FemtoLux 3 laser can be up to 5 MHz.

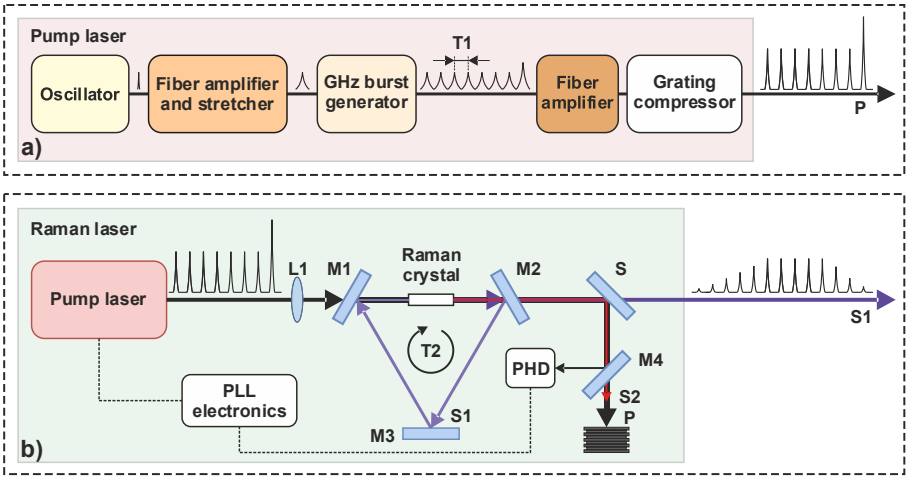

Fig. 4.8. a) Block diagram of the pump laser. **b)** The layout of synchronously pumped self-seeded Raman laser. Where L1 – lens, T1 – the period between the pulses in the burst, T2 – round trip time in the loop, M(1-4) – mirror, S – wavelength separator, PHD – photodiode, PLL – phase-locked loop, P – pump wave, S1 – first Stokes wave, S2 – second Stokes wave.

The layout of the Raman laser source concept is presented in Fig. 4.8(b). The burst of pulses from the pump laser is directed to the ring cavity consisting of 3 mirrors. The Raman active material is placed in the cavity between two mirrors. For further analysis, a 6 mm CVD diamond crystal is selected. The diamond is specifically chosen due to its high thermal conductivity (Table 4.1). Three mirror configuration is selected due to the following advantage: optical design protects pump laser from back-reflected radiation and generated pulse passes Raman crystal only one time per roundtrip, therefore linear and nonlinear losses are avoided. In principle, if a very compact design is required, the two-mirror linear cavity can be constructed.

The mirrors M1-M3 of the cavity are coated to highly transmit pump radiation at 1030 nm. Diamond Raman shift is equal to 1332 cm^{-1}, therefore the first Stokes for the selected pump is at ~1194 nm and the second Stokes is at ~1420 nm. This design is optimized for the first Stokes wave, hence all mirrors are designed to be transparent for 1420 nm as well. Mirrors M1 and M3 inner sides directed into a cavity are highly reflective at 1194 nm. Mirror M2 inner side is partly transmittant (≤20 %) at 1194 nm to realize output, meanwhile, the reflected part circulates in the cavity and is used as a seed for further pump pulses. The pump radiation is focused by the lens L1. A cavity caustic can be formed with the use of spherical mirrors M1-M3 or with additional lenses in the cavity (which are not shown in the layout). The first Stokes wave at the output is separated from the pump and the second stokes wave with separator, which directs undesired radiation to the beam dump.

The round trip time T2 is close to the period of pulses in burst T1 to realize synchronous pump condition. The SRS process has a delayed response, therefore for the maximal amplification T2 has to be a little bit shorter than T1.

Numerical simulations were performed with a 6 mm length diamond crystal pumped with a burst of 300 nJ pulses with an intraburst repetition rate of 1 GHz and duration of 250 fs. The conversion efficiency dependency on the number of pulses in the burst at 90% reflectance mirror M2 is presented in Fig. 4.9(a). Simulations revealed, that at selected pump pulse energies the SRA starting from quantum noise level is very ineffective with first pulses, therefore approximately 10 pulses in the burst are required to initiate effective amplification. In section 4.2.2 we demonstrated an effective SC seeded SRA approach, that allowed us to reach up to 9% conversion efficiency in a single-pass configuration. The same idea was applied in this setup.

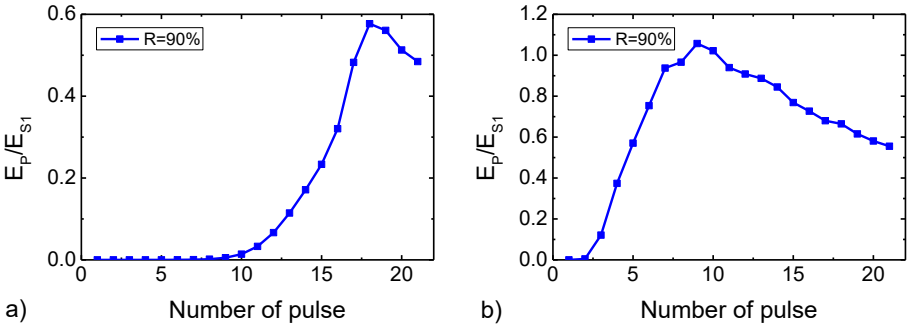

Fig. 4.9. First Stokes wave energy dependency on a pump pulse number at 90% reflectance mirror M2 in case of no seed (a) and with initial seed (b).

The standard approach for SC generation requires an additional stage, which increases system size, complexity and reduces long-term stability. Due to this, a different compact approach was proposed. Since the GHz burst generator addon allows to modulate the amplitude of the pump laser pulses, a custom form burst was selected. The first pulse energy was selected to be sufficiently high to generate a broad enough SC spectrum in the diamond crystal, meanwhile, subsequent pulses energies were lower than the SC generation threshold. In this case, the seed is generated in the same Raman active crystal, therefore the system complexity and size are not affected. Simulations of the proposed SC seeded amplifier were performed (Fig. 4.9(b)). Results confirmed, that in such a case, the efficient amplification starts after the first pulse and saturation is reached at less than 10 pulses. Furthermore, the energy at saturation is around two times higher than in a case with no seed. Another advantage of this approach is that due to strong SRS amplification starting from the second pulse the Stokes pulse duration shortening begins as well, which is desirable for microscopy applications.

To ensure a synchronous pump, the cavity length has to be precisely controlled. The most common solution is based on a piezo stage which adjusts one of the cavity mirrors. The stage is usually realized with the feedback control to compensate for environmental perturbations. Due to mechanical or thermal perturbations, the roundtrip time T2 or period of pump pulses T1 can change, therefore, it has to be compensated. However, the piezo-stage-based feedback solution increases system complexity and reduces reliability as was described in section 3.1.2. Another method to fulfill synchronous pump conditions is to control period T1 of pump pulses. The described GHz burst generation module allows the integration of the all-fiber repetition rate control technique presented in section 3.2. This approach does not require an additional component in the cavity, only the partially reflective mirror M4 before the beam dump is required to direct measured signal to the photodiode, therefore it is a robust and compact solution.

Even though the fully functional system was not yet assembled and tested, the required components and technologies were analyzed separately and thus demonstrated desirable parameters. The known behavior of the consisting elements and simulation results of the final system allow us to predict high-performance operation. To sum up, our proposed laser source concept appears to be a very promising compact and reliable solution dedicated to nonlinear biological microscopy systems.

4.2.4. Summary of the results

In this work, experimental tests of SC generation in the commonly used and several rarely tested crystals were presented. Fast degradation of Y_2O_3 crystal and ceramics was observed, meaning that the number of defects influencing a decreased damage threshold makes these materials unsuitable for practical applications with the examined pump conditions. Raman-active crystals (KGW, Diamond, $CaWO_4$) manifested good results in the generation of SC spreading to the NIR spectrum range. With the limited pump energy of 1 μJ, NIR cutoff of at 1900-1950 nm wavelength was demonstrated. Meanwhile, non-active in the SRS crystals: YAG, Y_2O_3, Lu_2O_3, manifested better shifting of the pump wavelength to Vis-NIR spectrum part of the SC, with obtained cutoff wavelength as short as 480-500 nm. In our experiments, some Raman active crystals featured lower SC generation thresholds than could be expected from the evaluation of the critical power of self-focusing. It could be an indication of an increase of efficient nonlinear refractive index due to Raman resonance. Observed low threshold of SC generation in Raman active crystals makes them the materials of choice in low energy applications.

Moreover, an experimental setup of femtosecond source in the NIR region was demonstrated. SRA scheme seeded by SC generated in KGW crystal and subsequently amplified in Diamond crystal produced up to 130 mW output power at discrete 1194 nm wavelength with nearly 9% of total conversion efficiency.

Moderate output power femtosecond lasers generating a few Watts of average power and a few micro-Joules of pulse energy could be efficiently wavelength shifted using the SC amplification approach. We have presented the way to make a cheap and simple laser source with a fixed or tunable wavelength by carefully choosing a pump laser energy in SC generation and subsequent nonlinear amplification layout.

Finally, a concept of the laser source dedicated to nonlinear biological microscopy applications was presented. This approach combines synchronous pumping with developed and tested technologies which are described in this thesis, [A7] and the patent application P1. According to the test results of each technology and numerical simulation, this laser source concept is a promising, robust, compact, and efficient solution for the NIR region.

CONCLUSIONS

1. Combination of two-channel fiber seed laser with subsequent amplification in narrowband picosecond Nd:YVO_4 regenerative amplifier and in multiple mid-IR OPA stage where efficient low-energy SC radiation pre-amplification in BBO crystal is employed, allows to realize hybrid broadband (up to 550 cm^{-1} and up to 850 cm^{-1} bandwidth by using the crystal scanning technique) high resolution (<3 cm^{-1}) SFG spectrometer system, that is tunable in the spectral range from 2 μm to 10 μm.
2. Feedback loop incorporation in an Er-doped fiber phase shifter setup allows increasing frequency response speed of 100 times. Furthermore, this could be increased even more with a higher pump offset, but it requires suppressing delay instabilities, arising due to the increased thermal load.
3. A combination of a low total cavity dispersion (-0.27 ps^2) fiber oscillator and an Er-doped fiber phase shifter allows realizing a frequency-locked mode-locked fiber oscillator operating at 1030 nm wavelength, which exhibits stable locking of pulse repetition rate to an external RF source with a timing jitter below 200 fs.
4. Supercontinuum seeded stimulated Raman active crystal amplifier setup allows realizing compact and efficient μJ-level femtosecond 1 μm laser wavelength conversion to biological tissues transparent NIR region (1.1-1.35 μm). Furthermore, supercontinuum self-seeded stimulated Raman amplification scheme combined with GHz burst providing fiber-based pump source, synchronous pumping, and all-fiber repetition rate locking techniques paves a way for improved efficiency, compact, and robust wavelength conversion concept.

SANTRAUKA

Įžanga

Nuo lazerių eros pradžios 1960-aisiais [1] per daugiau nei 60 metų lazerių technologijos drastiškai ištobulėjo. Šiuo metu lazeriai ar jų sistemos naudojami daugybėje sričių, jie pritaikomi ne tik moksliniuose centruose ar laboratorijose, bet ir pramonėje, fabrikuose ir net medicinoje. Tobulėjant technologijoms ir papildant lazerius naujomis funkcijomis, taip pagerinant jų parametrus, atsiranda vis daugiau sričių, kur juos galima pritaikyti.

Vidurio infraraudonosios srities (vid-IR) lazerinių šaltinių technologijos amžius beveik toks pat kaip ir pirmojo lazerio. Įdomus faktas yra tai, kad po Maimano rubino lazerio [2], antrasis lazerinis šaltinis pasaulyje buvo vidurio infraraudonosios srities uranu legiruoto kalcio fluorido kietakūnis lazeris, kurio centrinis bangos ilgis buvo 2.49 μm, o pagamintas jis buvo tais pačiais 1960-aisiais. Vidurio infraraudonosios srities šaltinių poreikis spektroskopijai dešimtmečius skatino tradicinių lazerių tobulinimą, kurie įprastai dirbo nuolatinės ar ns impulsinės veikos režime. Plačiajuosčių osciliatorių (Ti:Safyro, Cr:LiSAF, Aleksandrito) bei jų stiprintuvų sukūrimas ankstyvaisiais 90-taisiais inicijavo naujos femtosekundinių technologijų srities matomojoje spektro dalyje atsiradimą. Plačiajuosčiai lazeriniai šaltiniai kartu su naujai sukurtais didelio antros eilės netiesiškumo kristalais [3] leido pasiekti didelio efektyvumo optinį parametrinį stiprinimą (*angl. trump.: OPA*). Femtosekundinių impulsų parametrinio stiprinimo bei dažnio keitimo technologijos netrukus buvo pritaikytos artimosios infraraudonosios srities (*angl. trump.: NIR*) bei vid-IR šaltinių kūrimui.

Viena iš sričių, kur ultratrumpųjų vid-IR impulsų šaltiniai itin paklausūs yra suminio dažnio generacijos (*angl. trump.: SFG*) vibracinė spektroskopija. Ji yra paremta rezonansiniu netiesiniu derinamo vid-IR šaltinio bei matomosios srities šaltinio impulsų maišymu [4]. Dėl nagrinėjamų paviršiaus molekulių aktyvių vibracinių modų suminio dažnio signale registruojama rezonansinio atsako dedamoji. Ši technologija plačiai pritaikoma daugybėje sričių [5], tokių kaip: molekulių orientacijų, paviršiaus struktūros, cheminės sudėties ir epitaksinio auginimo elektrochemijos tyrimuose, skysčių, kietųjų medžiagų, polimerų, biologinių membranų bei kitų sistemų sandūrų ir paviršių tyrimuose. Plačiajuosčiai femtosekundiniai derinamo bangos ilgio vid-IR šaltiniai pagaminti panaudojant Ti:Safyro osciliatorius leido sukurti spektrometrus, kurie gali užregistruoti visą nagrinėjamo bandinio spektrą išvengiant bangos ilgio skenavimo [6]. Deja, tokiose sistemose spektrinė

skyra yra ribojama dėl matomojo kanalo juostos pločio. Ši problema dažniausiai sprendžiama siaurinant matomojo kanalo spektrą arba panaudojant du atskirus lazerinius šaltinius, tačiau pirmuoju atveju patiriami didžiuliai energijos nuostoliai, o antruoju atveju reikalingas itin sudėtingas lazerių sinchronizavimas.

Ultratrumpieji NIR šaltiniai buvo pritaikyti netiesinėje mikroskopijoje. NIR šaltiniai yra ypatingai patrauklūs bei reikalingi biologinių bandinių mikroskopijai, kadangi audiniai turi skaidrumo langus šioje srityje. Pirmieji femtosekundiniai NIR šaltiniai buvo sukurti naudojant Ti:Safyro osciliatorius bei OPA pakopas, jie buvo optimizuoti didelei energijai (nuo dešimčių μJ iki kelių mJ) ir mažam pasikartojimo dažniui (nuo kelių iki kelių šimtų kHz). Tuo tarpu mikroskopijai reikia didelio dažnio (MHz lygio) ir sąlyginai mažos (μJ lygio) energijos, kad būtų realizuotas greitas registravimas, didelis signalo-triukšmo santykis bei būtų išvengta bandinio pažaidos. Atsiradus iterbio jonais legiruota terpe paremtiems skaiduliniams ir kietakūniams fetosekundiniams lazeriniams šaltiniams buvo sukurti NIR šaltiniai tinkamesni mikroskopijai [7], tačiau OPA paremtos schemos dažniausiai buvo gana sudėtingos, todėl kompaktiškesnių bei patikimesnių schemų poreikis išliko. Kadangi netiesinei mikroskopijai dažniausiai nereikia derinamo bangos ilgio šaltinio, gali būti pritaikomi paprastesni diskretinio bangos ilgio keitimo metodai. Vienas iš jų, kuris buvo sėkmingai pademonstruotas yra stimuliuota Ramano sklaida [8]. Kadangi femtosekundiniams impulsams keitimo efektyvumas yra mažas, šiuo atveju naudotoje vieno praėjimo schemoje buvo pasiekti vos keli procentai. Kelių pakopų panaudojimas gali padidinti efektyvumą, tačiau tuomet sistema neišvengiamai tampa sudėtingesnė ir mažiau patikima. Kitas pasiūlytas sprendimas padidinti efektyvumą buvo paremtas sinchroniniu kaupinimu [9]. Šiuo atveju naudojama tik viena pakopa, tačiau net naudojant 80 MHz kaupinimo šaltinį reikia beveik 4 m ilgio rezonatoriaus. Dideli matmenys daro įtaką ilgalaikiam stabilumui bei apsunkina lazerio integravimą.

Šio darbo tikslas buvo sukurti lazerinius šaltinius SFG spektroskopijai bei netiesinei mikroskopijai, tokius, kurie neturi minėtų dabar naudojamų sistemų problemų, yra kompaktiškesni, patikimesni ir labiau prieinami.

Pirmiausia buvo koncentruotasi į hibridinio optiškai sinchronizuoto SFG spektrometro kūrimą. Buvo pradėta nuo optiškai sinchronizuoto dviejų kanalų osciliatoriaus, kuris buvo naudojamas kaip užkratas abiem spektrometro kanalams. Ypatingas dėmesys buvo skirtas plačiai derinamam plačiajuosčiam vid-IR kanalui. Atlikus skaitmeninius modeliavimus buvo parinkta tinkamiausia ir efektyviausia OPA schema. SFG spektrometras buvo

eksperimentiškai realizuotas ir charakterizuotas panaudojant kelis žinomus bandinius. Kaip alternatyva optiškai sinchronizuotai hibridinei SFG sistemai buvo atliktas tyrimas siekiant sukurti parastą pasikartojimo dažnio pririšimo metodą, skirtą siaurajuosčio kanalo lazerio osciliatoriui. Puslaidininkiniu įsisotinančio sugėriklio veidrodžiu (*angl. trump.: SESAM*) paremto sinchronizuotų modų skaidulinio osciliatoriaus su skirtingomis rezonatoriaus dispersijomis fazinio triukšmo analizė bei visiškai skaidulinių fazės valdiklių tyrimai leido parinkti optimalią konfigūraciją. Surinkta informacija buvo panaudota realizuojant sinchronizuotą osciliatorių.

Kitas šio darbo siekis buvo sukurti paprastą ir patikimą iterbio jonais legiruota terpe paremto didelio dažnio lazerinio šaltinio bangos ilgio keitimo į NIR spektrinę sritį, kur yra audinių skaidrumo langai, metodą. Superkontinuumo (*angl. trump.: SC*) generacijos eksperimentinių tyrimų, naudojant mažą kaupinimo energiją, rezultatai, bei jų analizė buvo panaudota kuriant vieno praėjimo SC užkrėsto stimuliuoto Ramano stiprinimo (*angl. trump.: SRA*) schemą. Siekiant dar labiau padidinti konversijos efektyvumą, sinchroninio kaupinimo sprendimai buvo išnagrinėti. Atsiradus naujiems MHz pasikartojimo dažnio kaupinimo lazeriniams šaltiniams, kurie panaudoja naujovišką skaidulinį GHz vorų formavimo metodą, trumpo rezonatoriaus ilgio sinchroninio kaupinimo schemos tapo įmanomos. Sukaupta informacija superkontinuumo generavimo ir SRA eksperimentų metu, kartu su sinchroninio kaupinimo sprendimu ir osciliatoriaus pasikartojimo dažnio valdymo metodu, buvo panaudota siekiant sukurti efektyvaus, patikimo ir kompaktiško femtosekundinio NIR šaltinio, skirto netiesiniai mikroskopijai, koncepciją.

Darbo tikslas ir uždaviniai

Pagrindinis darbo tikslas buvo sukurti metodus ir technologijas, leidžiančias realizuoti efektyvius ir patikimus lazerinius šaltinius NIR ir vid-IR spektriniame diapazone, kurie yra skirti mikroskopijai ir SFG spektrometrų sistemoms. Siekiant įgyvendinti tikslą buvo atliktos šios užduotys:

1. Sukurtas plačiajuostis derinamo bangos ilgio femtosekundinis vid-IR lazerinis šaltinis skirtas SFG spektrometrijai, bei pademonstruota pilnai funkcionali optiškai sinchronizuota hibridinė SFG spektrometro schema.
2. Ištirti ultrasparčiųjų iterbio jonais legiruota terpe paremtų SESAM sinchronizuotų modų osciliatorių su skirtingomis rezonatoriaus

dispersijomis laisvos eigos faziniai triukšmai, siekiant nustatyti optimalią konfigūraciją mažo laikinio drebėjimo dažnio pririšimui.

3. Ištestuoti ir optimizuoti visiškai skaiduliniai fazės valdikliai, kurie yra skirti integravimui į stabilizuojamo pasikartojimo dažnio osciliatorius. Realizuotas osciliatoriaus dažnio pririšimas prie išorinio elektrinio šaltinio ir charakterizuota surinkta sistema.

4. Ištirta ir optimizuota superkontinuumo generacija įvairiuose kristaluose su mažos energijos kaupinimo (<1μJ) impulsais, esant 1 MHz pasikartojimo dažniui, siekiant pastumti iterbio jonais legiruota terpe paremtų lazerinių šaltinių bangos ilgį į biologinių audinių skaidrumo sritį.

5. Ištirti iterbio jonais legiruota terpe paremtų lazerinių šaltinių bangos ilgio keitimo į NIR spektrinį diapazoną metodai, kurie paremti superkontinuumu užkrėsto stimuliuoto Ramano stiprintuvo schema ir yra skirti kompaktiško, patikimo ir efektyvaus šaltinio netiesinei mikroskopijai realizavimui.

Mokslinis naujumas

Pagrindinis darbo tikslas buvo sukurti metodus ir technologijas, leidžiančias realizuoti efektyvius ir patikimus lazerinius šaltinius NIR ir vid-IR spektriniuose diapazonuose, kurie yra skirti mikroskopijai bei SFG spektrometrų sistemoms.

Šio darbo mokslinis naujumas slypi sėkmingai pademonstruotose kietakūnėse ir skaidulinėse technologijose, kurios leido realizuoti hibridinę vid-IR SFG spektrometro sistemą, sinchronizuotą skaidulinį osciliatorių ir efektyvų NIR lazerinį šaltinį:

1. Pasiūlyta ir eksperimentiškai pademonstruota naujoviška optiškai sinchronizuoto aukštos rezoliucijos plačiajuosčio derinamo vid-IR suminio dažnio generacijos spektrometro schema, paremta visiškai skaiduliniu dviejų kanalų osciliatoriaus užkrato šaltiniu, kuris panaudotas plačiajuosčių ir siaurajuosčių impulsų generavimui. Šis išpildymas eliminuoja dviejų lazerių sinchronizavimo ar labai neefektyvaus spektrinio siaurinimo reikiamybę, todėl itin supaprastina sistemą.

2. Eksperimentiškai pademonstruotas ir išnagrinėtas būdas, kaip padidinti lūžio rodiklio modifikavimu paremto erbio jonais legiruotos skaidulos

fazės valdiklio atsako greitį, panaudojant grįžtamojo ryšio kilpą, kuri pakeičia sužadintų atomų efektinę gyvavimo trukmę.

3. Kompaktiškas stabilizuojamo pasikartojimo dažnio ultratrumpųjų impulsų iterbio jonais legiruota terpe paremtas SESAM sinchronizuotų modų skaidulinis osciliatorius buvo realizuotas remiantis patikimu visiškai skaiduliniu erbio jonais legiruotos skaidulos fazės valdikliu. Tai buvo pirmasis tokios pririšimo prie išorinio elektrinio šaltinio technologijos pademonstravimas iterbio jonais legiruota terpe paremto SESAM sinchronizuotų modų skaiduliniame osciliatoriuje.

4. Pademonstruota mažos energijos femtosekundinio iterbio jonais legiruota terpe paremto skaidulinio lazerio, kurio pasikartojimo dažnis 1 MHz, bangos ilgio keitimo į NIR sritį schema, kurioje panaudota superkontinuumu užkrėsto stimuliuoto Ramano stiprintuvo pakopa. Toks sprendimas sėkmingai pademonstruotas pirmą kartą. Šis technologinis sprendimas leido pasiekti didesnį keitimo efektyvumą ir realizuoti kompaktišką NIR šaltinį.

5. Naujoviška ir kompaktiška sinchroniškai kaupinamos stimuliuoto Ramano pagrindu paremtos bangos ilgio keitimo į NIR spektrinę sritį schemos koncepcija, paremta GHz voros kaupinimo lazeriu, savaime užsikrečiančiu Ramano stiprintuvo išpildymu bei visiškai skaiduliniu pasikartojimo dažnio pririšimo metodu, buvo sukurta ir teoriškai išnagrinėta.

Praktinė nauda

Bangos ilgio keitimo metodų tobulinimas bei naujų vystymas kartu su patikimų skaidulinių technologijų panaudojimu leidžia sukurti kompaktiškus, patikimus, efektyvius bei prieinamus ultratrumpųjų impulsų lazerinius šaltinius NIR ir vid-IR spektriniuose diapazonuose, kurie yra skirti spektroskopijos ir netiesinės mikroskopijos taikymams.

Šis darbas praktiškai vertingas keliais aspektais:

1. Nauja optiškai sinchronizuoto hibridinio plačiajuosčio aukštos spektrinės skyros vid-IR suminio dažnio generacijos spektrometro schema buvo eksperimentiškai pademonstruota. Sėkmingas išbandymas su keliais bandiniais paskatino jos integravimą į pilnai funkcionalią SFG sistemą, kuri šiuo metu yra paruošta prototipų kūrimui.

2. Mažos rezonatoriaus dispersijos skaidulinio osciliatoriaus bei visiškai skaidulinio erbio jonais legiruotos skaidulos fazės valdiklio kombinacija leido sukurti kompaktišką ir patikimą užkrato šaltinį, kuris gali būti integruotas į didelės energijos bei didelės galios lazerines sistemas ir leidžia pririšti jų pasikartojimo dažnį prie išorinio tikslaus šaltinio su mažu laikiniu drebėjimu. Komercinės sistemos, naudojančios minėtus užkrato šaltinius, jau realizuotos įmonėje „Ekspla“.

3. Sinchroninio kaupinimo, GHz voros kaupinimo lazerio, savaime užsikrečiančio Ramano stiprintuvo bei visiškai skaidulinio pasikartojimo dažnio pririšimo metodo technologijų tobulinimas bei panaudojimas leido sukurti patikimą, kompaktišką bei efektyvią femtosekundinio NIR spektrinio diapazono lazerinio šaltinio koncepciją, kuri gali būti pritaikyta komercinėse mažos energijos lazeriniuose šaltiniuose, skirtuose netiesinei mikroskopijai.

Ginamieji teiginiai

S1. Aukštos spektrinės skyros (<3 cm^{-1}), derinamo bangos ilgio (nuo 2 μm iki 10 μm) ir plačios dažnių juostos (iki 850 cm^{-1}) optiškai sinchronizuotas hibridinis suminio dažnio generacijos spektrometras gali būti realizuotas panaudojus dviejų kanalų skaidulinį užkrato šaltinį, kurio impulsai pastiprinti siaurajuosčiame pikosekundiniame Nd:YVO_4 regeneraciniame stiprintuve ir plačiajuosčiame daugiapakopiame vid-IR OPA, kuriame panaudotas efektyvus mažos energijos superkontinuumo užkrato parametrinis priešstiprintuvis BBO kristale.

S2. Lūžio rodiklio moduliacijos panaudojant lazerinio diodo spinduliuotę pagrindu paremto erbio (Er) jonais legiruotos skaidulos fazės valdiklio atsako greitis gali būti padidintas realizuojant grįžtamojo ryšio kilpą, kuri pakeičia efektinę sužadintų atomų gyvavimo trukmę. Tai leidžia panaudoti šį metodą pasikartojimo dažnio stabilizavimui su mažu laikiniu drebėjimu (standartinė deviacija <200 fs) kaip alternatyvą įprastiems pjezoelektriniams fazės valdikliams ultrasparčiuosiuose iterbio (Yb) jonais legiruota terpe paremtuose pasyviai sinchronizuotų modų skaiduliniuose osciliatoriuose.

S3. Kompaktiškas ir efektyvus metodas, skirtas μJ-lygio 1 μm femtosekundinio lazerio bangos ilgio keitimui į biologinių audinių skaidrumo sritį (1.1-1.35 μm) NIR regione gali būti realizuotas

panaudojus superkontinuumo spinduliuotės generaciją ir jos stiprinimą stimuliuotai Ramano sklaidai aktyviame kristale.

Autoriaus indėlis

Visus tyrimus pristatytus šiame darbe atliko autorius, išskyrus tuos, kurie nurodyti prie bendraautorių indėlio. Autorius sukonstravo arba prisidėjo prie konstravimo visų lazerinių sistemų, kurios aprašytos A1-A4 publikacijose. Autorius paruošė mokslinių publikacijų A1-A4 rankraščius. Taip pat, autorius atliko skaitmeninio modeliavimo ir teorinės analizės darbus, pateiktus mokslinėse publikacijose ir šiame darbe.

Bendraautorių indėlis

- Dr. Andrejus Michailovas vadovavo doktorantūros studijoms bei sudarė puikias sąlygas vykdyti tyrimus. Taip pat, pasiūlė svarbias idėjas darbams, pristatytiems mokslinėje publikacijoje A3, bei organizavo patentinės paraiškos P1 rengimą.
- Dr. Rokas Danilevičius generavo idėjas bei svariai prisidėjo prie mokslinių publikacijų A1 ir A2 rankraščių rengimo. Rokas konsultavo ir dalinosi eksperimentine patirtimi, kas padėjo pasiekti užsibrėžtus doktorantūros darbo tikslus.
- Dr. Karolis Viskontas prisidėjo konstruojant ir charakterizuojant skaidulinius lazerius aprašytus mokslinėje publikacijoje A2. Taip pat, jis ženkliai prisidėjo ruošiant mokslinės publikacijos rankraštį.
- Dr. Robertas Kananavičius sukonstravo spektrometro modulį bei padėjo realizuoti ir ištestuoti SFG spektrometro sistemą. Robertas taip pat dalinosi savo patirtimi bei įžvalgomis, kas padėjo parengti mokslinės publikacijos A1 rankraštį.
- Dr. Regimantas Januškevičius prisidėjo prie mokslinės publikacijos A1 rankraščio rengimo bei SFG spektrometro sistemos charakterizavimo.
- Rokas Jutas padėjo atlikti superkontinuumo generavimo bei SRA eksperimentus, kurių rezultatai pateikti mokslinėje publikacijoje A3.
- Dr. Tadas Bartulevičius sukūrė GHz voros lazerį, pristatytą patentinėje paraiškoje P1, bei dalinosi savo patirtimi ir konsultavo eksperimentinių schemų realizavimo klausimais.

- Virginija Petrauskienė atliko didžiąją dalį darbų rengiant patentinės paraiškos P1 aprašymą.
- Dr. Valdas Girdauskas atliko sinchroniškai kaupinamo SRA skaitmeninius modeliavimus.
- Dr. Pierre-Marc Dansette ir doktorantas Maksim Eremchev sukūrė ir išanalizavo NIR OPA schemą, kuri pristatyta mokslinėje publikacijoje A3.
- Dr. Audrius Zaukevičius ir doktorantas Laurynas Veselis patarė įvairiais klausimais, susijusiais su lazerių technologijomis, bei dalinosi savo patirtimi atliekant skaitmeninius modeliavimus ir eksperimentinius darbus.

Diskusija ir rezultatų apžvalga

Vid-IR suminio dažnio generacijos spektrometras

Skyriuje pateikta medžiaga publikuota A1 ir A4

Suminio dažnio generacijos spektroskopija yra galingas ir nedestruktyvus paviršių ir sandūrų charakterizavimo būdas [46]. Plačiajuostėse SFG spektroskopijos sistemose naudojami femtosekundiniai lazeriniai šaltiniai, kurių dėka vienu matavimu užregistruojamas visas spektras, tačiau spektrinė rezoliucija yra ribota ir siekia tik apie 10-20 cm^{-1} [6]. Norint apeiti fizikinius ribojimus ir pagerinti rezoliuciją yra naudojamos spektro siaurinimo technikos. Deja, tačiau jos yra itin neefektyvios ir dėl to patiriami didžiuliai energijos nuostoliai [58,59]. Kitas būdas kaip pasiekti viso spektro registravimą vienu matavimu ir užtikrinti gerą spektrine rezoliuciją, yra femtosekundinio ir pikosekundinio lazerio panaudojimas hibridinėje SFG spektroskopijos sistemoje [62,63]. Tokiose sistemose lazeriai turi būti tarpusavyje sinchronizuoti, kas nėra lengvai pasiekiama ir reikalauja sudėtingų technologinių sprendimų.

Šio darbo tikslas buvo sukurti kompaktišką ir pilnai funkcionalią sistemą, kuri yra efektyvi, nereikalauja sudėtingų ar nuostolingų technologijų spektrometro kanalų formavimui ar sinchronizavimui bei generuoja optimalius parametrus tiksliems ir greitiems vibracinės SFG spektrometrijos matavimams. Sistemos koncepcija buvo paremta daugiakanaliu pikosekundiniu skaiduliniu lazeriu [66,67], kuris panaudotas kaip tokios sistemos užkrato šaltinis. Vienas iš skaidulinio lazerio kanalų buvo

naudojamas užkrėsti didelės energijos pikosekundinį Nd:YVO_4 regeneracinį stiprintuvą, kurio išėjime siaurajuosčiai (~1.5 cm^{-1}) 1 kHz pasikartojimo dažnio impulsai, tuo tarpu kitas kanalas panaudotas generuoti plačiajuosčius vid-IR impulsus. Prieš pradedant vid-IR kanalo konstravimą, buvo atlikti detalūs skaitmeniniai modeliavimai, kuriais buvo siekiama nustatyti sąlygas, kuomet pasiekiamas maksimalus femtosekundinių impulsų konversijos efektyvumas į vid-IR spektrinį diapazoną su plačiausia įmanoma juosta.

Trys skirtingos vid-IR OPA schemos buvo išnagrinėtos. Modeliavimo rezultatai atskleidė, kad vid-IR OPA pakopa, kurioje panaudoti komerciškai prieinami netiesiniai kristalai, su 1 nJ superkontinuumo užkratu 1190 nm-1850 nm spektriniame diapazone, yra labai neefektyvi, o konversijos efektyvumas į šalutinę bangą išlaikant spektro plotį >500 cm^{-1} nesiekia net 0.001%. Vienintelė išimtis buvo GaSe kristalas, su kuriuo nustatytas konversijos efektyvumas buvo apie 100 kartų didesnis lyginant su likusiais kristalais, tačiau vis tiek per mažas, kad būtų galima realizuoti SFG spektrometrą. Buvo nustatyta, kad norint pasiekti pageidautiną išėjimo energiją paduodamo signalo energija tokio tipo OPA pakopoje turėtų būti mikro-Džaulio lygio. Dėl šios priežasties, kita nagrinėta schema buvo dviejų pakopų vid-IR OPA. Kadangi stiprinant superkontinuumo signalą keitimo efektyvumas itin prastas, net su visa galima kaupinimo energija iš lazerio, pirmos pakopos keitimo efektyvumas į signalinę bangą yra per mažas, kad būtų pasiektas reikiamas energijos lygis antros pakopos užkratui. Alternatyvus sprendimas pirmajai pakopai buvo išnagrinėtas. Šiuo atveju BBO OPA buvo užkrečiama ilgabange superkontinuumo puse (1150 nm-1850 nm), o kaupinama antra kaupinimo lazerio harmonika (532 nm). Teoriškai nustatytas keitimo efektyvumas buvo nuo ~0.6% iki ~5.5% nagrinėtame diapazone, kas atitinka kelis µJ, o tai apytiksliai 2-3 eilėmis daugiau nei prieš tai nagrinėtas vid-IR OPA variantas, kaupinamas su fundamentine lazerio spinduliuote (1064 nm). Rezultatai atskleidė, kad su tokiu užkratu šalutinės bangos energija po antrosios vid-IR OPA stiprinimo išlaikant 500 cm^{-1} spektro plotį 5-10 µm spektriniame diapazone siekia 1-3.4µJ, o ties 2.5 µm apytikriai 4.5-9.3 µJ. Šie parametrai tinkami plačiajuostės SFG spektrometro sistemos realizavimui, todėl tokia schema buvo pasirinkta tolimesniems eksperimentams.

Remiantis modeliavimų rezultatais buvo surinkta ir ištestuota eksperimentinė SFG spektrometro schema. Vid-IR pakopoje buvo išbandyti šie kristalai: 0.4 mm ilgio AGS, 0.5 mm ilgio GS ir 1mm ilgio LGS. Naudojant GS kristalą pavyko pasiekti šalutinės bangos derinimo ribas nuo 5 µm iki 13 µm, o naudojant AGS ir LGS kristalus derinimo ribas nuo 2 µm iki 10 µm. Didžiausia šalutinės bangos energija iki 0.4-1.8 µJ buvo pasiekta 2-5 µm

spektriniame diapazone naudojant AGS kristalą bei iki 0.2-0.5 μJ spektriniame diapazone nuo 5 iki 10 μm naudojant GS ir LGS kristalus. Derinimo ribose plačiausias spektro plotis pasiektas su LGS kristalu (205-505 cm^{-1}) bei su AGS kristalu (230-470 cm^{-1}). Eksperimentiniai rezultatai šiek tiek skyrėsi nuo teorinių. Nesutapimas greičiausiai kilo dėl neįvertintos dvifotonės sugerties kai kuriuose kristaluose, naudoto truputį mažesnio kaupinimo intensyvumo, neįskaitytų atspindžių nuostolių bei dėl neidealaus pluošto eksperimente.

Siekiant padidinti išėjimo energiją bei spektro plotį buvo išbandytas 1 mm ilgio AGS kristalas su kristalo skenavimo technika. Šalutinės bangos energija 2-5 μm diapazone padidėjo nuo 2 iki 4 kartų (iki 2,4-5,1 μJ), tuo tarpu 5-10 μm diapazone padidėjo apie 2 kartus (iki 0,2-1 μJ). Kristalo skenavimo technika 5-10 μm diapazone leido pasiekti panašų spektro plotį kaip ir su 0.4 mm ilgio AGS kristalu (apie 250-350 cm^{-1}), tuo tarpu 2-5 μm diapazone pasiektas efektinis spektro plotis buvo 500-750 cm^{-1}.

Pilnai funkcionali surinkta SFG spektrometro sistema buvo išbandyta. Nustatyta, kad pasiekta spektrinė rezoliucija <3 cm^{-1} ir matavimo ribos nuo 4000 cm^{-1} iki 950 cm^{-1}. Plačiajuosčio vid-IR kanalo energija buvo pakankama, kad realiu laiku būtų galima matuoti įvairius skysčius bei kietakūnius bandinius. Pavyzdžiui, su 0.1 s ekspozicijos trukme, etanolio spektras buvo registruojamas su priimtinu signalo-triukšmo lygiu. Kristalo skenavimo technika leido pasiekti daugiau nei 850 cm^{-1} registruojamą spektro plotį ties 2900 cm^{-1}, o matavimo laikui ji turėjo tik neženklią įtaką.

Skaidulinis osciliatorius su pasikartojimo dažnio pririšimu skirtas Ti:Safyro plačiajuostėms SFG spektroskopinėms sistemoms

Skyriuje pateikta medžiaga publikuota A2

Tiksli lazerio pasikartojimo dažnio kontrolė yra itin svarbi kai kuriems taikymams. Pavyzdžiui, didelio intensyvumo lazeriai dažnai paremti optiniu parametriniu čirpuotų impulsų stiprinimo technologija [149], reikalauja stabilaus ir tiksliai derinamo osciliatoriaus pasikartojimo dažnio, kad būtų įmanoma sinchronizuoti eksperimentinę įrangą. Kitas pavyzdys yra SFG spektrometrija, kur hibridinės SFG sistemos yra panaudojamos. Jos realizuojamos sinchronizuojant du atskirus lazerius (matomosios srities ir derinamas infraraudonosios srities), o laikinis dažnio drebėjimas turi būti mažesnis nei matomojo kanalo impulso trukmė [64]. Vienas iš dažniausiai sutinkamų sprendimų derinamam femtosekundiniam infraraudonajam kanalui

yra paremtas Ti:Safyro sistemomis, kurios yra paplitusios tyrimų laboratorijose. Tuo tarpu, siaurajuosčių matomojo kanalo pikosekundinių lazerių, kurie yra lengvai sinchronizuojami, poreikis yra didelis. Tiksliam pikosekundinės lazerinės sistemos sinchronizavimui osciliatoriaus dažnio drebėjimas kito lazerio ar tikslaus išorinio laikrodžio atžvilgiu turi būti femtosekundinėje laiko skalėje [150].

Paprastas, patikimas visiškai skaidulinis solitoninis sinchronizuotų modų lazeris yra vienas iš patraukliausių užkrato šaltinių minėtiems taikymams, tačiau impulsų formavimo mechanizmas jame yra sudėtingas ir dažnai sukelia papildomą pasikartojimo dažnio svyravimą prie jau esamo lėto terminio rezonatoriaus terpės ilgio kitimo. Bendras laikinis dažnio drebėjimas yra apsprendžiamas sąveikos tarp pastiprintos spontaninės emisijos, rezonatoriaus dispersijos ir netiesiškumo, solitonų energijos bei spektrinio filtravimo [151]. Dalis sukelto dažnio triukšmo gali būti efektyviai nuslopinta pasitelkus fazės derinimo kilpą (*angl. trump.: PLL*). Likusi triukšmo dalis už PLL juostos pločio prisideda prie bendro skaidulinio osciliatoriaus dažnio laikinio drebėjimo.

Panaudojus erbio jonais legiruotos skaidulos fazės reguliatorių, buvo sukurtas praktiškas pririšto pasikartojimo dažnio 1030 nm bangos ilgio osciliatoriaus dizainas. Panaudojus nedideles kaupinimo galias (14-28 mW) erbio jonais legiruotai skaidulai kaupinti pavyko pasiekti stabilų dažnio pririšimą prie išorinio elektrinio šaltinio su impulso laikiniu drebėjimu, mažesniu nei 200 fs.

Siekiant padidinti fazės valdiklio greitį, kuris ribojamas sužadintų jonų gyvavimo laiko, buvo ištirta ir pristatyta naujoviška koncepcija – erbio jonais legiruota skaidula su grįžtamojo ryšio kilpa. Kadangi panaudotas visiškai skaidulinis sprendimas, patikimumu jis nenusileidžia standartiniam. Tuo tarpu, atsako greitis išauga dėl pakitusios sužadintų jonų dinamikos ir, šiuo atveju, jis priklauso nuo stiprintuvo parametrų. Eksperimentiškai pavyko pasiekti ~100 kartų greičio padidėjimą lyginant su schema be grįžtamojo ryšio. Panaudojus didesnes kaupinimo galias, atsako greitis gali būti dar labiau padidintas, tačiau reikalingi papildomi tyrimai, kaip suvaldyti fazės poslinkio nestabilumus kilusius dėl nepageidaujamo terminio krūvio.

Skirtingų anomalių dispersijų skaidulinių osciliatorių laikinis dažnio drebėjimas buvo įvertintas. Rezultatai atskleidė, kad dažnių poslinkio ribose nuo 100 Hz iki 100 kHz, mažiausios nagrinėtos anomalios dispersijos (-0.05 ps^2) osciliatoriaus suintegruotas laikinis impulsų drebėjimas yra mažiau 150 fs. Tuo tarpu, didžiausios nagrinėtos anomalios dispersijos (-1.7ps^2) osciliatoriui padidėja iki 575 fs. Siekiant kompensuoti terminius ir kitus fazės

triukšmus mažesniame nei 100 Hz dažnio poslinkio diapazone bei išlaikyti visiškai skaidulinę osciliatoriaus konfigūraciją, erbio jonais legiruotos skaidulos fazės reguliatorius gali būti panaudotas kaip alternatyva kitoms vėlinimo linijoms, kai yra reikalingas mažesnis nei 1 ps laikinis impulso drebėjimas. Realizuojant hibridinę SFG sistemą pageidautina, kad laikinis impulsų drebėjimas tarp vid-IR femtosekundinio ir siaurajuosčio pikosekundinio impulsų būtų mažesnis nei dešimtadalis ps impulso trukmės. Tokiu būdu signalo fliuktuacijos dėl dažnio nestabilumo būtų minimizuotos. Siaurajuosčio lazerio, kurio spektriškai ribota impulsų trukmė yra 10 ps, spektro plotis atitinka ~1.5 cm^{-1}, taigi pademonstruotas metodas su <1 ps laikiniu drebėjimu tarp ps ir vid-IR impulsų yra tinkamas sprendimas plačiajuostės hibridinės SFG sistemos konstravimui.

Femtosekundinio NIR lazerinio šaltinio skirto netiesinės mikroskopijos taikymams kūrimas

Skyriuje pateikta medžiaga publikuota A3 bei aprašyta patentinėje paraiškoje P1

Viena iš sričių, kur femtosekundiniai NIR šaltiniai itin reikalingi, yra biologinių audinių netiesinė mikroskopija [160]. Biologiniuose audiniuose sugeneruoti netiesiniai signalai yra gana silpni, todėl norint pasiekti priimtiną signalo-triukšmo santykį reikalinga ilga bandinio ekspozicijos trukmė. Norint padidinti netiesinio signalo lygį, reikia kiek įmanoma trumpesnio signalo, o greitam signalo registravimui pageidautinas kuo didesnis pasikartojimo dažnis. Tuo pat metu yra leistina kaupinimo spinduliuotės galios riba, kurią lemia biologinių bandinių degradacija. Kitas netiesinės mikroskopijos aspektas yra kaupinimo ir netiesinio signalo bangos ilgių parinkimas. Įsiskverbimo gylis biologiniuose bandiniuose yra ribojamas šviesos sugerties [161]. NIR regione (0.7-2.5 μm) egzistuoja keli skaidrumo langai, kur audinių sugertis turi lokalius minimumus [161–166]. Norint optimizuoti įsiskverbimo gylį, reikia parinkti kaupinimo ir generuojamo signalo bangos ilgius taip, kad jie būtų skaidrumo languose.

Kadangi femtosekundinių lazerinių šaltinių NIR srityje pasirinkimas ribotas, norimiems parametrams pasiekti dažnai panaudojami netiesiniai bangos ilgio keitimo būdai. Vienas iš labiausiai paplitusių metodų, kaip gauti plačiajuostę femtosekundinę spinduliuotę, apimančią ultravioletinę, matomąją ir artimąją infraraudonąją sritį, yra superkontinuumo generacija [173,174]. Norint padidinti spektrinį tankį pasirinktame diapazone, dažnai

pritaikoma OPA technologija. Kadangi netiesinei mikroskopijai dažniausiai nereikia derinamo bangos ilgio šaltinių, paprastesni diskretiniai bangos ilgio keitimo metodai yra tinkami. Vienas iš jų yra stimuliuota Ramano sklaida paremtas stiprinimas (*angl. trump.: SRA*).

Kompaktiški, patikimi ir komerciškai prieinami lazeriniai šaltiniai, kurių impulsų energija 1-3 µJ, trukmė <500 fs, centrinis bangos ilgis 1-1.1 µm, pasikartojimo dažnis MHz eilės, o vidutinė galia 3-5 W, yra patrauklūs kandidatai kaip kaupinimo šaltiniai NIR lazerinėms sistemoms. Superkontinuumo spinduliuotė gali būti universalus užkrato šaltinis tiek OPA, tiek SRA paremtoms sistemoms, tačiau dėl gana mažos impulsų energijos tik nedidelė kaupinimo lazerio spinduliuotės dalis gali būti panaudota superkontinuumo generacijai, o likusi kuo didesnė dalis, pageidautina, netiesiniam stiprintuvui. Dėl šios priežasties reikalingi kristalai, kuriuose superkontinuumo generacijos slenkstis yra mažiausias.

Industrinis skaidulinis lazeris FemtoLux 3 (*Ekspla*) [186] buvo naudotas kaip kaupinimo šaltinis visiems eksperimentams. Jo išduodama spinduliuotės galia iki 3W esant 1 MHz pasikartojimo dažniui, impulsų trukmė <300 fs, o centrinis bangos ilgis 1030 nm. Lazeris jau buvo sėkmingai išbandytas plataus lauko antros harmonikos generacijos mikroskopijoje [187]. Siekiant praplėsti lazerio galimybes netiesinėje biologinių bandinių mikroskopijoje, bangos ilgio keitimo priedas, paremtas vieno lėkio SRA schema, kuri užkrečiama superkontinuumo signalu (sugeneruotu optimaliame kristale), buvo išbandytas ir išanalizuotas. Naujoviška, sinchroniškai kaupinama, savaime užkrečianti schema su modifikuotu GHz vorų FemtoLux 3 lazeriu buvo taip pat pristatyta.

Šiame skyriuje buvo atlikti superkontinuumo generacijos tyrimai keliuose dažnai naudojamuose ir mažai tyrinėtuose (dvejuose seskvioksiduose ir deimante) kristaluose. Atliekant eksperimentus buvo pastebėta greita Y_2O_3 kristalo ir keramikos degradacija, todėl šie kristalai esant naudojamoms eksperimente kaupinimo sąlygoms nėra praktiškai pritaikomi. Stimuliuotai Ramano sklaidai aktyvūs kristalai (KGW, deimantas, $CaWO_4$) pademonstravo gerus rezultatus generuojant superkontinuumą NIR spektrinėje srityje. Su ribota kaupinimo energija (1 µJ), spektro išplitimas į NIR sritį iki 1900-1950 nm buvo pademonstruotas. Tuo tarpu stimuliuotai Ramano sklaidai neaktyvūs kristalai (YAG, Y_2O_3, Lu_2O_3) pademonstravo geresnius rezultatus generuojant superkontinuumą matomoje-NIR spektro srityje ir išplitimas iki 480-500 nm buvo užregistruotas. Atliekant eksperimentus pastebėta, kad kai kurių stimuliuotai Ramano sklaidai aktyvių kristalų superkontinuumo generavimo slenksčiai buvo mažesni nei tikėtasi iš kritinės savifokusacijos

galios skaičiavimų. Tai gali būti indikacija, kad dėl Ramano sklaidos medžiagos netiesinis lūžio rodiklis yra modifikuojamas. Kadangi nustatyti superkontinuumo generacijos slenksčiai šiuose kristaluose yra mažiausi, stimuliuotai Ramano sklaidai aktyvūs kristalai yra tinkamas pasirinkimas mažos energijos taikymuose.

Panaudojus surinktą tyrimų informaciją femtosekundinio NIR šaltinio schema buvo pademonstruota. SRA schemoje, kuri buvo užkrečiama superkontinuumo spinduliuote sugeneruota KGW kristale ir pastiprinta deimanto kristale, pasiekta 130 mW išėjimo galia ties diskretiniu 1194 nm bangos ilgiu, kas atitiko apie 9% energijos keitimą iš kaupinimo spinduliuotės į signalą.

Nedidelės išėjimo galios femtosekundinių lazerių, kurių vidutinė galia keli Vatai, o impulsų energija keletas mikro-Džaulių, bangos ilgis gali būti efektyviai pastumtas panaudojus superkontinuumo stiprinimo schemą. Buvo pademonstruotas būdas, kaip pagaminti pigų ir paprastą fiksuoto ar diskretiškai derinamo bangos ilgio lazerinį šaltinį, efektyviai panaudojus kaupinančio lazerio energiją superkontinuumo generacijai ir po to kitai stiprinimo pakopai.

Galiausiai buvo pristatyta netiesinei biologinių audinių mikroskopijai skirto lazerinio šaltinio koncepcija. Šis metodas apjungia sinchroninį kaupinimą su naujai sukurtomis ir ištestuotomis technologijomis, kurios yra aprašytos šiame darbe bei patentinėje paraiškoje P1. Remiantis panaudotų technologijų eksperimentiniais rezultatais bei galutinės sistemos skaitmeniniais modeliavimais galima daryti išvadą, kad ši koncepcija yra perspektyvus, patikimas, kompaktiškas ir efektyvus sprendimas femtosekundiniams NIR spektrinio diapazono impulsams gauti.

Išvados

1. Dviejų kanalų skaidulinio užkrato lazerio bei jo impulsų stiprinimo siaurajuosčiame pikosekundiniame Nd:YVO_4 regeneraciniame stiprintuve ir plačiajuosčiame daugiapakopiame vid-IR (2-10 μm) OPA, kur panaudotas efektyvus mažos energijos superkontinuumo užkrato parametrinis priešstiprintuvis BBO kristale, kombinacija, leidžia realizuoti hibridinę plačiajuostę (iki 550 cm^{-1} ir iki 850 cm^{-1} naudojant kristalo skenavimo metodą) aukštos rezoliucijos (<3 cm^{-1}) SFG spektrometro sistemą.
2. Grįžtamojo ryšio kilpos panaudojimas lazerinio diodo spinduliuote moduliuojamos erbiu legiruotos skaidulos principu veikiančio fazės

valdiklio schemoje leidžia padidinti jo atsako greitį iki 100 kartų. Atsako greitis gali būti padidintas dar daugiau panaudojus didesnės galios kaupinimo spinduliuotę, tačiau nestabilumai kylantys dėl išaugusio terminio krūvio turi būti eliminuoti.

3. Mažos rezonatoriaus dispersijos (-0.27 ps^2) skaidulinio osciliatoriaus ir erbiu legiruotos skaidulos fazės valdiklio panaudojimas leidžia realizuoti stabilizuoto pasikartojimo dažnio sinchronizuotų modų skaidulinio osciliatoriaus, kurio centrinis bangos ilgis 1030 nm, schemą su kuria galima pasiekti stabilų pasikartojimo dažnio pririšimą prie išorinio elektrinio šaltinio su mažesniu nei 200 fs laikiniu drebėjimu.

4. Superkontinuumo spinduliuote užkrečiama stimuliuotai Ramano sklaidai aktyvaus kristalo stiprintuvo schema leidžia realizuoti efektyvų µJ-lygio femtosekundinio 1 µm lazerio bangos ilgio keitimą į biologiniams audiniams skaidrią sritį (1.1-1.35 µm) NIR regione. Be to, tokios Ramano stiprintuvo schemos bei GHz voras generuojančio kaupinimo lazerio, sinchroninio kaupinimo ir visiškai skaidulinio pasikartojimo dažnio pririšimo metodų panaudojimas atveria kelią pagerinto efektyvumo ir kompaktiškesniam bangos ilgio keitimo koncepcijos realizavimui.

BIBLIOGRAPHY

[1] T. H. Maiman, "Stimulated Optical Radiation in Ruby," Nature **187**, 493–494 (1960).

[2] P. P. Sorokin and M. J. Stevenson, "Stimulated Infrared Emission from Trivalent Uranium," Phys. Rev. Lett. **5**, 557–559 (1960).

[3] Y. Ishida and T. Yajima, "Characteristics of a new-type SHG crystala β-BaB_2O_4 in the femtosecond region," Opt. Commun. **62**, 197–200 (1987).

[4] A. G. Lambert, P. B. Davies, and D. J. Neivandt, "Implementing the theory of sum frequency generation vibrational spectroscopy: A tutorial review," Appl. Spectrosc. Rev. **40**, 103–145 (2005).

[5] C. S. Tian and Y. R. Shen, "Recent progress on sum-frequency spectroscopy," Surf. Sci. Rep. **69**, 105–131 (2014).

[6] J. P. Smith and V. Hinson-Smith, "Product Review: SFG coming of age," Anal. Chem. **76**, 287 A-290 A (2004).

[7] T. V. Andersen, O. Schmidt, C. Bruchmann, J. Limpert, C. Aguergaray, E. Cormier, and A. Tünnermann, "High repetition rate tunable femtosecond pulses and broadband amplification from fiber laser pumped parametric amplifier," Opt. Express **14**, 4765–4773 (2006).

[8] J. Trägårdh, J. Schniete, M. Parsons, and G. McConnell, "A femtosecond Raman generator for long wavelength two-photon and third harmonic generation imaging," APL Photonics **1**, 091303 (2016).

[9] M. Murtagh, J. Lin, R. P. Mildren, G. McConnell, and D. J. Spence, "Efficient diamond Raman laser generating 65 fs pulses," Opt. Express **23**, 15504–15513 (2015).

[10] R. W. Boyd, *Nonlinear Optics* (Elsevier, 2020).

[11] A. P. Stabinis and G. Valiulis, *Ultratrumpųjų Šviesos Impulsų Netiesinė Optika* (TEV, 2008).

[12] A. Dubietis, *Netiesinė Optika* (Vilniaus universiteto leidykla, 2011).

[13] G. Cerullo and S. De Silvestri, "Ultrafast optical parametric amplifiers," Rev. Sci. Instrum. **74**, 1–18 (2003).

[14] M. V. Hobden and J. Warner, "The temperature dependence of the refractive indices of pure lithium niobate," Phys. Lett. **22**, 243–244 (1966).

[15] W. R. Bosenberg and D. R. Guyer, "Broadly tunable, single-frequency optical parametric frequency-conversion system," J. Opt. Soc. Am. B **10**, 1716–1722 (1993).

[16] G. M. Gale, M. Cavallari, T. J. Driscoll, and F. Hache, "Sub-20-fs tunable pulses in the visible from an 82-MHz optical parametric oscillator," Opt. Lett. **20**, 1562–1564 (1995).

[17] D. J. Spence, "Spectral effects of stimulated Raman scattering in crystals," Prog. Quantum Electron. **51**, 1–45 (2017).

[18] L. Sirleto, A. Vergara, and M. A. Ferrara, "Advances in stimulated Raman scattering in nanostructures," Adv. Opt. Photonics **9**, 169–217 (2017).

[19] P. E. Powers, *Field Guide to Nonlinear Optics* (SPIE, 2013).

[20] P. A. Franken, A. E. Hill, C. W. Peters, and G. Weinreich, "Generation of Optical Harmonics," Phys. Rev. Lett. **7**, 118–119 (1961).

[21] J. A. Armstrong, N. Bloembergen, J. Ducuing, and P. S. Pershan, "Interactions between light waves in a nonlinear dielectric," Phys. Rev. **127**, 1918–1939

(1962).
[22] N. Bloembergen, R. K. Chang, S. S. Jha, and C. H. Lee, "Optical Second-Harmonic Generation in Reflection from Media with Inversion Symmetry," Phys. Rev. **174**, 813–822 (1968).
[23] J. M. Chen, J. R. Bower, C. S. Wang, and C. H. Lee, "Optical second-harmonic generation from submonolayer Na-covered Ge surfaces," Opt. Commun. **9**, 132–134 (1973).
[24] M. Fleischmann, P. J. Hendra, and A. J. McQuillan, "Raman spectra of pyridine adsorbed at a silver electrode," Chem. Phys. Lett. **26**, 163–166 (1974).
[25] T. E. Furtak and J. Reyes, "A critical analysis of theoretical models for the giant Raman effect from adsorbed molecules," Surf. Sci. **93**, 351–382 (1980).
[26] C. K. Chen, T. F. Heinz, D. Ricard, and Y. R. Shen, "Detection of molecular monolayers by optical second-harmonic generation," Phys. Rev. Lett. **46**, 1010–1012 (1981).
[27] T. F. Heinz, C. K. Chen, D. Ricard, and Y. R. Shen, "Optical second-harmonic generation from a monolayer of centrosymmetric molecules adsorbed on silver," Chem. Phys. Lett. **83**, 180–182 (1981).
[28] G. T. Boyd, Y. R. Shen, and T. W. Hänsch, "Second-Harmonic Generation from Sub-Monolayer Molecular Adsorbates Using a CW Diode Laser — Maui Surface Experiment," in *Laser Spectroscopy VII* **49**, 322–323, (Springer Berlin Heidelberg, 1985).
[29] N. Bloembergen and P. S. Pershan, "Light Waves at the Boundary of Nonlinear Media," Phys. Rev. **128**, 606–622 (1962).
[30] C. C. Wang, "Second-harmonic generation of light at the boundary of an isotropic medium," Phys. Rev. **178**, 1457–1460 (1969).
[31] P. Guyot-Sionnest, W. Chen, and Y. R. Shen, "General considerations on optical second-harmonic generation from surfaces and interfaces," Phys. Rev. B **33**, 8254–8263 (1986).
[32] T. F. Heinz, C. K. Chen, D. Ricard, and Y. R. Shen, "Spectroscopy of Molecular Monolayers by Resonant Second-Harmonic Generation," Phys. Rev. Lett. **48**, 478–481 (1982).
[33] T. F. Heinz, H. W. K. Tom, and Y. R. Shen, "Determination of molecular orientation of monolayer adsorbates by optical second-harmonic generation," Phys. Rev. A **28**, 1883–1885 (1983).
[34] G. Berkovic, T. Rasing, and Y. R. Shen, "Study of monolayer polymerization using nonlinear optics," J. Chem. Phys. **85**, 7374–7376 (1986).
[35] K. Bhattacharyya, E. V Sitzmann, and K. B. Eisenthal, "Study of chemical reactions by surface second harmonic generation: p -Nitrophenol at the air–water interface," J. Chem. Phys. **87**, 1442–1443 (1987).
[36] P. Guyot-Sionnest, H. Hsiung, and Y. R. Shen, "Surface Polar Ordering in a Liquid Crystal Observed by Optical Second-Harmonic Generation," Phys. Rev. Lett. **57**, 2963–2966 (1986).
[37] J. Reif, J. C. Zink, C. M. Schneider, and J. Kirschner, "Effects of surface magnetism on optical second harmonic generation," Phys. Rev. Lett. **67**, 2878–2881 (1991).
[38] T. Rasing, Y. R. Shen, M. W. Kim, and S. Grubb, "Observation of molecular reorientation at a two-dimensional-liquid phase transition," Phys. Rev. Lett. **55**, 2903–2906 (1985).

[39] Y. R. Shen, "Surface nonlinear optics [Invited]," J. Opt. Soc. Am. B **28**, A56 (2011).

[40] Y. R. Shen, *Fundamentals of Sum-Frequency Spectroscopy* (Cambridge University Press, 2016).

[41] X. D. Zhu, H. Suhr, and Y. R. Shen, "Surface vibrational spectroscopy by infrared-visible sum frequency generation," Phys. Rev. B **35**, 3047–3050 (1987).

[42] J. H. Hunt, P. Guyot-Sionnest, and Y. R. Shen, "Observation of C-H stretch vibrations of monolayers of molecules optical sum-frequency generation," Chem. Phys. Lett. **133**, 189–192 (1987).

[43] A. L. Harris, C. E. D. Chidsey, N. J. Levinos, and D. N. Loiacono, "Monolayer vibrational spectroscopy by infrared-visible sum generation at metal and semiconductor surfaces," Chem. Phys. Lett. **141**, 350–356 (1987).

[44] R. Superfine, J. Y. Huang, and Y. R. Shen, "Experimental determination of the sign of molecular dipole moment derivatives: an infrared-visible sum frequency generation absolute phase measurement study," Chem. Phys. Lett. **172**, 303–306 (1990).

[45] R. Superfine, J. Y. Huang, and Y. R. Shen, "Nonlinear optical studies of the pure liquid/vapor interface: Vibrational spectra and polar ordering," Phys. Rev. Lett. **66**, 1066–1069 (1991).

[46] Y. R. Shen, "Surface properties probed by second-harmonic and sum-frequency generation," Nature **337**, 519–525 (1989).

[47] K. B. Eisenthal, "Liquid interfaces probed by second-harmonic and sum-frequency spectroscopy," Chem. Rev. **96**, 1343–1360 (1996).

[48] H. F. Wang, W. Gan, R. Lu, Y. Rao, and B. H. Wu, "Quantitative spectral and orientational analysis in surface sum frequency generation vibrational spectroscopy (SFG-VS)," Int. Rev. Phys. Chem. **24**, 191–256 (2005).

[49] Q. Du, R. Superfine, E. Freysz, and Y. R. Shen, "Vibrational spectroscopy of water at the vapor/water interface," Phys. Rev. Lett. **70**, 2313–2316 (1993).

[50] Q. Du, E. Freysz, and Y. R. Shen, "Vibrational spectra of water molecules at quartz/water interfaces," Phys. Rev. Lett. **72**, 238–241 (1994).

[51] Q. Du, E. Freysz, and Y. R. Shen, "Surface Vibrational Spectroscopic Studies of Hydrogen Bonding and Hydrophobicity," Science **264**, 826–828 (1994).

[52] Y. R. Shen, "Optical Second Harmonic Generation at Interfaces," Annu. Rev. Phys. Chem. **40**, 327–350 (1989).

[53] Y. R. Shen, "Surfaces probed by nonlinear optics," Surf. Sci. **299**–**300**, 551–562 (1994).

[54] M. B. Raschke, M. Hayashi, S. H. Lin, and Y. R. Shen, "Doubly-resonant sum-frequency generation spectroscopy for surface studies," Chem. Phys. Lett. **359**, 367–372 (2002).

[55] B. C. Chow, T. T. Ehler, and T. E. Furtak, "High-resolution sum-frequency generation from alkylsiloxane monolayers," Appl. Phys. B Lasers Opt. **74**, 395–399 (2002).

[56] G. Niaura, Z. Kuprionis, I. Ignatjev, M. Kažemékaité, G. Valincius, Z. Talaikyte, V. Razumas, and A. Svendsen, "Probing of lipase activity at air/water interface by sum-frequency generation spectroscopy," J. Phys. Chem. B **112**, 4094–4101 (2008).

[57] S. Strazdaite, E. Navakauskas, J. Kirschner, T. Sneideris, and G. Niaura, "Structure Determination of Hen Egg-White Lysozyme Aggregates Adsorbed

to Lipid/Water and Air/Water Interfaces," Langmuir **36**, 4766–4775 (2020).

[58] A. Lagutchev, A. Lozano, P. Mukherjee, S. A. Hambir, and D. D. Dlott, "Spectrochimica Acta Part A : Molecular and Biomolecular Spectroscopy Compact broadband vibrational sum-frequency generation spectrometer with nonresonant suppression," Spectrochim. Acta Part A Mol. Biomol. Spectrosc. **75**, 1289–1296 (2010).

[59] O. Isaienko and E. Borguet, "Ultra-broadband sum-frequency spectrometer of aqueous interfaces based on a non-collinear optical parametric amplifier," Opt. Express **20**, 547–561 (2012).

[60] R. Zhang, X. Peng, Z. Jiao, T. Luo, C. Zhou, X. Yang, and Z. Ren, "Flexible high-resolution broadband sum-frequency generation vibrational spectroscopy for intrinsic spectral line widths," J. Chem. Phys. **150**, 074702 (2019).

[61] Z. Heiner, V. Petrov, and M. Mero, "Compact, high-repetition-rate source for broadband sum-frequency generation spectroscopy," APL Photonics **2**, 066102 (2017).

[62] L. Velarde, X. Zhang, Z. Lu, A. G. Joly, Z. Wang, and H. Wang, "Communication: Spectroscopic phase and lineshapes in high-resolution broadband sum frequency vibrational spectroscopy: Resolving interfacial inhomogeneities of “identical” molecular groups," J. Chem. Phys. **135**, 241102 (2011).

[63] R. Feng, L. Lin, Y. Li, M. Liu, Y. Guo, and Z. Zhang, "Effect of Ca^{2+} to Sphingomyelin Investigated by Sum Frequency Generation Vibrational Spectroscopy," Biophys. J. **112**, 2173–2183 (2017).

[64] L. Velarde and H. F. Wang, "Unified treatment and measurement of the spectral resolution and temporal effects in frequency-resolved sum-frequency generation vibrational spectroscopy (SFG-VS)," Phys. Chem. Chem. Phys. **15**, 19970–19984 (2013).

[65] L. Velarde and H. F. Wang, "Capturing inhomogeneous broadening of the -CN stretch vibration in a Langmuir monolayer with high-resolution spectra and ultrafast vibrational dynamics in sum-frequency generation vibrational spectroscopy (SFG-VS)," J. Chem. Phys. **139**, (2013).

[66] K. Michailovas, A. Baltuska, A. Pugzlys, V. Smilgevicius, A. Michailovas, A. Zaukevicius, R. Danilevicius, S. Frankinas, and N. Rusteika, "Combined Yb/Nd driver for optical parametric chirped pulse amplifiers," Opt. Express **24**, 22261–22271 (2016).

[67] R. Danilevičius, A. Zaukevičius, R. Budriūnas, A. Michailovas, and N. Rusteika, "Femtosecond wavelength-tunable OPCPA system based on picosecond fiber laser seed and picosecond DPSS laser pump," Opt. Express **24**, 17532–17540 (2016).

[68] L. J. Richter, T. P. Petralli-Mallow, and J. C. Stephenson, "Vibrationally resolved sum-frequency generation with broad-bandwidth infrared pulses," Opt. Lett. **23**, 1594–1596 (1998).

[69] Z. Heiner, L. Wang, V. Petrov, and M. Mero, "Broadband vibrational sum-frequency generation spectrometer at 100 kHz in the 950-1750 cm^{-1} spectral range utilizing a $LiGaS_2$ optical parametric amplifier," Opt. Express **27**, 15289–15297 (2019).

[70] G. B. Abdullaev, K. R. Allakhverdiev, L. A. Kulevskii, A. M. Prokhorov, É. Y. Salaev, A. D. Savel’ev, and V. V Smirnov, "Parametric conversion of

infrared radiation in a GaSe crystal," Sov. J. Quantum Electron. **5**, 665–668 (1975).

[71] Y. X. Fan, R. C. Eckardt, R. L. Byer, R. K. Route, and R. S. Feigelson, "$AgGaS_2$ infrared parametric oscillator," Appl. Phys. Lett. **45**, 313–315 (1984).

[72] L. I. Isaenko and A. P. Yelisseyev, "Recent studies of nonlinear chalcogenide crystals for the mid-IR," Semicond. Sci. Technol. **31**, 123001 (2016).

[73] P.-M. J. M. Dansette, "A tunable femtosecond fiber laser source for multiphoton emission microscopy," EPFL (2021).

[74] P. M. Dansette, R. Burokas, L. Veselis, A. Zaukevičius, A. Michailovas, and N. Rusteika, "Peculiarities of second harmonic generation with chirped femtosecond pulses at high conversion efficiency," Opt. Commun. **455**, 124462 (2020).

[75] D. N. Nikogosyan, "Beta barium borate (BBO)," Appl. Phys. A Solids Surfaces **52**, 359–368 (1991).

[76] H. Nakatani, W. R. Bosenberg, L. K. Cheng, and C. L. Tang, "Laser-induced damage in beta-barium metaborate," Appl. Phys. Lett. **53**, 2587–2589 (1988).

[77] M. Bradler, C. Homann, and E. Riedle, "Mid-IR femtosecond pulse generation on the microjoule level up to 5 μm at high repetition rates," Opt. Lett. **36**, 4212–4214 (2011).

[78] B.-H. Chen, E. Wittmann, Y. Morimoto, P. Baum, and E. Riedle, "Octave-spanning single-cycle middle-infrared generation through optical parametric amplification in $LiGaS_2$," Opt. Express **27**, 21306–21318 (2019).

[79] M. A. Leigh, W. Shi, J. Zong, Z. Yao, S. Jiang, and N. Peyghambarian, "Narrowband pulsed THz source using eyesafe region fiber lasers and a nonlinear crystal," IEEE Photonics Technol. Lett. **21**, 27–29 (2009).

[80] C. Cleff, J. Epping, P. Gross, and C. Fallnich, "Femtosecond OPO based on LBO pumped by a frequency-doubled Yb-fiber laser-amplifier system for CARS spectroscopy," Appl. Phys. B Lasers Opt. **103**, 795–800 (2011).

[81] J. Kim and Y. Song, "Ultralow-noise mode-locked fiber lasers and frequency combs: principles, status, and applications," Adv. Opt. Photonics **8**, 465–540 (2016).

[82] T. Yasui, M. Nose, A. Ihara, K. Kawamoto, S. Yokoyama, H. Inaba, K. Minoshima, and T. Araki, "Fiber-based, hybrid terahertz spectrometer using dual fiber combs," Opt. Lett. **35**, 1689–1691 (2010).

[83] N. J. Doran and D. Wood, "Nonlinear-optical loop mirror," Opt. Lett. **13**, 56–58 (1988).

[84] M. E. Fermann, F. Haberl, M. Hofer, and H. Hochreiter, "Nonlinear amplifying loop mirror," Opt. Lett. **15**, 752–754 (1990).

[85] I. N. Duling, "All-fiber ring soliton laser mode locked with a nonlinear mirror," Opt. Lett. **16**, 539–541 (1991).

[86] W. Hänsel, H. Hoogland, M. Giunta, S. Schmid, T. Steinmetz, R. Doubek, P. Mayer, S. Dobner, C. Cleff, M. Fischer, and R. Holzwarth, "All polarization-maintaining fiber laser architecture for robust femtosecond pulse generation," Appl. Phys. B Lasers Opt. **123**, 41 (2017).

[87] H. A. Haus, E. P. Ippen, and K. Tamura, "Additive-Pulse Modelocking in Fiber Lasers," IEEE J. Quantum Electron. **30**, 200–208 (1994).

[88] M. E. Fermann, M. L. Stock, M. J. Andrejco, and Y. Silberberg, "Passive mode locking by using nonlinear polarization evolution in a polarization-

maintaining erbium-doped fiber," Opt. Lett. **18**, 894–896 (1993).
[89] C. K. Nielsen, B. Ortaç, T. Schreiber, J. Limpert, R. Hohmuth, W. Richter, and A. Tünnermann, "Self-starting self-similar all-polarization maintaining Yb-doped fiber laser," Opt. Express **13**, 9346–9351 (2005).
[90] J. Szczepanek, T. M. Kardaś, C. Radzewicz, and Y. Stepanenko, "Nonlinear polarization evolution of ultrashort pulses in polarization maintaining fibers," Opt. Express **26**, 13590–13604 (2018).
[91] G. Khoe and I. Introduction, "New Endless Polarization Control Method Using Three Fiber Squeezers," **7**, 1033–1043 (1989).
[92] G. Pu, L. Zhang, W. Hu, and L. Yi, "Automatic mode-locking fiber lasers: progress and perspectives," Sci. China Inf. Sci. **63**, 160404 (2020).
[93] G. Pu, L. Yi, L. Zhang, and W. Hu, "Intelligent programmable mode-locked fiber laser with a human-like algorithm," Optica **6**, 362–369 (2019).
[94] X. Shen, W. Li, M. Yan, and H. Zeng, "Electronic control of nonlinear-polarization-rotation mode locking in Yb-doped fiber lasers," Opt. Lett. **37**, 3426–3428 (2012).
[95] Q. Bao, H. Zhang, Y. Wang, Z. Ni, Y. Yan, Z. X. Shen, K. P. Loh, and D. Y. Tang, "Atomic-layer craphene as a saturable absorber for ultrafast pulsed lasers," Adv. Funct. Mater. **19**, 3077–3083 (2009).
[96] S. Y. Set, H. Yaguchi, Y. Tanaka, and M. Jablonski, "Laser Mode Locking Using a Saturable Absorber Incorporating Carbon Nanotubes," J. Light. Technol. **22**, 51–56 (2004).
[97] S. Hong, F. Lédée, J. Park, S. Song, H. Lee, Y. S. Lee, B. Kim, D. Il Yeom, E. Deleporte, and K. Oh, "Mode-Locking of All-Fiber Lasers Operating at Both Anomalous and Normal Dispersion Regimes in the C- and L-Bands Using Thin Film of 2D Perovskite Crystallites," Laser Photon. Rev. **12**, 1800118 (2018).
[98] W. Liu, L. Pang, H. Han, W. Tian, H. Chen, M. Lei, P. Yan, and Z. Wei, "70-fs mode-locked erbium-doped fiber laser with topological insulator," Sci. Rep. **6**, 19997 (2016).
[99] R. I. Woodward and E. J. R. Kelleher, "2D saturable absorbers for fibre lasers," Appl. Sci. **5**, 1440–1456 (2015).
[100] O. Okhotnikov, A. Grudinin, and M. Pessa, "Ultra-fast fibre laser systems based on SESAM technology: new horizons and applications," New J. Phys. **6**, 177 (2004).
[101] U. Keller, K. J. Weingarten, F. X. Kärtner, D. Kopf, B. Braun, I. D. Jung, R. Fluck, C. Hönninger, N. Matuschek, and J. Aus Der Au, "Semiconductor saturable absorber mirrors (SESAM's) for femtosecond to nanosecond pulse generation in solid-state lasers," IEEE J. Sel. Top. Quantum Electron. **2**, 435–451 (1996).
[102] F. X. Kärtner, I. D. Jung, and U. Keller, "Soliton mode-locking with saturable absorbers," IEEE J. Sel. Top. Quantum Electron. **2**, 540–556 (1996).
[103] K. Viskontas, K. Regelskis, and N. Rusteika, "Slow and fast optical degradation of the SESAM for fiber laser mode-locking at 1 μm," Lith. J. Phys. **54**, 127–135 (2014).
[104] X. Zhou, D. Yoshitomi, Y. Kobayashi, and K. Torizuka, "Generation of 28-fs pulses from a mode-locked ytterbium fiber oscillator," Opt. Express **16**, 7055–7059 (2008).
[105] X. Liu, J. Lægsgaard, and D. Turchinovich, "Highly-stable monolithic

femtosecond Yb-fiber laser system based on photonic crystal fibers," Opt. Express **18**, 15475–15483 (2010).

[106] B. Ortaç, M. Plötner, J. Limpert, and A. Tünnermann, "Self-starting passively mode-locked chirped-pulse fiber laser," Opt. Express **15**, 16794–16799 (2007).

[107] K. Regelskis, J. Želudevičius, K. Viskontas, and G. Račiukaitis, "Ytterbium-doped fiber ultrashort pulse generator based on self-phase modulation and alternating spectral filtering," Opt. Lett. **40**, 5255–5258 (2015).

[108] Z. Liu, Z. M. Ziegler, L. G. Wright, and F. W. Wise, "Megawatt peak power from a Mamyshev oscillator," Optica **4**, 649–654 (2017).

[109] P. V. Mamyshev, "All-optical data regeneration based on self-phase modulation effect," in *24th European Conference on Optical Communication. ECOC '98 (IEEE Cat. No.98TH8398)* **1**, 475–476, (Telefonica, 1998).

[110] I. Samartsev, A. Bordenyuk, and V. Gapontsev, "Environmentally stable seed source for high power ultrafast laser," Components Packag. Laser Syst. III **10085**, 100850S (2017).

[111] P. Repgen, B. Schuhbauer, M. Hinkelmann, D. Wandt, A. Wienke, U. Morgner, J. Neumann, and D. Kracht, "Mode-locked pulses from a Thulium-doped fiber Mamyshev oscillator," Opt. Express **28**, 13837–13844 (2020).

[112] P. Sidorenko, W. Fu, L. G. Wright, and F. W. Wise, "Multi-megawatt, self-seeded Mamyshev oscillator," in *Advanced Photonics 2018 (BGPP, IPR, NP, NOMA, Sensors, Networks, SPPCom, SOF)* SoM3H.4, (OSA, 2018).

[113] W. Fu, L. G. Wright, P. Sidorenko, S. Backus, and F. W. Wise, "Several new directions for ultrafast fiber lasers [Invited]," Opt. Express **26**, 9432–9463 (2018).

[114] W. Zhang, H. Han, Y. Zhao, Q. Du, and Z. Wei, "A 350MHz Ti:sapphire laser comb based on monolithic scheme and absolute frequency measurement of 729nm laser," Opt. Express **17**, 6059–6067 (2009).

[115] A. Ruehl, A. Marcinkevicius, M. E. Fermann, and I. Hartl, "80 W, 120 fs Yb-fiber frequency comb," Opt. Lett. **35**, 3015–3017 (2010).

[116] F. Adler, K. Moutzouris, A. Leitenstorfer, H. Schnatz, B. Lipphardt, G. Grosche, and F. Tauser, "Phase-locked two-branch erbium-doped fiber laser system for long-term precision measurements of optical frequencies," Opt. Express **12**, 5872–5880 (2004).

[117] D. C. Heinecke, A. Bartels, and S. A. Diddams, "Offset frequency dynamics and phase noise properties of a self-referenced 10 GHz Ti:sapphire frequency comb," Opt. Express **19**, 18440–18451 (2011).

[118] J. A. Cox, A. H. Nejadmalayeri, J. Kim, and F. X. Kärtner, "Complete characterization of quantum-limited timing jitter in passively mode-locked fiber lasers," Opt. Lett. **35**, 3522–3524 (2010).

[119] T. C. Briles, D. C. Yost, A. Cingöz, J. Ye, and T. R. Schibli, "Simple piezoelectric-actuated mirror with 180 kHz servo bandwidth," Opt. Express **18**, 9739–9746 (2010).

[120] A. Chadi, G. Méjean, R. Grilli, and D. Romanini, "Note: Simple and compact piezoelectric mirror actuator with 100 kHz bandwidth, using standard components," Rev. Sci. Instrum. **84**, 056112 (2013).

[121] D. Goldovsky, V. Jouravsky, and A. Pe'er, "Simple and robust phase-locking of optical cavities with > 200 KHz servo-bandwidth using a piezo-actuated mirror mounted in soft materials," Opt. Express **24**, 28239–28246 (2016).

[122] T. Nakamura, S. Tani, I. Ito, M. Endo, and Y. Kobayashi, "Piezo-electric transducer actuated mirror with a servo bandwidth beyond 500 kHz," Opt. Express **28**, 16118–16125 (2020).

[123] D. D. Hudson, K. W. Holman, R. J. Jones, S. T. Cundiff, J. Ye, and D. J. Jones, "Mode-locked fiber laser frequency-controlled with an intracavity electro-optic modulator," Opt. Lett. **30**, 2948–2950 (2005).

[124] Y. Nakajima, H. Inaba, K. Hosaka, K. Minoshima, A. Onae, M. Yasuda, T. Kohno, S. Kawato, T. Kobayashi, T. Katsuyama, and F.-L. Hong, "A multi-branch, fiber-based frequency comb with millihertz-level relative linewidths using an intra-cavity electro-optic modulator," Opt. Express **18**, 1667–1676 (2010).

[125] K. Iwakuni, H. Inaba, Y. Nakajima, T. Kobayashi, K. Hosaka, A. Onae, and F. L. Hong, "Narrow linewidth comb realized with a mode-locked fiber laser using an intra-cavity waveguide electro-optic modulator for high-speed control," Opt. Express **20**, 13769–13776 (2012).

[126] Wei Zhang, M. Lours, M. Fischer, R. Holzwarth, G. Santarelli, and Y. Le Coq, "Characterizing a fiber-based frequency comb with electro-optic modulator," IEEE Trans. Ultrason. Ferroelectr. Freq. Control **59**, 432–438 (2012).

[127] S. Okubo, K. Gunji, A. Onae, M. Schramm, K. Nakamura, F. Hong, T. Hattori, K. Hosaka, and H. Inaba, "All-optically stabilized frequency comb," Appl. Phys. Express **8**, 122701 (2015).

[128] B. R. Washburn, S. A. Diddams, and N. R. Newbury, "Phase-locked , erbium-fiber-laser-based frequency comb in the near infrared," **29**, 250–252 (2004).

[129] K. Yang, P. Zhao, J. Luo, K. Huang, Q. Hao, and H. Zeng, "Comparison on different repetition rate locking methods in Er-doped fiber laser," Laser Phys. **28**, 055108 (2018).

[130] H. Hundertmark, D. Wandt, C. Fallnich, N. Haverkamp, and H. R. Telle, "Phase-locked carrier-envelope-offset frequency at 1560 nm," Opt. Express **12**, 770–775 (2004).

[131] N. Haverkamp, H. Hundertmark, C. Fallnich, and H. R. Telle, "Frequency stabilization of mode-locked Erbium fiber lasers using pump power control," Appl. Phys. B Lasers Opt. **78**, 321–324 (2004).

[132] X. Shen, B. He, J. Zhao, Y. Liu, D. Bai, K. Yang, C. Wang, G. Liu, D. Luo, F. Liu, Q. Hao, W. Li, and H. Zeng, "Repetition rate stabilization of an erbium-doped all-fiber laser via opto-mechanical control of the intracavity group velocity," Appl. Phys. Lett. **106**, 031117 (2015).

[133] K. Yin, B. Zhang, L. Yang, and J. Hou, "152 W spectrally flat all-fiber supercontinuum laser source with >1 W power beyond 38 μm," Opt. Lett. **42**, 2334–2337 (2017).

[134] K. Yang, Q. Hao, and H. Zeng, "All-Optical High-Precision Repetition Rate Locking of an Yb-Doped Fiber Laser," IEEE Photonics Technol. Lett. **27**, 852–855 (2015).

[135] S. Rieger, T. Hellwig, T. Walbaum, and C. Fallnich, "Optical repetition rate stabilization of a mode-locked all-fiber laser," Opt. Express **21**, 4889–4895 (2013).

[136] Q. Hao, Q. Zhang, F. Chen, K. Yang, and H. Zeng, "All-Optical 20-μHz-Level Repetition Rate Stabilization of Mode Locking With a Nonlinear Amplifying Loop Mirror," J. Light. Technol. **34**, 2833–2837 (2016).

[137] R. de L. Kronig, "On the Theory of Dispersion of X-Rays," J. Opt. Soc. Am. **12**, 547–557 (1926).
[138] H. Tünnermann, J. Neumann, D. Kracht, and P. Weßels, "All-fiber phase actuator based on an erbium-doped fiber amplifier for coherent beam combining at 1064 nm," Opt. Lett. **36**, 448–450 (2011).
[139] Guan-Chyun Hsieh and J. C. Hung, "Phase-locked loop techniques. A survey," IEEE Trans. Ind. Electron. **43**, 609–615 (1996).
[140] Dong Hou, Bo Ning, Shuangyou Zhang, Jiutao Wu, and Jianye Zhao, "Long-Term Stabilization of Fiber Laser Using Phase-Locking Technique With Ultra-Low Phase Noise and Phase Drift," IEEE J. Sel. Top. Quantum Electron. **20**, 456–463 (2014).
[141] D. Hou, J. Wu, Q. Ren, and J. Zhao, "Analysis of long-term phase-locking technique for mode-locked laser with PID regulator," IEEE J. Quantum Electron. **48**, 839–846 (2012).
[142] D. Hou, B. Ning, P. Li, Z. Zhang, and J. Zhao, "Modeling analysis for phase-locking of mode-locked laser," IEEE J. Quantum Electron. **47**, 891–898 (2011).
[143] F. M. Gardner, *Phaselock Techniques* (John Wiley & Sons, Inc., 2005).
[144] W. Kester, "Converting Oscillator Phase Noise to Time Jitter," Analog Devices Inc. 1–10 (2009).
[145] C. Azeredo-Leme, "Clock Jitter Effects on Sampling: A Tutorial," IEEE Circuits Syst. Mag. **11**, 26–37 (2011).
[146] A. L. Lance, W. D. Seal, and F. Labaar, "Phase noise and AM noise measurements in the frequency domain," in *Infrared and Millimeter Waves* **11**, 239–289, (1984).
[147] U. L. Rohde, A. K. Poddar, and A. M. Apte, "Getting Its Measure: Oscillator Phase Noise Measurement Techniques and Limitations," IEEE Microw. Mag. **14**, 73–86 (2013).
[148] R. Hui and M. O'Sullivan, "Optical System Performance Measurements," in *Fiber Optic Measurement Techniques* (Elsevier, 2009).
[149] A. Vaupel, N. Bodnar, B. Webb, L. Shah, and M. Richardson, "Concepts, performance review, and prospects of table-top, few-cycle optical parametric chirped-pulse amplification," Opt. Eng. **53**, 051507 (2013).
[150] J. V Rudd, R. J. Law, T. S. Luk, and S. M. Cameron, "High-power optical parametric chirped-pulse amplifier system with a 1.55 μm signal and a 1064 μm pump," Opt. Lett. **30**, 1974–1976 (2005).
[151] R. Paschotta, "Timing jitter and phase noise of mode-locked fiber lasers," Opt. Express **18**, 5041–5054 (2010).
[152] Y. S. Kivshar and G. P. Agrawal, *Optical Solitons: From Fibers to Photonic Crystals* (Elsevier Science, 2003).
[153] N. Kuse, J. Jiang, C. C. Lee, T. R. Schibli, and M. E. Fermann, "All polarization-maintaining Er fiber-based optical frequency combs with nonlinear amplifying loop mirror," Opt. Express **24**, 3095–3102 (2016).
[154] J. P. Gordon and H. A. Haus, "Random walk of coherently amplified solitons in optical fiber transmission," Opt. Lett. **11**, 665–667 (1986).
[155] R. Riedel, M. Schulz, M. J. Prandolini, A. Hage, H. Höppner, T. Gottschall, J. Limpert, M. Drescher, and F. Tavella, "Long-term stabilization of high power optical parametric chirped-pulse amplifiers," Opt. Express **21**, 28987–28999 (2013).

[156] M. Schmitt, B. Dietzek, G. Hermann, and J. Popp, "Femtosecond time-resolved spectroscopy on biological photoreceptor chromophores," Laser Photonics Rev. **1**, 57–78 (2007).

[157] W. R. Zipfel, R. M. Williams, and W. W. Webb, "Nonlinear magic: multiphoton microscopy in the biosciences," Nat. Biotechnol. **21**, 1369–1377 (2003).

[158] N. G. Horton, K. Wang, D. Kobat, C. G. Clark, F. W. Wise, C. B. Schaffer, and C. Xu, "In vivo three-photon microscopy of subcortical structures within an intact mouse brain," Nat. Photonics **7**, 205–209 (2013).

[159] E. V. Kovalchuk, T. Schuldt, and A. Peters, "Combination of a continuous-wave optical parametric oscillator and a femtosecond frequency comb for optical frequency metrology," Opt. Lett. **30**, 3141–3143 (2005).

[160] L. M. G. van Huizen, N. V. Kuzmin, E. Barbé, S. van der Velde, E. A. te Velde, and M. L. Groot, "Second and third harmonic generation microscopy visualizes key structural components in fresh unprocessed healthy human breast tissue," J. Biophotonics **12**, 1–11 (2019).

[161] L. A. Sordillo, Y. Pu, S. Pratavieira, Y. Budansky, and R. R. Alfano, "Deep optical imaging of tissue using the second and third near-infrared spectral windows," J. Biomed. Opt. **19**, 056004 (2014).

[162] A. M. Smith, M. C. Mancini, and S. Nie, "Bioimaging: Second window for in vivo imaging," Nat. Nanotechnol. **4**, 710–711 (2009).

[163] K. Welsher, S. P. Sherlock, and H. Dai, "Deep-tissue anatomical imaging of mice using carbon nanotube fluorophores in the second near-infrared window," Proc. Natl. Acad. Sci. **108**, 8943–8948 (2011).

[164] C. Li and Q. Wang, "Challenges and Opportunities for Intravital Near-Infrared Fluorescence Imaging Technology in the Second Transparency Window," ACS Nano **12**, 9654–9659 (2018).

[165] E. Hemmer, A. Benayas, F. Légaré, and F. Vetrone, "Exploiting the biological windows: current perspectives on fluorescent bioprobes emitting above 1000 nm," Nanoscale Horizons **1**, 168–184 (2016).

[166] D. C. Sordillo, L. A. Sordillo, P. P. Sordillo, and R. R. Alfano, "Fourth near-infrared optical window for assessment of bone and other tissues," in *Proc. SPIE* **9689**, 96894J, (2016).

[167] J. Adur, H. F. Carvalho, C. L. Cesar, and V. H. Casco, "Nonlinear Microscopy Techniques: Principles and Biomedical Applications," in *Microscopy and Analysis* 121–150, (InTech, 2016).

[168] F. Helmchen and W. Denk, "Deep tissue two-photon microscopy," Nat. Methods **2**, 932–940 (2005).

[169] S. W. Chu, S. Y. Chen, T. H. Tsai, T. M. Liu, C. Y. Lin, H. J. Tsai, and C. K. Sun, "In vivo developmental biology study using noninvasive multi-harmonic generation microscopy," Opt. Express **11**, 3093–3099 (2003).

[170] K. Guesmi, L. Abdeladim, S. Tozer, P. Mahou, T. Kumamoto, K. Jurkus, P. Rigaud, K. Loulier, N. Dray, P. Georges, M. Hanna, J. Livet, W. Supatto, E. Beaurepaire, and F. Druon, "Dual-color deep-tissue three-photon microscopy with a multiband infrared laser," Light Sci. Appl. **7**, 1–9 (2018).

[171] D. Kobat, M. E. Durst, N. Nishimura, A. W. Wong, C. B. Schaffer, and C. Xu, "Deep tissue multiphoton microscopy using longer wavelength excitation," Opt. Express **17**, 13354–13364 (2009).

[172] S. Wang, B. Li, and F. Zhang, "Molecular Fluorophores for Deep-Tissue

Bioimaging," ACS Cent. Sci. **6**, 1302–1316 (2020).
[173] R. R. Alfano and S. L. Shapiro, "Emission in the Region 4000 to 7000 Å Via Four-Photon Coupling in Glass," Phys. Rev. Lett. **24**, 584–587 (1970).
[174] A. Dubietis, G. Tamošauskas, R. Šuminas, V. Jukna, and A. Couairon, "Ultrafast supercontinuum generation in bulk condensed media," Lith. J. Phys. **57**, 113–157 (2017).
[175] S. Backus, C. G. Durfee, M. M. Murnane, and H. C. Kapteyn, "High power ultrafast lasers," Rev. Sci. Instrum. **69**, 1207–1223 (1998).
[176] Y. W. Tzeng, Y. Y. Lin, C. H. Huang, J. M. Liu, H. C. Chui, H. L. Liu, J. M. Stone, J. C. Knight, and S. W. Chu, "Broadband tunable optical parametric amplification from a single 50 MHz ultrafast fiber laser," Opt. Express **17**, 7304–7309 (2009).
[177] J. Mundry, J. Lohrenz, and M. Betz, "Tunable femtosecond near-IR source by pumping an OPA directly with a 90 MHz Yb:fiber source," Appl. Opt. **56**, 3104–3108 (2017).
[178] R. H. Stolen and E. P. Ippen, "Raman gain in glass optical waveguides," Appl. Phys. Lett. **22**, 276–278 (1973).
[179] P. Mackonis, A. Petrulenas, A. M. Rodin, V. Girdauskas, and A. Michailovas, "Two-stage transient stimulated Raman chirped-pulse amplification in $KGd(WO_4)_2$ with compression to 145 fs," Opt. Lett. **45**, 6627–6630 (2020).
[180] V. Krylov, V. Bespalov, D. Staselko, A. Rebane, D. Erni, O. Ollikainen, and U. Wild, "Stimulated Raman amplification of femtosecond pulses in hydrogen gas," Opt. Lett. **21**, 2005–2007 (1996).
[181] A. S. Grabtchikov, R. V. Chulkov, V. A. Orlovich, M. Schmitt, R. Maksimenko, and W. Kiefer, "Observation of Raman conversion for 70-fs pulses in $KGd(WO_4)_2$ crystal in the regime of impulsive stimulated Raman scattering," Opt. Lett. **28**, 926–928 (2003).
[182] M. Murtagh, J. Lin, R. P. Mildren, and D. J. Spence, "Ti:sapphire-pumped diamond Raman laser with sub-100-fs pulse duration," Opt. Lett. **39**, 2975–2978 (2014).
[183] J. Lin and D. J. Spence, "255 fs dissipative soliton diamond Raman laser," Opt. Lett. **41**, 1861–1864 (2016).
[184] M. Murtagh, J. Lin, J. Trägårdh, G. McConnell, and D. J. Spence, "Ultrafast second-Stokes diamond Raman laser," Opt. Express **24**, 8149–8155 (2016).
[185] E. P. Perillo, J. W. Jarrett, Y.-L. Liu, A. Hassan, D. C. Fernée, J. R. Goldak, A. Bonteanu, D. J. Spence, H.-C. Yeh, and A. K. Dunn, "Two-color multiphoton in vivo imaging with a femtosecond diamond Raman laser," Light Sci. Appl. **6**, e17095 (2017).
[186] Ekspla Ltd, "Femtolux 3," https://ekspla.com/product/microjoule-class-industrial-grade-femtosecond-fiber-laser-femtolux3/.
[187] A. Dementjev, R. Rudys, R. Karpicz, and D. Rutkauskas, "Optimization of wide-field second-harmonic generation microscopy for fast imaging of large sample areas in biological tissues," Lith. J. Phys. **60**, 145–153 (2020).
[188] R. R. Alfano, *The Supercontinuum Laser Source* (Springer New York, 2016).
[189] A. Couairon and A. Mysyrowicz, "Femtosecond filamentation in transparent media," Phys. Rep. **441**, 47–189 (2007).
[190] A. Couairon, E. Brambilla, T. Corti, D. Majus, O. de, and M. Kolesik, "Practitioner's guide to laser pulse propagation models and simulation," Eur. Phys. J. Spec. Top. **199**, 5–76 (2011).

[191] A. Šuminienė, V. Jukna, R. Šuminas, G. Tamošauskas, M. Vengris, and A. Dubietis, "Lisaf: An efficient and durable nonlinear material for supercontinuum generation in the ultraviolet," Lith. J. Phys. **60**, 217–224 (2020).

[192] J. Kohl-Landgraf, J. E. Nimsch, and J. Wachtveitl, "LiF, an underestimated supercontinuum source in femtosecond transient absorption spectroscopy," Opt. Express **21**, 17060–17065 (2013).

[193] A. Brodeur and S. L. Chin, "Band-Gap Dependence of the Ultrafast White-Light Continuum," Phys. Rev. Lett. **80**, 4406–4409 (1998).

[194] A. Brodeur and S. L. Chin, "Ultrafast white-light continuum generation and self-focusing in transparent condensed media," J. Opt. Soc. Am. B **16**, 637–650 (1999).

[195] M. Sheik-Bahae, D. C. Hutchings, D. J. Hagan, and E. W. Van Stryland, "Dispersion of Bound Electronic Nonlinear Refraction in Solids," IEEE J. Quantum Electron. **27**, 1296–1309 (1991).

[196] R. DeSalvo, A. A. Said, D. J. Hagan, E. W. Van Stryland, and M. Sheik-Bahae, "Infrared to ultraviolet measurements of two-photon absorption and n2 in wide bandgap solids," IEEE J. Quantum Electron. **32**, 1324–1333 (1996).

[197] A. G. Selivanov, I. A. Denisov, N. V. Kuleshov, and K. V. Yumashev, "Nonlinear refractive properties of Yb^{3+}-doped $KY(WO_4)_2$ and YVO_4 laser crystals," Appl. Phys. B Lasers Opt. **83**, 61–65 (2006).

[198] M. Bradler, P. Baum, and E. Riedle, "Femtosecond continuum generation in bulk laser host materials with sub-μJ pump pulses," Appl. Phys. B Lasers Opt. **97**, 561–574 (2009).

[199] I. V. Mochalov, "Laser and nonlinear properties of the potassium gadolinium tungstate laser crystal $KGd(WO_4)_2$:Nd^{3+}-(KGW:Nd)," Opt. Eng. **36**, 1660–1669 (1997).

[200] J. A. Piper and H. M. Pask, "Crystalline Raman lasers," IEEE J. Sel. Top. Quantum Electron. **13**, 692–704 (2007).

[201] M. Bass, E. W. Van Stryland, D. R. Williams, and W. L. Wolfe, *Handbook of Optics Volume II Devices, Measurements, and Properties 2nd Edition* (McGraw-Hill, 1995).

[202] W. L. Bond, "Measurement of the refractive indices of several crystals," J. Appl. Phys. **36**, 1674–1677 (1965).

[203] B. Wang, H. Jiang, X. Jia, Q. Zhang, D. Sun, and S. Yin, "Thermal conductivity of doped YAG and GGG laser crystal," Front. Optoelectron. China **1**, 138–141 (2008).

[204] P. H. Klein and W. J. Croft, "Thermal Conductivity, Diffusivity, and Expansion of Y_2O_3, $Y_3Al_5O_{12}$, and LaF_3 in the Range 77°–300°K," J. Appl. Phys. **38**, 1603–1607 (1967).

[205] J. F. Bisson, Y. Feng, A. Shirakawa, H. Yoneda, J. Lu, H. Yagi, T. Yanagitani, and K. I. Ueda, "Laser Damage Threshold of Ceramic YAG," Japanese J. Appl. Physics, Part 2 Lett. **42**, 1025–1027 (2003).

[206] S. Xu, J. Qiu, T. Jia, C. Li, H. Sun, and Z. Xu, "Femtosecond laser ablation of crystals SiO_2 and YAG," Opt. Commun. **274**, 163–166 (2007).

[207] G. Turri, S. Webster, Y. Chen, B. Wickham, A. Bennett, and M. Bass, "Index of refraction from the near-ultraviolet to the near-infrared from a single crystal microwave-assisted CVD diamond," Opt. Mater. Express **7**, 855–859 (2017).

[208] C. Kittel, *Introduction to Solid State Physics* (Wiley, 1966).
[209] D. J. Twitchen, C. S. J. Pickles, S. E. Coe, R. S. Sussmann, and C. E. Hall, "Thermal conductivity measurements on CVD diamond," Diam. Relat. Mater. **10**, 731–735 (2001).
[210] S. E. Coe and R. S. Sussmann, "Optical, thermal and mechanical properties of CVD diamond," Diam. Relat. Mater. **9**, 1726–1729 (2000).
[211] J. Achard, F. Silva, A. Tallaire, X. Bonnin, G. Lombardi, K. Hassouni, and A. Gicquel, "High quality MPACVD diamond single crystal growth: High microwave power density regime," J. Phys. D. Appl. Phys. **40**, 6175–6188 (2007).
[212] A. A. Kaminskii, V. G. Ralchenko, and V. I. Konov, "CVD-diamond - A novel χ(3)-nonlinear active crystalline material for SRS generation in very wide spectral range," Laser Phys. Lett. **3**, 171–177 (2006).
[213] E. Anoikin, A. Muhr, A. Bennett, D. Twitchen, and H. de Wit, "Diamond optical components for high-power and high-energy laser applications," Components Packag. Laser Syst. **9346**, 93460T (2015).
[214] Y. Liu, F. Zhang, Z. Wang, F. Yu, L. Wei, X. Xu, and X. Zhao, "$Ca_3(BO_3)_2$, a first wide waveband borate Raman laser crystal with strong Raman effects and outstanding anti-optical damage ability," J. Mater. Chem. C **3**, 10687–10694 (2015).
[215] A. Joshi, N. D. Haynes, D. E. Zelmon, O. Stafsudd, and R. Shori, "Impurity concentration and temperature dependence of the refractive indices of Er^{3+} doped ceramic Y_2O_3," Opt. Express **20**, 4428–4435 (2012).
[216] S. Kumar, H. Tripathi, J. Sharma, and U. Batra, "Structural, morphological, and opto-electrical properties of $Y_{2-x}Yb_xO_3$ nanoparticles synthesized using co-precipitation method," Int. J. Appl. Ceram. Technol. **18**, 12–23 (2021).
[217] K. Shibata, H. Nakamura, and A. Fujii, "Nondoped Y_2O_3 for 3-5μm IR transmission," in *Window and Dome Technologies and Materials II* **1326**, 48, (SPIE, 1990).
[218] Y. Zhao, D. Tang, D. Shen, J. Wang, W. Yao, Z. Shao, C. Shen, D. Yin, Y. Wang, P. Liu, and W. Zhou, "High-Power Ho-Doped Sesquioxide Ceramic Laser In-Band Pumped by a Tm-Doped All-Fiber MOPA," IEEE Photonics J. **10**, 1502107 (2018).
[219] D. E. Zelmon, J. M. Northridge, N. D. Haynes, D. Perlov, and K. Petermann, "Temperature-dependent Sellmeier equations for rare-earth sesquioxides," Appl. Opt. **52**, 3824–3828 (2013).
[220] Y. N. Xu, Z. quan Gu, and W. Ching, "Electronic, structural, and optical properties of crystalline yttria," Phys. Rev. B - Condens. Matter Mater. Phys. **56**, 14993–15000 (1997).
[221] S. V. Ordin and A. I. Shelykh, "Optical and dielectric characteristics of the rare-earth metal oxide Lu_2O_3," Semiconductors **44**, 558–563 (2010).
[222] C. McMillen, D. Thompson, T. Tritt, and J. Kolis, "Hydrothermal Single-Crystal Growth of Lu_2O_3 and Lanthanide-Doped Lu_2O_3," Cryst. Growth Des. **11**, 4386–4391 (2011).
[223] T. W. Houston, L. F. Johnson, P. Kisliuk, and D. J. Walsh, "Temperature Dependence of the Refractive Index of Optical Maser Crystals," J. Opt. Soc. Am. **53**, 1286–1291 (1963).
[224] V. N. Kolobanov, I. A. Kamenskikh, V. V. Mikhailin, I. N. Shpinkov, D. A. Spassky, B. I. Zadneprovsky, L. I. Potkin, and G. Zimmerer, "Optical and

luminescent properties of anisotropic tungstate crystals," Nucl. Instruments Methods Phys. Res. Sect. A Accel. Spectrometers, Detect. Assoc. Equip. **486**, 496–503 (2002).

[225] P. A. Popov, S. A. Skrobov, E. V. Zharikov, D. A. Lis, K. A. Subbotin, L. I. Ivleva, V. N. Shlegel', M. B. Kosmyna, and A. N. Shekhovtsov, "Investigation of the Thermal Conductivity of Tungstate Crystals," Crystallogr. Reports **63**, 111–116 (2018).

[226] M. Bass, C. DeCusatis, J. Enoch, V. Lakshminarayanan, G. Li, C. MacDonald, V. Mahajan, and E. Van Stryland, *Handbook of Optics, Third Edition Volume IV: Optical Properties of Materials, Nonlinear Optics, Quantum Optics* (McGraw-Hill Education, 2009).

[227] W. Ryba-Romanowski, "YVO_4 crystals - Puzzles and challenges," Cryst. Res. Technol. **38**, 225–236 (2003).

[228] N. R. Belashenkov, S. A. Kozlov, V. V. Nazarov, V. Y. Khramov, A. V. Mikhailov, and I. V. Mochalov, "The influence of single and two-photon resonances on the nonlinear refractive index of polyfunctional laser crystals," in *Ultrafast Phenomena in Spectroscopy: Proceedings of the V International Symposium* 202–206, (World Scientific, 1988).

[229] A. L. Gaeta, "Catastrophic collapse of ultrashort pulses," Phys. Rev. Lett. **84**, 3582–3585 (2000).

[230] V. Jukna, J. Galinis, G. Tamosauskas, D. Majus, and A. Dubietis, "Infrared extension of femtosecond supercontinuum generated by filamentation in solid-state media," Appl. Phys. B Lasers Opt. **116**, 477–483 (2014).

[231] M. S. Liu, L. A. Bursill, S. Prawer, and R. Beserman, "Temperature dependence of the first-order Raman phonon line of diamond," Phys. Rev. B - Condens. Matter Mater. Phys. **61**, 3391–3395 (2000).

[232] O. Lux, V. G. Ralchenko, A. P. Bolshakov, V. I. Konov, G. V. Sharonov, A. Shirakawa, H. Yoneda, H. Rhee, H. J. Eichler, R. P. Mildren, and A. A. Kaminskii, "Multi-octave frequency comb generation by χ (3) -nonlinear optical processes in CVD diamond at low temperatures," Laser Phys. Lett. **11**, 086101 (2014).

[233] X. Q. Gao, M. L. Long, and C. Meng, "Compact $KGd(WO_4)_2$ picosecond pulse-train synchronously pumped broadband Raman laser," Appl. Opt. **55**, 6554–6558 (2016).

NOTES

NOTES

Vilniaus universiteto leidykla
Saulėtekio al. 9, III rūmai, LT-10222 Vilnius
El. p. info@leidykla.vu.lt, www.leidykla.vu.lt
Tiražas 20 egz.